The Role of Inosine in Adipose Tissue Metabolism

Dissertation

zur

Erlangung des Doktorgrades (Dr. rer. nat.)

der

Mathematisch-Naturwissenschaftlichen Fakultät

der

Rheinischen Friedrich-Wilhelms-Universität Bonn

vorgelegt von

Birte Niemann

aus Höxter, Deutschland

Bonn 2021

Angefertigt mit Genehmigung der Mathematisch-Naturwissenschaftlichen

Fakultät der Rheinischen Friedrich-Wilhelms-Universität Bonn

1. Gutachter: Prof. Dr. Alexander Pfeifer

2. Gutachter: Prof. Dr. Günther Weindl

Tag der Promotion: 01. April 2022

Erscheinungsjahr: 2022

Acknowledgements

First of all, I would like to thank Prof. Dr. Alexander Pfeifer for this great opportunity and the constant support and supervision during my doctoral studies. I appreciate everything you did for me. Moreover, I would like to thank my second supervisor Prof. Dr. Ulrich Jaehde and my second reviewer Prof. Dr. Günther Weindl for their advice and help. I would also like to thank Dr. Saskia Haufs-Brusberg for the supervision and mentoring during the first years. Thanks to Dr. Laia Reverte-Salisa and Dr. Staffan Hildebrand for the support and the nice scientific and non-scientific discussions.

Furthermore, I would like to thank Jelena Zurkovic, Juhee Yang, Neda Mohammadi and Karsten Motzler, my office mates and dear friends, thank you for the constant support and friendship during good and bad times, without you the last years would not have been the same. Thanks to Dr. Elisabeth Mies-Klomfass, Pia and Nico for proof-reading this thesis.

A big thanks to my partner Nico for encouragement and believing in me as well as for the immense patience and continuous support. Thank you for all the sacrifices you have made, without you I would not have made it here. Moreover, I am very grateful to my family, my parents and my sisters Pia and Ines, thank you for all your help and always being there.

List of abbreviations

A2A	Adenosine A2a receptor (AdoRA2A)
A2B	Adenosine A2b receptor (AdoRA2B)
ABP	L-Ascorbate, d-Biotin, Panthothenate
AC	Adenylate cyclase
ADA	Adenosine deaminase
Adipoq	Adiponectin gene (*Mus musculus*)
ADK	Adenosine kinase
AdoR	Adenosine receptor
AdoRA1	Adenosine A1 receptor
AdoRA2A	Adenosine A2a receptor
AdoRA2B	Adenosine A2b receptor
AdoRA3	Adenosine A3 receptor
ADP	Adenosine 5′-diphosphate
ADSS	Adenylosuccinate synthase
AK	Adenylate kinase
ALP	Alkaline phosphatase
AMP	Adenosine 5′-monosphate
aP2	Adipocyte protein 2 (FABP4)
APS	Ammoniumperoxodisulphate
ASL	Adenylosuccinate lyase
AT	Adipose tissue
ATP	Adenosine 5′-triphosphate
AUC	Area under the curve
BA	Brown adipocytes
BAT	Brown adipose tissue
BMI	Body mass index
bp	Base pair(s)
BSA	Bovine serum albumin
°C	Degrees Celsius
CaCl$_2$	Calcium chloride
cAMP	Cyclic 3',5'- adenosine monophosphate
CD	Control diet
CD39	Cluster of differentiation 39/Ectonucleoside triphosphate diphosphohydrolase 1 (ENTPD1)
CD73	Cluster of differentiation 73/Ecto-5'-nucleotidase (NT5E)
cDNA	Complementary DNA
C/EBP	CCAAT/enhancer-binding protein
cGMP	Cyclic 3'-5' guanosine monophosphate
CNT	Concentrative nucleoside transporter
CO$_2$	Carbon dioxide
Conc.	Concentration
Cox8b	Cytochrome C oxidase subunit 8B gene (*Mus musculus*)
CREB	cAMP responsive element-binding protein
DAB	3-3' diaminobenzidine
DAG	Diacylglycerol
dH$_2$O	Deionized water
DIO	Diet-induced obesity
DMEM	Dulbecco's Modified Eagle Medium
DMSO	Dimethyl sulfoxide
DNA	Deoxyribonucleic acid
EC$_{50}$	Half maximal effective concentration
EDTA	Ethylene diamine tetraacetic acid
EE	Energy expenditure
EGTA	Ethylene glycol-bis (β-aminoethyl ether) - N, N, N', N'-tetraacetic acid

ELISA	Enzyme-linked immunosorbent assay
ENT	Equilibrative nucleoside transporter
ENT1-A-KO	Adipocyte specific equilibrative nucleoside transporter 1 (ENT1) knock out (ENT1$^{fl/fl}$ ApnCre+)
ENT1fl-ApnCre	Equilibrative nucleoside transporter 1 (ENT1)-floxed Adiponectin-Cre
ENTPD1	Ectonucleoside triphosphate diphosphohydrolase 1/Cluster of differentiation 39 (CD39)
EPAC	Exchange protein activated by cAMP
ERK	Extracellular signal-regulated kinase
ETC	Electron transport chain
EtOH	Ethanol
Fabp4	Fatty acid binding protein 4 gene (*Mus musculus*)
FABP4	Fatty acid binding protein 4 (aP2)
FBS	Foetal bovine serum
FCCP	Carbonyl cyanide p-trifluoro-methoxyphenyl hydrazine
FFA	Free fatty acids
gDNA	Genomic DNA
GDP	Guanosine-5′-diphosphate
GEF	Guanine nucleotide exchange factor
GMP	Guanosine monophosphate
GPCR	G protein coupled receptor
GRK	G protein coupled receptor kinase
GTP	Guanosine-5′-triphosphate
GTT	Glucose tolerance test
h	hour(s)
hBA	Human brown adipocytes
HBSS	Hanks' balanced salt solution
HCl	Hydrochloric acid
H&E	Hematoxylin & Eosin staining
HFD	High fat diet
HGPRT	Hypoxanthine-guanine phosphoribosyl transferase
H$_2$O	Water
H$_2$O$_2$	Hydrogen peroxide
Hprt	Hypoxanthine guanine phosphoribosyl transferase gene (*Mus musculus*)
HPRT	Hypoxanthine-guanine phosphoribosyl transferase
HRP	Horseradish peroxidase
HSL	Hormone sensitive lipase
IBMX	3-isobutyl-1-methylxanthine
IMP	Inosine 5′-monophosphate
i.p.	*intraperitoneal*
IP$_3$	Inositol trisphosphate
KCl	Potassium chloride
KD	Knock down
KH$_2$PO$_4$	Potassium dihydrogen phosphate
KO	Knock out
KOH	Potassium hydroxide
M/mM/µM	molar/millimolar/micromolar
mA	milliampere
MAPK	Mitogen-activated protein kinase
mg/µg	milligram/microgram
MgCl$_2$	Magnesium chloride
min	Minute(s)
ml/µl	milliliter/microliter
µm	micrometer
mRNA	Messenger ribonucleic acid

List of abbreviations

NaCl	Sodium chloride
NaF	Sodium fluoride
Na$_2$HPO$_4$	Disodium hydrogen phosphate
NaN$_3$	Sodium azide
Na$_3$VO$_4$	Sodium orthovanadate
NBMPR	Nitrobenzyl mercaptopurine riboside/S-(4-Nitrobenzyl)-6-thioinosin
Nd5	NADH:ubiquinone oxidoreductase core subunit 5 gene (*Mus musculus*)
Ndufa1	NADH:ubiquinone oxidoreductase subunit A1 gene (*Mus musculus*)
NE	Norepinephrine
ng	nanogram
NGS	Normal goat serum
nm	nanometer
nM	nanomolar
NMR	Nuclear magnetic resonance
NST	Non-shivering thermogenesis
NT5E	Ecto-5'-nucleotidase/Cluster of differentiation 73 (CD73)
O$_2$	Oxygen
OCR	Oxygen consumption rate
p38	p38 mitogen-activated protein kinase
PBS	Phosphate buffered saline
PCR	Polymerase chain reaction
PDE5	Phosphodiesterase 5
PET-CT	Positron emission tomography–computed tomography
PFA	Paraformaldehyde
PGK	Phosphoglycerate kinase
PIP$_2$	Phosphatidylinositol 4,5-bisphosphate
PKA	Protein kinase A
PKC	Protein kinase C
PLC	Phospholipase C
pmol	picomole(s)
PNP	Purine-nucleoside phosphorylase
pp	percentage point(s)
Pparg	Peroxisome proliferator activated receptor gamma gene (*Mus musculus*)
PPARγ	Peroxisome proliferator activated receptor gamma
Ppargc1a	Peroxisome proliferator activated receptor gamma (PPARγ) cofactor 1 alpha gene (*Mus musculus*)
PPARGC1α	Peroxisome proliferator activated receptor gamma (PPARγ) cofactor 1 alpha
Prdm16	PR domain containing 16 gene (*Mus musculus*)
PRDM16	PR domain containing 16
P/S	Penicillin/Streptomycin
qRT-PCR	Quantitative real-time polymerase chain reaction
RhoGEF	Guanine nucleotide exchange factor for Rho/Rac/Cdc42-like GTPases
RhoA	Ras homology gene family, member A
ROCKs	Ras homology gene family, member A (RhoA) associated protein kinases
rpm	Rotations per minute
RT	Room temperature
s	Second(s)
SAT	Subcutaneous (white) adipose tissue
SDS	Sodium dodecyl sulphate
SDS-PAGE	Sodium dodecyl sulphate polyacrylamide gel electrophoresis
SEM	Standard error of the mean
SLC	Solute carrier

Slc29a1	Solute carrier family 29 (nucleoside transporters), member 1 gene (*Mus musculus*)
Slc29a2	Solute carrier family 29 (nucleoside transporters), member 2 gene (*Mus musculus*)
SV40	Simian virus 40
SVF	Stromal vascular fraction
T3	Triiodothyronine
TBS-T	Tween 20 (0.1%) solution in Tris buffered saline
TEMED	N, N, N', N'-Tetramethyl ethylene diamine
TUV	Tunable UV/Vis-detector
Ucp1	Uncoupling protein 1 gene (*Mus musculus*)
UCP1	Uncoupling protein 1
UPLC	Ultra Performance Liquid Chromatography
VAT	Visceral (white) adipose tissue
V(O$_2$)	Volume of oxygen consumed
WA	White adipocytes
WAT	White adipose tissue
WATg	Gonadal white adipose tissue
WATi	Inguinal white adipose tissue
WHO	World Health Organization
WT	Wild type
XO	Xanthine oxidase

Table of contents

1. Introduction

1.1. Obesity

Obesity was formally recognized as a global epidemic by the World Health Organization (WHO) in 1997 (World Health Organization, 2000), and recent findings on the prevalence of overweight and obesity are still alarming: In 2016, 1.9 billion adults and 340 minors were overweight, while more than 650 million of the adults were obese (World Health Organization, 2018). In comparison to 1975, the number of obese adults has almost tripled (World Health Organization, 2018). Obesity negatively affects individuals' health and, given its high prevalence, also poses a serious challenge for public healthcare systems (Organisation for Economic Co-operation and Development, 2019).

Overweight and obesity develop due to a chronic positive energy imbalance, when calorie intake exceeds energy expenditure (EE), resulting in an abnormal and unhealthy accumulation of body fat. Causes for this imbalance are increased sedentary lifestyles, overeating of energy-dense food and low physical activity in present-day societies (Blüher, 2019) as well as certain genetic, psychological and (patho)physiological factors (Sharma and Padwal, 2010).

The Body Mass Index (BMI) is commonly used to classify overweight and obesity. It is defined as the body mass (in kg) divided by the square of body height in meters. For adults, the WHO defines overweight as a BMI greater than or equal to 25 kg/m^2 and obesity as a BMI greater than or equal to 30 kg/m^2 (Table 1).

Table 1 BMI categories

Category	BMI [kg/m^2]
Underweight	<18.5
Normal weight	18.5-24.99
Overweight	≥25-29.99
Moderately obese	≥30-34.99
Severely obese	≥35

Source: (World Health Organization, 2021)

Besides BMI, further evaluation of the fat distribution, for instance by measuring the waist-to-hip ratio, can also serve as an indicator of the individual risk for obesity-related metabolic dysfunction and comorbidities (Manolopoulos et al., 2010).

There are several risk factors and comorbidities associated with a raised BMI including diabetes mellitus type 2, fatty liver disease, hypertension, myocardial infarction, stroke, dementia, osteoarthritis, obstructive sleep apnoea, psychological stress and several types of cancer (Blüher, 2019). A constellation of interconnected comorbidities and metabolic disorders including dyslipidemia, hypertension, glucose intolerance, proinflammatory state, and a prothrombotic state is called 'metabolic syndrome' (Kaur, 2014).

The currently approved medications for weight loss therapies in obesity, such as orlistat, liraglutide, naltrexone/bupropion and phentermine primarily decrease food intake or absorption in the intestines (Williams et al., 2020). Most of these drugs have an efficacy of 3–7% (estimated net weight loss) (Srivastava and Apovian, 2018). For obese individuals, bariatric surgery can be a necessary intervention to aim remission of the metabolic syndrome (Leblanc et al., 2011). This is due to the patients oftentimes being incapable of physical activity, while other non-surgical therapies such as dietary regimen or pharmacological approaches are less effective (Leblanc et al., 2011; Gloy et al., 2013).

With regard to the described steadily progressing epidemic scenario, development of novel therapeutic tools targeting metabolic regulatory pathways, to prevent obesity and to mitigate its negative effects, is of high relevance.

1.2. Adipose Tissues

Two different types of adipose tissue (AT) can been observed in mammals: white adipose tissue (WAT) and brown adipose tissue (BAT). WAT, which is present in higher quantities, serves as energy storage, while BAT combusts energy producing heat (Hoffmann et al., 2015; Cohen and Spiegelman, 2016).

1.2.1. Anatomy and physiology of white adipose tissue

WAT is specialized to store energy in form of triglycerides during nutrient abundance. Under nutrient deficit conditions, these caloric reservoirs are enzymatically hydrolysed and free fatty acids (FFAs) as well as glycerol are provided as energetic fuel for other organs (Cohen and Spiegelman, 2016). This process is called lipolysis and tightly controlled by insulin and catecholamines, the 'key hormones of the fed and fasted states' (Cohen and Spiegelman, 2016). Moreover, WAT plays an important role in regulation of systemic metabolism by secreting adipokines, such as adiponectin and leptin, as a response to changes in systemic energy balance (Rosen and Spiegelman, 2014). As an endocrine organ, WAT influences appetite, satiety, insulin-sensitivity and -secretion (Zhang et al., 1994; Choe et al., 2016).

In humans WAT is anatomically distinguished in two major depots: subcutaneous WAT (SAT) and visceral WAT (VAT). VAT is located in the abdominal cavity surrounding and protecting the internal organs and is further subdivided into mesenteric, omental, perirenal, and retroperitoneal depots (Scheme 1A). Increased VAT mass in obese humans (known as 'central obesity') is closely linked to metaflammation and metabolic complications, such as type 2 diabetes (Després, 2006). Adult mice have gonadal adipose tissue (WATg), which is considered as VAT in mouse models (Scheme 1B). In contrast, there is a lack of gonadal adipose tissue in humans. Most of the human VAT is contained in the omentum. This anatomical difference has to be considered, when extrapolating findings from rodents/mice to humans.
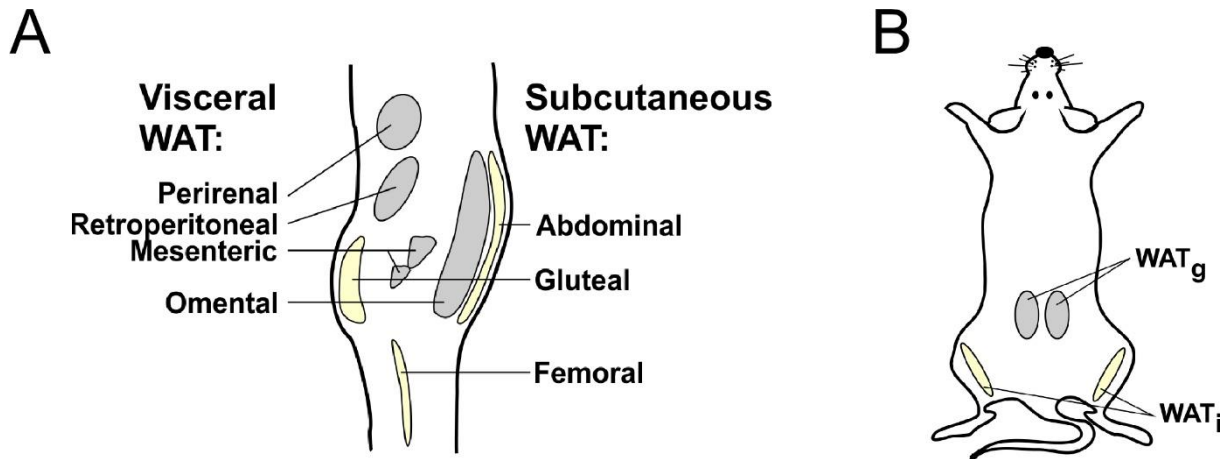
Scheme 1 Location of WAT in humans and mice

(A) Human white adipose tissue depots. (B) Murine white adipose tissue depots. Subcutaneous WAT is shown in yellow and visceral WAT in grey. Author's adaptation from (Choe et al., 2016). Adipose Tissue Remodeling: Its Role in Energy Metabolism and Metabolic Disorders. Front. Endocrinol. 7:30. doi: 10.3389/fendo.2016.00030

Human SAT is subdivided into abdominal, gluteal and femoral depots (Scheme 1A). Increased SAT mass in obese subjects, also known as 'peripheral obesity', is correlated with lower incidence of metabolic disorders compared to obesity derived increased VAT mass (Després et al., 1989; Pouliot et al., 1992; Stolic et al., 2002) and less prone to metaflammation (Sanyal et al., 2017). Moreover, subcutaneous fat shows a higher thermogenic capacity and potential for browning compared to VAT (Collins et al., 1997; Guerra et al., 1998; Barbatelli et al., 2010; Seale et al., 2011). Using animal models murine inguinal WAT (WATi) is often compared to subcutaneous human WAT (Scheme 1).

Recently, it has been shown that defects in murine adipose tissue differentiation caused severe symptoms of lipodystrophy, including metabolic inflexibility and development of type 2 diabetes (Gilardi et al., 2019). Generalized lipodystrophy in humans has been found to be associated with insulin resistance and secondary diseases, such as diabetes mellitus, hypertriglyceridemia, hepatic steatosis, polycystic ovaries, acute pancreatitis and blindness due to diabetic retinopathy (Garg, 2011). Consequently, a healthy development of adipose tissue is required for functioning metabolic control.

1.2.2. Development of white adipose tissue

In mice, expression of adipocyte-specific genes in the subcutaneous region can be observed from embryonic day 16.5-17.5 onwards (Birsoy et al., 2011). In addition, inguinal white adipocytes containing lipid components can be detected on postnatal day 1, but mature adipocytes and WATi pads appear later after birth (Han et al., 2011). Moreover, murine visceral fat develops later, no precursor cells are observed until postnatal day 4, a cell cluster starts to appear on postnatal day 7 and mature epididymal adipocytes can be found from postnatal day 14 onwards (Han et al., 2011).

In contrast, human WAT starts to appear and develop in the 14-24th week of gestation (Poissonnet et al., 1984). From late gestation until approximately the age of ten, adipocytes are filled with lipids with no changes in cell numbers (in non-obese children), followed by a proliferation phase of adipocytes until the age of 18, resulting in leveled off adult cell numbers (Knittle et al., 1979). During adulthood the number of adipocytes remains constant (in lean and obese individuals) and a certain turnover of adipocytes of approximately 10% per year is observed (Spalding et al., 2008). If body fat mass is increased or decreased during adulthood, only the adipocytes size or volume changes (Spalding et al., 2008).

1.2.3. Anatomy and physiology of brown adipose tissue

The other important adipose tissue is BAT (brown adipose tissue). The main function of BAT is thermoregulation by performing non-shivering thermogenesis (NST) under the control of norepinephrine (NE), which is released from sympathetic nerves (Cannon and Nedergaard, 2004). The special brown color of this organ is given by the iron content of the high number of mitochondria. In addition, the uniquely high expression of uncoupling protein 1 (UCP1, thermogenin) of BAT is most important for the process of NST. The UCP1 protein is located in the inner mitochondrial membrane and uncouples ATP production from the respiratory chain by translocating protons from the mitochondrial intermembrane space to the mitochondrial matrix. This process enables fast substrate oxidation of FFAs. The resulting energy is dissipated as heat, thereby body temperature is maintained without muscular contribution (Cannon and Nedergaard, 2004).

Human newborns have interscapular BAT depots (Scheme 2A), which regresses with age switching to a white appearance (Symonds, 2013). While some human adults have supraclavicular BAT and BAT depots in the neck region, smaller BAT depots can also be found along the aorta, vertebrae and kidneys (Nedergaard et al., 2007) (Scheme 2B). In adult mice the major BAT depot is located in the interscapular area (Scheme 2C).
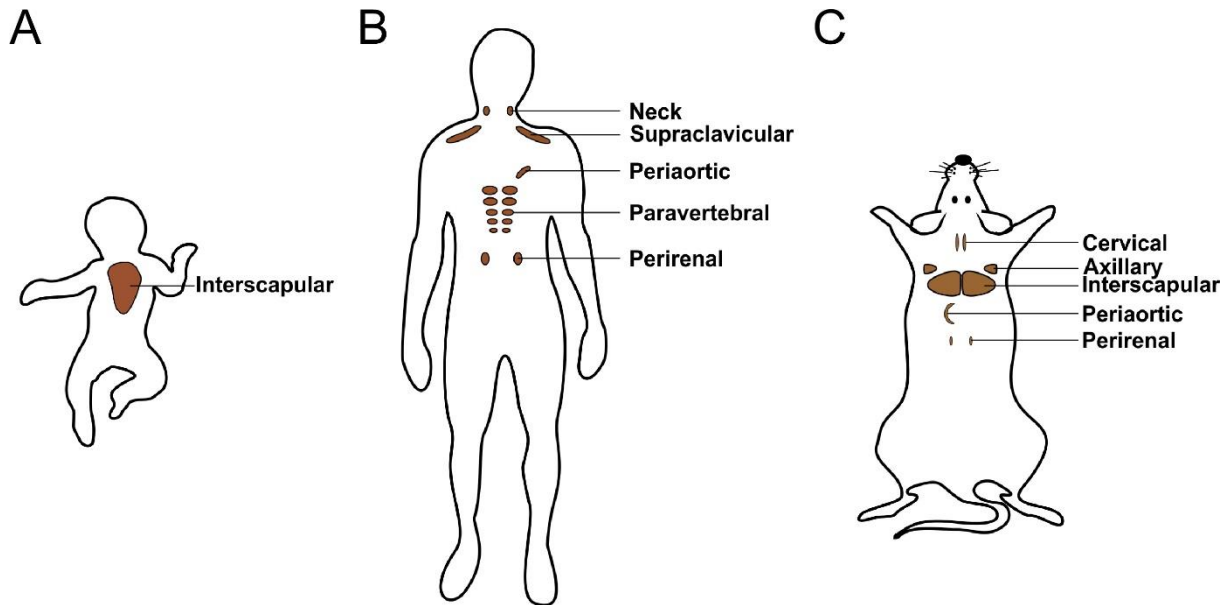
Scheme 2 Location of BAT in humans and mice
(A) Brown adipose tissue of human newborns. (B) Brown adipose tissues of adult humans. (C) Brown adipose tissues of adult mice. Author's adaptation from (van den Berg, Susan M et al., 2017). Immune Modulation of Brown(ing) Adipose Tissue in Obesity. Endocrine Reviews, 38, 46–68.

For many years, it has been proposed that BAT only exist in infants and rodents to protect against hypothermia. However, using [18]F- fluorodeoxyglucose (^{18}F-FDG) positron-emission tomographic computer tomography (PET-CT) imaging, viable and functional BAT was also detected in human adults (Nedergaard et al., 2007; Virtanen et al., 2009). Independent studies revealed that the amount and the activity of BAT negatively correlates with BMI, while resting metabolic rate showed a significant positive correlation with BAT activity (Cypess et al., 2009; van Marken Lichtenbelt et al., 2009). Although BAT is comparatively small in size (2-4% of birth weight) (Symonds, 2013) compared to other organs, Bartelt et al. (2011) observed, that the total contribution of activated BAT to FFA uptake was even higher than for muscles. These findings demonstrate the high importance of BAT in whole body metabolism and EE. Therefore, BAT is considered as a promising target for future obesity therapies, increasing BAT activity could be a therapeutic option to treat or prevent obesity and associated diseases, especially for patients, who are incapable of physical activity (Cypess and Kahn, 2010).

1.2.4. Development of brown adipose tissue

BAT has a different developmental pattern than WAT. Murine BAT becomes visible on day 15.5 of embryonic development (E15.5) and expands rapidly until birth (Schulz and Tseng, 2013). Mice are so called 'altricial' mammals, they have a comparably short gestation period, causing their offspring to be born with an immature hypothalamic-pituitary adrenal axis (Symonds, 2013). Accordingly, newborn mice are mainly warmed by their mother in the nest and not by performing non-shivering thermogenesis. UCP1 expression of interscapular murine BAT is detectable after 18 days of gestation and gradually increases until birth (Xue et al.,

2007). The peak value for *Ucp1* mRNA expression is reached on postnatal day 1 whereas maximal protein levels occur ~10 days after birth (Xue et al., 2007).

In contrast, precocial mammals, such as humans, have a longer gestation period enabling maturation of the hypothalamic-pituitary adrenal axis prior to birth (Symonds, 2013). Thus, from the day of birth on infants are able to perform non-shivering thermogenesis to be protected against hypothermia. The quantity and UCP1 expression of human BAT peak at birth and decrease with age, due to brown adipocytes being replaced by white fat cells (Symonds, 2013). However, some of these adipocytes still have the potential to be reactivated (Symonds, 2013).

1.2.5. Types of adipocytes

Adipose tissues contain several interacting cell types, including fat cells, immune cells, endothelium, fibroblasts, neurons, and stem cells. Adipocytes constitute for approximately 90% of the adipose tissue volume, while it has been shown that other cells types predominate in cell-number (Rosen and Spiegelman, 2014).

Three different types of adipocytes are found in mammals: brown (BA), white (WA) and beige/brite adipocytes.

WA' morphology is characterized by a large monolocular lipid droplet, which constitutes for most of the intracellular space, and a low density of mitochondria (Scheme 3C). BA, on the other hand, have a high amount of mitochondria and contain smaller, multilocular lipid droplets (Cinti, 2002) (Scheme 3A). Moreover, BA are characterized by their uniquely high expression of UCP1. So-called 'beige' or 'brite' adipocytes can be described as an intermediate of BA and WA with morphologically characteristic higher numbers of mitochondria and more and smaller lipid droplets in comparison to WA (Wu et al., 2012)(Scheme 3B).
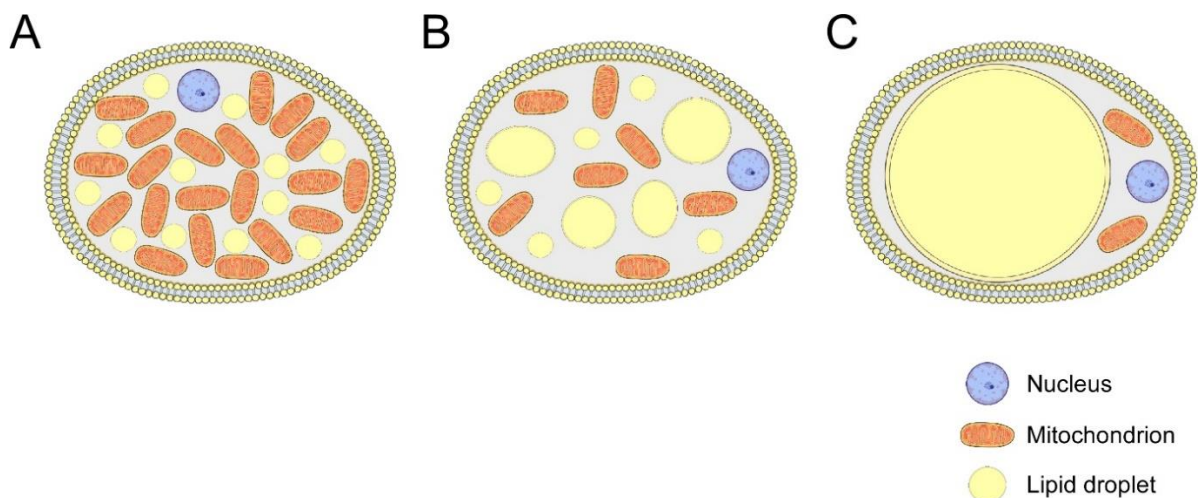
Scheme 3 Adipocytes morphology
(A) BA are characterized by a high density of mitochondria and small lipid droplets. (B) Beige adipocytes contain less mitochondria and bigger lipid droplets in comparison to BA. (C) WA have an unilocular lipid droplet and a few mitochondria. Adapted from (Perdikari et al., 2018)

Introduction

Both, BA and WA, derive from mesenchymal stem cells, but they have different precursor cells: It has been shown that paired-box protein 7 and myogenic factor 5 positive precursor cells give rise to BA, while WA progenitors are negative for both markers (Seale et al., 2008; Rosen and Spiegelman, 2014).

Beige adipocytes, have a BA-like appearance and express UCP1, although they derive from white precursor cells *via de novo* differentiation or by transdifferentiation from mature WA (Seale et al., 2008; Cinti, 2009; Wang and Seale, 2016). The development of beige adipocytes in WAT is dramatically enhanced by cold exposure, β3-selective adrenergic agonists treatment or treatment with thiazolidinedione drugs (Himms-Hagen et al., 2000; Wilson-Fritch et al., 2004; Barbatelli et al., 2010). This process, called 'beiging' or 'browning' of WAT, is most prominent in the inguinal subcutaneous fat depot, while the perigonadal adipocytes are less prone to undergo browning (Barbatelli et al., 2010). Beiging/browning of WAT might be a promising approach for obesity therapy, because the beige adipocytes perform NST and thereby increase whole body EE. However, induction of beiging/browning by cold exposure or β3-selective adrenergic agonists is often not feasible due to cardiac side effects (Nitti et al., 2013; Cypess et al., 2015) or poor bioavailability (Weyer et al., 1998). In particular, cold exposure leads to increased cardiac output (Hanna et al., 1975) and mirabegron (the only clinically approved β3-adrenoceptor agonist), which is used to treat the overactive bladder syndrome, can also cause hypertensive events (Nitti et al., 2013; Cypess et al., 2015). This might be a problem or risk, especially for obese and hypertensive patients, since cardiovascular complications often occur as comorbidities of obesity. Moreover, the β3-adrenoceptor agonist CL-316243, which is frequently used in rodent models, has an unsatisfactory oral bioavailability of ~10% (Weyer et al., 1998). Consequently, there is still a high interest in development of novel compounds to induce browning/beiging of WAT.

Despite their differences of origin, BA and WA share the main transcription factors of adipogenesis, such as peroxisome proliferator-activated receptor gamma (PPARγ) and CCAAT/enhancer-binding proteins (C/EBPs) (Rosen and MacDougald, 2006). Adipogenic induction initiates expression of the early adipogenic transcription factors C/EBPβ and C/EBPδ, which promote adipogenesis by induction of C/EBPα and PPARγ expression (Rosen and MacDougald, 2006). C/EBPα and PPARγ act as late adipogenenic modulators and induce the expression of several downstream targets including fatty acid binding protein 4 (FABP4/aP2), which are required for adipogenic function, such as lipolysis and insulin signaling (Hotamisligil and Bernlohr, 2015). Moreover, PPARγ is not only crucial for adipocyte differentiation, but also important to maintain the differentiated state mature adipocyte functions (Rosen and MacDougald, 2006), such as systemic insulin sensitization (Sugii et al., 2009).

Thermogenic function is limited to the UCP1-expressing brown and beige adipocytes. Most of this specialized function is controlled by transcriptional cofactors: prominent examples are the peroxisome proliferator-activated receptor gamma coactivator 1 alpha (PPARGC1α), PR domain containing 16 (PRDM16) and C/EBPβ (Puigserver and Spiegelman, 2003; Seale et al., 2007; Kajimura et al., 2009). Brown and beige adipocytes are activated by cold exposure, when the sympathetic nervous system (SNS) initiates the release of norepinephrine (NE). In turn, NE activates adrenergic beta-3 receptors, which are G protein-coupled receptors (GPCRs) with stimulatory G protein α-subunits (G_s). Thereby, adipocytes adenylate cyclase (AC) is activated and cAMP accumulates intracellularly. Next, raised cAMP levels activate the enzyme protein kinase A (PKA) (Cannon and Nedergaard, 2004), leading to phosphorylation of multiple targets including hormone sensitive lipase (HSL) and perilipin. Phosphorylation of these proteins directly initiates lipolysis/hydrolysis of triglycerides into glycerol and FFAs (Braun et al., 2018). The released FFAs serve as fuel for NST of brown and beige adipocytes. Additionally, it has been shown, that FFAs can directly activate UCP1 (Cannon and Nedergaard, 2004). Moreover, cAMP-mediated activation of PKA can also lead to phosphorylation of transcription factors, such as cAMP responsive element-binding protein (CREB), which directly enhances expression levels of UCP1 (Cannon and Nedergaard, 2004). Besides PKA signaling, the exchange protein activated by cAMP (EPAC) is another receptor for cAMP. It has previously been shown that EPAC regulates mitogen-activated protein kinase (MAPK) pathways, such as extracellular signal-regulated kinases (ERKs) and p38 mitogen-activated protein kinases (p38s) (Monaghan et al., 2008). p38 MAPK has been identified to promote thermogenesis by inducing expression of UCP1 and PPARGC1α, indicating that this pathway also contributes to the thermogenic potential of brown and beige adipocytes (Cao et al., 2004).

Different G_s-coupled GPCRs are expressed in thermogenic adipocytes. Activation of these receptors can similarly lead to increased intracellular cAMP concentrations activating the described cAMP-PKA signaling axis. An example, recently described by Gnad et al. (2014), is the adenosine A2A receptor (AdoRA2A) which is highly expressed in murine and human BA. AdoRA2A activation in mice resulted in increased EE, decreased diet-induced weight gain and improved glucose tolerance (Gnad et al., 2014). Those findings reveal that purinergic signaling is a promising target for future obesity therapies.

1.3. Enzymatic metabolism of ATP

Scheme 4 provides an overview about the metabolism of ATP-derived purinergic molecules: Upon SNS activation, adenosine 5′-triphosphate (ATP) is released as a co-transmitter with classical neurotransmitters, such as noradrenaline or acetylcholine (Khakh and Burnstock, 2009). Under physiological conditions, extracellular ATP is rapidly degraded to adenosine by ectonucleotidases and alkaline phosphatase (ALP) (Gordon, 1986). Firstly, ectonucleoside

triphosphate diphosphohydrolase-1 (ENTPD1; also known as CD39) hydrolizes ATP and adenosine 5′-diphosphate (ADP) to adenosine 5′-monophosphate (AMP). Secondly, AMP is converted into extracellular adenosine by the ecto-5'-nucleotidase (NT5E; also known as CD73) and ALP (Pettengill et al., 2013; Da Rocha Lapa et al., 2014).
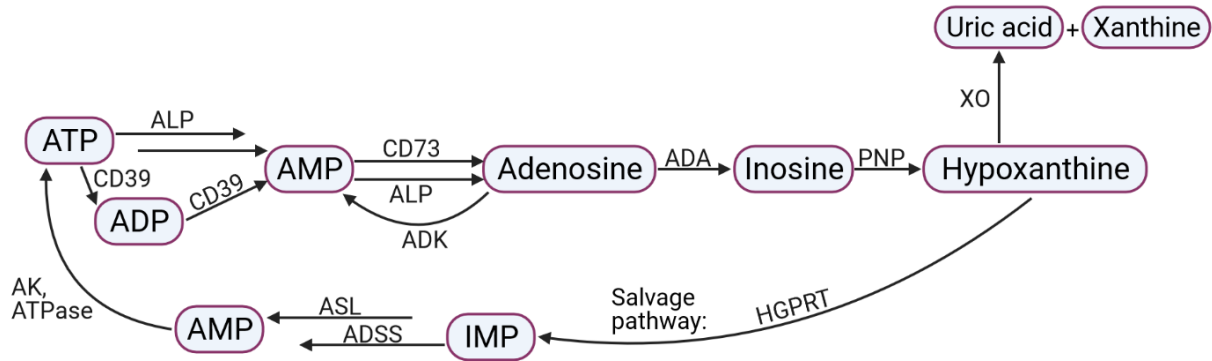
Scheme 4 Enzymatic metabolism of ATP

ATP - Adenosine 5′-triphosphate, ADP - Adenosine 5′-diphosphate, AMP - Adenosine 5′-monophosphate, CD39 - Cluster of differentiation 39 / Ectonucleoside triphosphate diphosphohydrolase-1 (ENTPD1), CD73 - Cluster of differentiation 73 / Ecto-5'-nucleotidase (NT5E), ALP - Alkaline phosphatase, ADK - Adenosine kinase, ADA – Adenosine deaminase, PNP - Purine nucleoside phosphorylase, XO - Xanthine oxidase, HGPRT - Hypoxanthine-guanine phosphoribosyltransferase, IMP - Inosine 5′-monophosphat, ADSS - Adenylosuccinate synthase, ASL - Adenylosuccinate lyase, AK - Adenylate kinase, ATPase - ATP synthase

Additionally, adenosine is released from BA after NE stimulation (Gnad et al., 2014). The phosphotransferase adenosine kinase (ADK) regulates adenosine concentrations by converting the purine ribonucleoside adenosine into AMP (Boison, 2013). Moreover, the deamination of adenosine by adenosine deaminase (ADA) gives rise to inosine within seconds (Da Rocha Lapa et al., 2014). The ADA enzyme is expressed intra- and extracellularly. It forms a complex with two molecules of CD26 on the cell surface (Kameoka et al., 1993). Accordingly, adenosine is characterized by a short half-life of approximately 10 seconds, while its direct metabolite inosine is more stable with a half-life of approximately 15 hours (Welihinda et al., 2016).

Subsequently, purine nucleoside phosphorylase (PNP) converts inosine into hypoxanthine, which can be further degraded to xanthine and uric acid by xanthine oxidase (XO) (Haskó et al., 2004; Giuliani et al., 2017). However, it is more likely that hypoxanthine is 'recycled' *via* the salvage pathway into nucleotides (Zoref-Shani, 1992). In this salvage reaction an activated ribose-5-phosphate is added to the base hypoxanthine by hypoxanthine-guanine phosphoribosyltransferase (HGPRT) resulting in inosine 5′-monophosphate (IMP) (Klepinin et al., 2020). The formed IMP may be converted in two steps into AMP. These reactions are mediated by the enzymes adenylosuccinate synthase (ADSS) and adenylosuccinate lyase (ASL) (Hatch, 1966). In a next step, AMP is converted by adenylate kinase (AK) and ATP synthase (ATPase) into ATP (Panayiotou et al., 2014).

1.4. Transporters of the purinergic system

1.4.1. Pannexins and connexins

Most of the ATP is stored intracellularly, it is released into the extracellular space under specific conditions, such as necrosis, apoptosis, hypoxia and inflammation (Dosch et al., 2018). Moreover, ATP is released as a co-transmitter from sympathetic nerves (Burnstock and Gentile, 2018).

In addition to cell damage and vesicular exocytosis, many cell types release ATP in an autocrine manner *via* connexin hemichannels or pannexin channels (Eltzschig et al., 2006; Poon et al., 2014). The subtypes connexin 43 and pannexin 1 are the most widely expressed and there exists plenty of empirical evidence on these channels (Dosch et al., 2018). Pannexins and connexins are hexameric membrane channels, while only connexins form gap-junctions (Penuela et al., 2013). ATP has been found to be released by adipocytes during physiological activation (Gnad et al., 2014; Adamson et al., 2015; Tozzi et al., 2020). Adamson et al. (2015) showed that inhibition of pannexin 1 channels diminished insulin-stimulated glucose uptake of adipocytes.

1.4.2. Concentrative and equilibrative nucleoside transporters

Nucleosides can access the intracellular space *via* nucleoside transporters. There are two different solute carrier (SLC) gene families encoding these plasma membrane transporters: SLC28 and SLC29 (Guallar et al., 2007). The SLC28 family encodes concentrative nucleoside transporter (CNT) proteins, while the SLC29 genes encode equilibrative nucleoside transporter (ENT) proteins (Baldwin et al., 2004).

CNTs are unidirectional inward transporters; they transport nucleosides against their concentration gradient into the cell. This process is driven by sodium (and proton) electrochemical gradients (Pastor-Anglada and Pérez-Torras, 2018). There are three subtypes of CNTs: CNT1, CNT2, and CNT3. They differ in their substrate specificities: CNT1 is mostly pyrimidine-nucleoside selective, CNT2 is purine-nucleoside preferring, while CNT3 transports both (Gray et al., 2004). Thus, CNT2 plays a role in clearance of extracellular adenosine and its metabolites (Aymerich et al., 2006). In addition, it has been suggested that CNT3 might also contribute to adenosine reuptake (Guallar et al., 2007).

ENTs are ubiquitously found in most cell types, they mediate bidirectional transport of nucleosides down their concentration gradients (Baldwin et al., 2004). Together with CNTs, by mediating nucleoside and nucleobase uptake, the ENTs play a key role in the salvage pathways of nucleotide synthesis (Baldwin et al., 2004). Moreover, these transporters influence the extracellular concentrations of adenosine and its metabolites available to cell surface receptors. Thereby, they are involved in many physiological processes, such as cardiovascular

function and neurotransmission (Baldwin et al., 2004; Löffler et al., 2007). It has been reported that adipocytes can also secrete inosine and hypoxanthine besides adenosine (Kather, 1988). In addition, ENTs are responsible for the intracellular uptake of cytotoxic nucleoside analogs, which are used for cancer and viral infections therapy (Zhang et al., 2007). There are four subtypes of ENTs: ENT1-4. ENT1 and ENT2 are predominantly located in plasma membranes, while ENT3 is located intracellularly in lysosomal membranes (Baldwin et al., 2005). ENT4 is also located in plasma membranes, it has a low affinity for adenosine at physiological pH (Baldwin et al., 2004), but has been shown to be a cardiac adenosine transporter at acidic pH during ischemia (Barnes et al., 2006). Taken together, under regular physiological conditions ENT1 and ENT2 subtypes are assumed to be the main regulators of adenosine-, inosine- and hypoxanthine-release into the extracellular space.

While ENT1 and ENT2 show similar selectivities for natural nucleosides, they have different sensitivities for inhibition by S-(4-Nitrobenzyl)-6-thioinosin (nitrobenzyl mercaptopurine riboside; NBMPR) and coronary vasodilators, such as dipyridamole (Baldwin et al., 2005). Baldwin et al. (2005) showed that human ENT1 is 100-1000-fold more sensitive than ENT2 to the aforementioned inhibitors. Deletion of ENT1 in mice led to significantly increased extracellular adenosine concentrations of cardiomyocytes, which has been shown to be cardioprotective (Rose et al., 2011). Further studies described a neuroprotective effect of adenosine, especially during increased extracellular adenosine concentrations due to inhibition or deletion of ENT (Kao et al., 2017). Moreover, it has been shown that inhibition of ENT1 by dipyridamole affects extracellular purine concentrations of adipocytes (Kather, 1988; Scheibler, 2017).

1.5. G-Protein coupled receptors

G-protein-coupled receptors (GPCRs) are seven-transmembrane-domain proteins, which regulate a broad range of intracellular signaling cascades (Hilger et al., 2018). GPCRs are involved in numerous human diseases, such as immune and central nervous system disorders as well as Alzheimer's disease, obesity and diabetes (Hauser et al., 2017). Consequently, they are in the focus of drug discovery, while already one third of the FDA approved drugs acts on GPCR targets (Hauser et al., 2017).

G-proteins are membrane-associated and carry an endogenous GTPase activity (Rosenbaum et al., 2009). They are heterotrimeric proteins composed of three subunits: alpha, beta and gamma (Scheme 5).
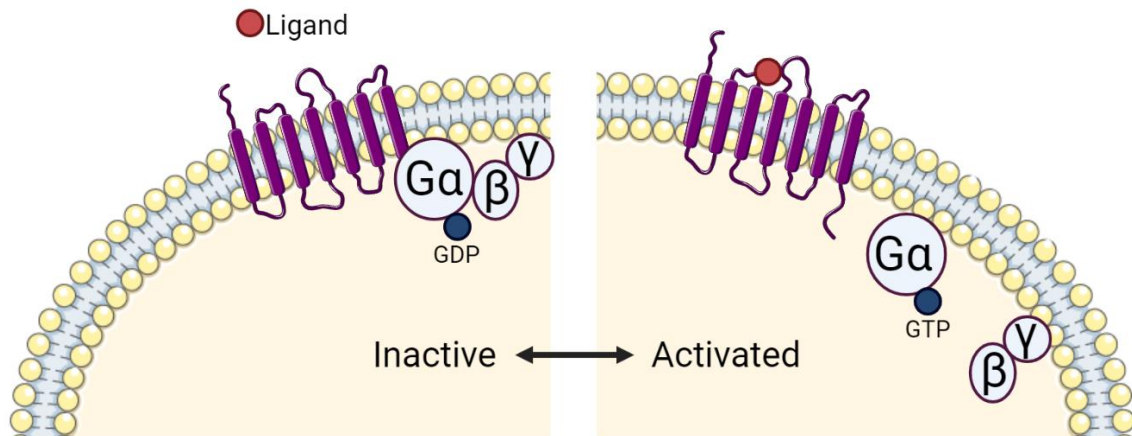
Scheme 5 Composition and activation of GPCRs

GDP – Guanosine-5′-diphosphate, GTP – Guanosine-5′-triphosphate. Author's adaptation from (Jo and Jung, 2016).

Upon binding of a ligand to a GPCR, the conformation of the seven-transmembrane helical bundle, which is allosterically coupled to the guanine nucleotide binding pocket of the Gα subunit, changes (Hanlon and Andrew, 2015). Thereby, G-protein signaling is initiated: The GDP at the α subunit is replaced by GTP transferring the inactive Gα subunit into an activated state by conformational change (Hanlon and Andrew, 2015). This process promotes dissociation of the G-protein from the GPCR. Next, the G-protein further dissociates into Gα and βγ subcomplex, which both interact with effectors activating downstream signaling as a physiological response to the ligand dependent stimulation of the GPCR (Rosenbaum et al., 2009). When the intrinsic GTPase activity of the Gα subunit hydrolyses the bound GTP into GDP, Gα becomes inactivated allowing reassociation with Gβγ (Hanlon and Andrew, 2015). This process ends the GPCR G-protein activation cycle (Scheme 5).

The heterotrimeric G-proteins are classified by their G alpha subunit. These Gα-proteins are divided in four subfamilies: $Gα_s$, $Gα_{i/o}$, $Gα_{q/11}$ and $Gα_{12/13}$ (Hilger et al., 2018). Moreover, each subclass targets a specific signaling cascade (Wettschureck and Offermanns, 2005) (Scheme 6).
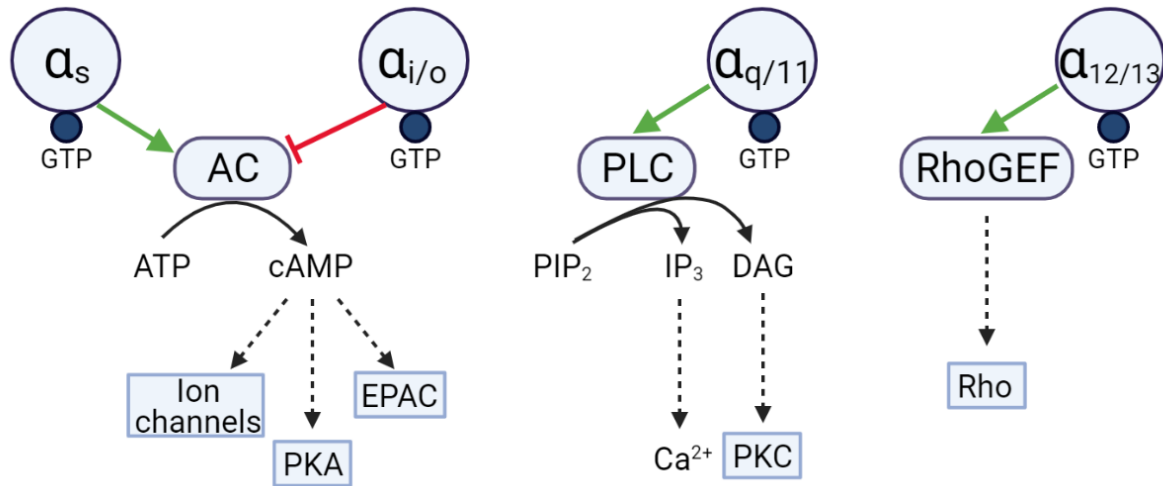
Scheme 6 Classification of G alpha subunits

GTP – Guanosine-5′-triphosphate, AC - Adenylate cyclase, ATP – Adenosine-5′-triphosphate, cAMP - Cyclic 3′,5′-adenosine monophosphate, PKA – Protein kinase A, EPAC - exchange factor directly activated by cAMP, PLC - Phospholipase C, PIP$_2$ - Phosphatidylinositol 4,5-bisphosphate, IP$_3$ – Inositol trisphosphate, DAG – Diacylglycerol, PKC - Protein kinase C, RhoGEF - Guanine nucleotide exchange factor for Rho/Rac/Cdc42-like GTPases

Gα_s, Gα_i and Gα_o modulate adenylate cyclases (Hanlon and Andrew, 2015). Activated Gα_s stimulates AC activity leading to increased extracellular cAMP levels (Wettschureck and Offermanns, 2005). Subsequently, cAMP regulates ion channels or signaling cascades of PKA and EPAC (Syrovatkina et al., 2016). In contrast, Gα_i and Gα_o inhibit AC activity causing opposite effects of Gα_s (Wettschureck and Offermanns, 2005). The third subfamily G$\alpha_{q/11}$ activates the β-isoforms of phospholipase C (PLC β1-4), this enzyme hydrolyses phosphatidylinositol 4,5-bisphosphate (PIP$_2$) into inositol trisphosphate (IP$_3$) and diacylglycerol (DAG) (Rhee and Bae, 1997; Syrovatkina et al., 2016). DAG activates protein kinase C (PKC) as a downstream effector protein, while binding of IP$_3$ to its receptor, which acts as a calcium channel, leads to calcium release of intracellular stores from the endoplasmic reticulum (Rhee and Bae, 1997). Lastly, the G$\alpha_{12/13}$ subclass activates the guanine nucleotide exchange factors for Rho/Rac/Cdc42-like GTPases (RhoGEFs), which in turn activate Rho (Hanlon and Andrew, 2015).

1.6. Purinergic signaling

Burnstock (1978) classified the purinergic receptors in two major groups: P1 receptors, which are activated by adenosine, and P2 receptors, which are activated by ATP and ADP, but not by AMP and adenosine.

The P2 receptor family, which serves as a target for ATP and other nucleotides, is further grouped into two classes: P2Y receptors, which are GPCRs, and P2X receptors, which act as ligand-gated, non-selective cation channels (Dubyak, 1991; Abbracchio and Burnstock, 1994) (Scheme 7).

P1 purinergic receptors are GPCRs activated by adenosine (Fredholm et al., 2011). There are four adenosine receptors (AdoRs): AdoRA1, AdoRA2A, AdoRA2B and AdoRA3. Activation of adenosine receptor subtypes A1 and A3 leads to decreased intracellular cAMP levels, because they are coupled to $G_{i/o}$ protein α-subunits inhibiting AC activity (Burnstock, 2007) (Scheme 7). In contrast, activation of the G_s-coupled GPCRs AdoRA2A and AdoRA2B leads to increased AC activity resulting in elevated intracellular cAMP concentrations (Burnstock, 2007) (Scheme 7). In addition, the human AdoRA2B was observed to regulate phospholipase C activity by $G_{q/11}$ coupling (Burnstock, 2007).
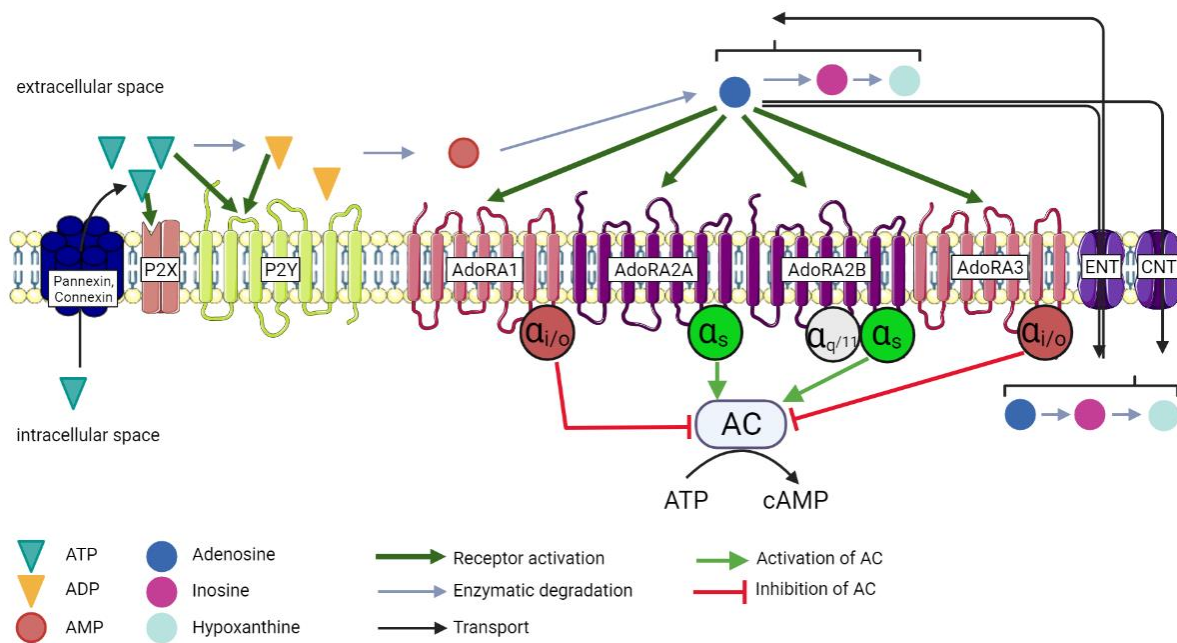
Scheme 7 Purinergic signaling
AdoRA – Adenosine receptor A, AC - Adenylate cyclase, ADP – Adenosine-5′-diphosphate, ATP – Adenosine-5′-triphosphate, AMP – Adenosine-5′-monophosphate, cAMP - Cyclic 3′,5′- adenosine monophosphate, CNT – Concentrative nucleoside transporter, ENT – Equilibrative nucleoside transporter. Author's adaptation from (Ledderose et al., 2016).

It has been shown that adenosine acts as an endogenous agonist at all four human adenosine receptors (Fredholm et al., 2001). Moreover, similar potencies of adenosine were observed at A1, A2A and A3 adenosine receptors (to modulate cAMP concentrations in cells with comparable receptor densities), while adenosine was found to act approximately 50 times less potent at A2B receptors (Fredholm et al., 2001). The authors concluded that physiological adenosine levels cannot activate AdoRA2B.

Because of divergent expression patterns of the four adenosine receptors, effects of adenosine stimulation can differ between species: For instance, isoproterenol-stimulated lipolysis of hamster BA is decreased by adenosine treatment, while murine and human BA react with increased lipolysis to adenosine stimulation (Schimmel and McCarthy, 1984; Gnad et al., 2014). A possible explanation for this opposite effect is the different expression pattern of AdoRs in the BAT of these species: the inhibitory AdoRA1 and the stimulatory AdoRA2A have

similar expression levels in hamster BA, while in human and murine BA the AdoRA2A subtype predominates AdoRA1 density (Gnad et al., 2014). Gnad et al. (2020) recently showed, that AdoRA2A-AdoRA2B-interaction is required for adenosine-mediated effects in BAT. Particularly, deletion of AdoRA2B fully abolished the stimulatory effect of a selective AdoRA2A agonist, while AdoRA2B-mediated lipolysis was not changed in A2A-deficient BA and BAT compared to wild type (WT) controls (Gnad et al., 2020). These findings indicate that AdoRA2B can regulate BAT metabolism independently of AdoRA2A. In contrast, interaction with AdoRA2B seems to be crucial for AdoRA2A-mediated adenosine signaling (Gnad et al., 2020).

For a long time, inosine was considered as an inactive metabolite of adenosine (Mabley et al., 2003). However, there is growing evidence that inosine can act anti-inflammatory, immunomodulatory, neuroprotective and antidepressant (Gomez and Sitkovsky, 2003; Haskó et al., 2004; Kaster et al., 2013; Welihinda et al., 2016). Many of these protective effects are associated with AdoRs activation (especially A1, A2A and A3) by inosine (Gomez and Sitkovsky, 2003; Haskó et al., 2004; Kaster et al., 2013; Welihinda et al., 2016). Moreover, protective effects of inosine against development of type 1 diabetes have been found in murine models (Mabley et al., 2003). In line with these findings that inosine can act on P1 receptors, effects of inosine on AT metabolism should be investigated.

2. Contribution, aim and research questions

This thesis adds to a growing body of literature on novel approaches to stimulate thermogenic adipose tissue. Activation of thermogenic brown and beige AT has been widely recognized as a potential target to improve metabolic activity and energy expenditure alleviating obesity. However, most of the currently known mechanisms stimulating thermogenic AT, such as β3-adrenergic activation, are not therapeutically feasible, primarily due to systemic (cardiac) side effects or suboptimal oral bioavailability. Consequently, novel molecular activators, which increase thermogenesis of brown and beige AT, need to be identified.

Previous research showed that purinergic signaling might serve as a pharmaceutical approach to increase AT energy expenditure and combat obesity. Moreover, recent findings revealed that inosine can activate adenosine receptors. Accordingly, inosine could be a promising candidate to target the purinergic signaling cascade in AT. A preliminary experiment of our working-group focusing on ATP-derived nucleotides and nucleosides showed increased extracellular inosine levels as a response to stimulation of BA with norepinephrine indicating a potential physiological role of inosine in BAT. The functional effects of inosine on thermogenic AT have not been extensively investigated yet, especially the *in vivo* effects on AT and whole body metabolism remain unclear. Therefore, the aim of this thesis is to investigate the effects of inosine on AT metabolism.

In order to elucidate the role of inosine in adipose tissue metabolism, the following research questions were addressed:

- ➢ What is the role of extracellular inosine in thermogenic adipose tissue?
- ➢ To what extent does inosine administration influence whole body energy expenditure, BAT function and browning of WAT?
- ➢ To what extent does global deletion of ENT1 affect extracellular inosine levels, whole body energy expenditure and adipose tissue metabolism?
- ➢ To what extent does adipocyte-specific deletion of ENT1 affect whole body energy expenditure and adipose tissue metabolism?
- ➢ What are relevant signaling pathways of inosine in adipose tissue?

In order to address these questions, a series of *in vitro* and *in vivo* experiments was performed. Initially, microdialysis, a method to measure dialysates in intact organs *ex vivo*, was developed. Subsequently, analysis of purines was carried out using an UPLC-TUV system. Furthermore, various methods of molecular biology, such as mRNA and protein analysis, ELISAs, functional biochemical assays and histological analysis, were applied to investigate the effects of inosine on AT metabolism. Several mouse models were used to study the effects of inosine *in vivo*. Continuous administration of inosine to (wild type) mice was studied *in vivo* using micro-

osmotic pumps. As a genetic approach, global ENT1-KO mice were investigated to study the influence of increased endogenous extracellular inosine levels *in vivo*. In order to assess the contribution of ENT1-deletion in adipocytes to whole body metabolism, an adipocyte-specific ENT1-A-KO mouse model (ENT1floxed-AdiponectinCre) was generated and studied. With the intention to investigate AdoRA2B as a potential target of inosine in AT, effects in AdoRA2B-KO mice and adipocytes were tested. Moreover, pharmacological approaches were used to modulate the identified pathways and to influence extracellular inosine levels.

3. Materials and methods

This chapter introduces the materials and methods used to answer the research questions formulated in the previous section. Each section lists the materials and equipment used, before the applied methods are presented. Unless explicitly mentioned, all chemicals used were purchased from Calbiochem (Darmstadt), Carl Roth GmbH (Karlsruhe), Merck (Darmstadt), Sigma-Aldrich (München) and VWR (Darmstadt). Milli-Q Water Purification System (Merck EMD Millipore) was used to purify water.

3.1. Animals

All animal experiments have been approved by LANUV (Landesamt für Natur, Umwelt und Verbraucherschutz), NRW, Germany. Mice were housed and bred at the animal facility 'Haus für Experimentelle Therapie', University of Bonn. Animals had access to a standard rodent diet (Ssniff® R/M-H) and water *ad libitum*.

C57Bl/6J mice were ordered from Charles River. ENT1-KO and ENT1-floxed mice were kindly provided by Prof. Eltzschig, School of Medicine, Department of Aenestesiology, University of Colorado Denver, USA. Generation of ENT1-KO mice has been described by Choi et al. (2004). Heterozygous breeding-pairs enabled comparison of global ENT1-KO and WT littermates. For the adipocyte-specific ENT1-A-KO mouse model (ENT1fl-ApnCre) deletion of ENT1 in adipocytes was achieved by crossing ENT1-floxed mice with Adiponectin-Cre mice (B6;FVB-Tg(Adipoq-cre)1Evdr/J, Jackson Laboratory, Stock No: 010803) to obtain animals with homozygous loxP-flanked ENT1-alleles without Cre or hemizygous for Cre. AdoRA2B-KO (A2B-KO) mice were kindly provided by Prof. Idzko, Department of Pulmonology, University of Vienna, Austria. Generation of A2B-KO mice has been described by Csóka et al. (2007). Heterozygous breeding-pairs enabled comparison of A2B-KO and WT littermates.

3.1.1. Genotyping

The following list provides an overview of the materials and equipment used for genotyping:

- Acetic acid (Roth, Cat.No. 3738.4)
- Centrifuge (Eppendorf, Cat. No. 5415R)
- EDTA (Roth, Cat.No. 8043.2)
- Electrophoresis chamber, RunOne™ Electrophoresis System (Embi Tec)
- Ethanol (EtOH) (Roth, Cat.No. 9065.4)
- Ethidiumbromide solution 10mg/ml (Roth, Cat. No. 2218.1)
- Gel casting chambers, RunOne™ Agarose Gel Casting Systeme (Embi Tec)
- Microwave (Severin)
- OneTaq® Quick Load® 2x MM w/Std Buffer (New England BioLabs, Cat. No. M0486S)
- Phire Tissue Direct PCR Master Mix (ThermoFisher Scientific, Cat. No. F170L)
- 2-Propanol (Roth, Cat. No. 6752.4)

- Proteinase K (Roche, Cat. No. 03115828001)
- QuantityOne® Software (BioRad)
- Reaction tube 1.5 mL (Sarstedt, Cat. No. 72706)
- Roti®- Phenol/chloroform/isoamylalcohol (Roth, Cat. No. A156.2)
- Sodium dodecyl sulphate (SDS) (Roth, Cat. No. 2326.2)
- Sodiumchloride (NaCl) (Roth, Cat. No. 3957.1)
- Thermocycler Biometra (Analytik Jena)
- Thermomixer (Eppendorf)
- Tris (Roth, Cat. No. AE15.3)
- Tris HCl (Roth, Cat. No. 9090.3)
- UV light transilluminator, GelDoc®XR (BioRad)

3.1.1.1. Isolation and amplification of genomic DNA (gDNA) from ENT1-WT/-KO and ENT1fl-ApnCre biopsies

In order to genotype ENT1-WT/-KO and ENT1fl-ApnCre mice, biopsies of earlobe or tail were taken. Digestion and DNA-extraction were performed using Phire™ Tissue Direct PCR Master Mix and following manufacturer's instructions. Afterwards, DNA was amplified by Polymerase Chain Reaction (PCR). The following primers, mixtures and PCR program were used for DNA-amplification (Tables 2-8):

Table 2 Primers used for ENT1-WT/-KO genotyping

Name	Primer sequence (5'→3')
ENT1_ComF	CCCCCTGAACCTTCTAGGAC
ENT1_WTR	CCAGGCGGTTTGTGAAATAC
ENT1_KOR	GACAGCTCAGAACCACCTGG

Table 3 Mixture for ENT1-WT/-KO genotyping PCR

Substance	Volume [µl]
gDNA	1
2x Phire tissue direct PCR master mix	10
Primer ENT1_ComF (10pmol/µl)	1
Primer ENT1_WTR (10pmol/µl)	1
Primer ENT1_KOR (10pmol/µl)	1
H_2O	6

Table 4 Primers used for ENT1-floxed (ENT1fl) genotyping

Name	Primer sequence (5'→3')
ENT1fl_floxF	AGGTGGAGATGGATGCTCTG
ENT1fl_ComR	CCCAGGAAGCTTTAACCTGA

Table 5 Mixture for ENT1-floxed (ENT1fl) genotyping PCR

Substance	Volume [µl]
gDNA	1
2x Phire tissue direct PCR master mix	10
Primer ENT1fl_floxF (10pmol/µl)	1
Primer ENT1fl_ComR (10pmol/µl)	1
H_2O	7

Table 6 Primers used for Adiponectin Cre (ApnCre) genotyping

Name	Primer sequence (5'→3')
ApnCre_15381	ACGGACAGAAGCATTTTCCA
ApnCre_18564	CGATGTGCCATGTGAGTCTG
ApnCre_7338	CTAGGCCACAGAATTGAAAGATCT
ApnCre_7339	GTAGGTGGAAATTCTAGCATCATCC

Table 7 Mixture for Adiponectin Cre (ApnCre) genotyping PCR

Substance	Volume [µl]
gDNA	1
2x Phire tissue direct PCR master mix	10
ApnCre_15381 (10pmol/µl)	1.875
ApnCre_18564 (10pmol/µl)	1.875
ApnCre_7338 (10pmol/µl)	1.875
ApnCre_7339 (10pmol/µl)	1.875
H_2O	2.4

Table 8 PCR program used for genotyping of ENT1-WT/-KO and ENT1fl-ApnCre mice

Step	Time [s]	Temperature [°C]	
Initial denaturation	300	98	
Denaturation	5	98	
Annealing	5	55	
Extension	30	72	x30 cycles
	60	72	
Pause	∞	4	

3.1.1.2. Isolation and amplification of genomic DNA (gDNA) from A2B-WT/-KO biopsies

To genotype A2B-WT/-KO mice, biopsies of earlobe or tail were taken and put in an Eppendorf tube. 500µl of proteinase K buffer (Table 9) were added and samples were placed in a thermomixer, under constant shaking (550rpm) at 55°C, for digestion overnight.

Table 9 Proteinase K buffer

Substance	Quantity
EDTA	5mM
NaCl	200mM
Proteinase K	0.1 mg/ml
SDS	0.2%
Tris HCl pH 7.6	100 mM

Substances were dissolved in H_2O.

The next day, 500µl Roti®-phenol/chloroform/isoamylalcohol was added, samples were shaken vigorously for 15 seconds and incubated at room temperature (RT) for 5 minutes, in order to extract gDNA. Subsequently, tubes were centrifuged for 15 minutes at 16°C and 13000rpm, before the obtained upper phase was transferred to a new reaction tube. To precipitate gDNA, 800µl of isopropanol were added followed by a centrifugation step for 10 minutes at 13000rpm. Afterwards, the pellet was washed with 1ml 70% EtOH and pelleted by centrifugation for 5 minutes at 13000rpm. Finally, the DNA-pellet was dried and resolved in 30µl H_2O. DNA was amplified using an OneTaq® kit. The following primers, mixture and PCR program were used for DNA-amplification (Tables 10-12):

Table 10 Primers used for A2B-WT/-KO genotyping

Name	Primer sequence (5'→3')
A2B_1	GTACGTGGCGCTGGAGCTGGTTATC
A2B_2	GCTCTGTGTGAGCACCAGCACGAAG
A2B_Neo	GGGTGGGATTAGATAAATGCCTGCTCT

Table 11 Mixture for A2B-WT/-KO genotyping PCR

Substance	Volume [µl]
gDNA	1
Master Mix OneTaq®	12.5
Primer A2B_1 (10pmol/µl)	0.5
Primer A2B_2 (10pmol/µl)	0.5
Primer A2B_Neo (10pmol/µl)	0.5
H_2O	10

Table 12 PCR program used for genotyping of A2B mice

Step	Time [s]	Temperature [°C]	
Initial denaturation	30	94	
Denaturation	15	94	
Annealing	30	58	
Extension	45	68	x32 cycles
	300	68	
Pause	∞	4	

3.1.1.3. Agarose gel electrophoresis

To separate and visualize PCR products, agarose gel electrophoresis was performed. Agarose was solved in 1x TAE buffer (Table 13) and heated in a microwave to obtain a 2% agarose solution. Subsequently, ethidium bromide (800 ng/ml) was added and the gels were solidified in casting chambers at RT.

Table 13 TAE buffer 50x

Substance	Quantity
Tris	2M
Acetic acid	5.71%
Na_2-EDTA	50mM

Substances were dissolved in H_2O and stored at RT.

Afterwards, samples were loaded in agarose gels, which were placed into an electrophoresis chamber containing 1 x TAE buffer. To separate different PCR products, gel electrophoresis was performed at 100V and RT. Finally, DNA bands were visualized using an UV light transilluminator (GelDoc®XR, BioRad) in combination with QuantityOne® software(BioRad). Based on PCR product sizes genotypes were identified (Table 14).

Table 14 Product sizes of genotyping PCRs

Name	Genotype	Product size [bp]
ENT1 (global)	WT	467
	KO	700
ENT1 floxed	WT	145
	floxed	214
ApnCre	WT	324
	Cre positive	200
A2B (global)	WT	247
	KO	417

3.1.2. Diet-induced obesity

To investigate diet-induced obesity (DIO) effects in mice, animals were fed a high fat diet (HFD) (Ssniff®, D12492), meaning that 60% of the calories were derived from fat. The control group received a control diet (CD) (10% kJ fat, Ssniff®, D12450B). 6-week-old mice were fed with the respective diet for 12 weeks, while the bodyweight was monitored weekly.

HFD/CD experiments were performed with global ENT1-WT/-KO and ENT1fl-ApnCre mice. HFD and respective *in vivo* experiments of three ENT1-WT and three -KO mice were done by Dr. Saskia Haufs-Brusberg. All other HFD- and CD-experiments were performed by myself.

3.1.3. Implantation of micro-osmotic pumps

Micro-osmotic pumps (alzet®, model 1004, Cat. No. 0009922) were implanted subcutaneously into 8-week-old, male C57Bl6/J mice, under anesthesia (3.5% isoflurane), following manufacturer's instructions. Subsequently, inosine (0.11µl/h of 3.4mM solution; 2.4µg/day) or vehicle (NaCl 0.9%) was permanently released for 28 days. During this period, mice were fed either a CD or a HFD and the bodyweight was monitored. Indirect calorimetry measurements were performed from day 22 until day 27. After 28 days, the mice were sacrificed and the organs were isolated for analysis.

Two cohorts, with five mice per group each, were operated and studied. Surgeries, monitoring of bodyweight and organ isolation of the first cohort was done by Dr. Saskia Haufs-Brusberg. All experiments of the second cohort, including additional indirect calorimetry measurements, as well as data and organ analysis of both cohorts, were performed by myself.

3.1.4. Glucose tolerance tests

After 11 weeks of HFD or CD (17-week-old mice), glucose tolerance tests (GTTs) were performed. Initially, mice were fasted for 5 hours. Subsequently, to measure basal glucose levels of mice, the tail vein was punctured, and the glucose concentration of the obtained blood drop was measured using a glucose meter (Accu-Check; Roche) and dipsticks (Roche). Afterwards, eight µl/g bodyweight glucose solution (0.25g/ml) were injected intraperitoneally (*i.p.*). Glucose levels of blood withdrawn from the tail vein were determined 15, 30, 60, 90, and 120 minutes *post* injection.

3.1.5. NMR measurements

Body composition was determined using a benchtop NMR device (Bruker Minispec) measuring lean-, fat- and water-mass of the mice.

3.1.6. Metabolic cages (TSE system)

For metabolic characterization of mice, oxygen consumption and motility were measured at 23ºC every 2 minutes for 24 hours, with a light and dark cycle of 12 hours each, using a Phenomaster system (TSE). During the measurements mice were single caged with access to

food and water *ad libitum*. Acute cold exposure of mice was performed for 1-2 hours at 4°C, during the light cycle and without access to food and water.

3.1.7. Uptake of radioactive labelled fat and glucose

Metabolic tracer studies in 8-week-old male ENT1-WT and -KO mice were performed by Dr. Heine (Prof. Heeren´s working group, Department of Biochemistry and Molecular Cell Biology, University Medical Center Hamburg-Eppendorf, Hamburg, Germany). A lipid emulsion, labelled with ^{14}C-triolein (0.15 MBq/kg) and ^{3}H-DOG (0.72 MBq/kg), was administered to the mice by oral gavage. Mice were sacrificed 2 hours *post* gavage application and organs were dissected and homogenized. Subsequently, radioactivity of respective solubilized organs was measured by liquid scintillation counting.

3.1.8. Bomb calorimetry of feces

The following list provides an overview of the materials and equipment used for bomb calorimetry:

- Parr 6725 Semimicro Calorimeter (Parr, Serial No. 6725-1909-93531)
- CONOXIA® GO2X medical oxygen (Linde, Cat. No.2020175)
- dd-H$_2$0 (Milli-Q Water Purification System)
- Wire Fuse 10cm NI ALLOY (Parr, Item No. 45C10)

A 6725 Semimicro Bomb Calorimeter was used to measure the heat produced by the combustion of murine feces samples. 0.02-0.04g of feces were placed in an Inconel dish of a 1109A Semimicro Oxygen Bomb. Afterwards a 10cm Ni-Cr loop was installed causing the wire to touch the samples. Finally, the bomb was closed, saturated with oxygen and placed into a stainless steel air can containing 400ml of dd-H$_2$0. After preparation of electrical connections for the firing circuit, the samples were burned and the resulting rise in temperature was measured enabling calculation of heat [cal/g]. Thereby the amount of energy derived from food, which was not absorbed and consequently secreted by feces, can be estimated.

3.1.9. Quantification of inosine plasma concentrations

The following list provides an overview of the materials and equipment used to quantify inosine plasma concentrations:

- Enspire® microplate reader (Perkin Elmer, Cat. No. 2300-0000)
- Inosine Assay Kit (Sigma-Aldrich, Cat. No. MAK100)
- 96-well microplates for fluorescence-based assays (Thermo Fisher, Cat. No. M33089)

Inosine plasma concentrations were determined using an Inosine Assay Kit following the manufacturer´s instructions (Sigma-Aldrich). Fluorescence intensity was measured at λ_{ex}535 nm/λ_{em}587 nm using EnSpire™ plate reader.

3.1.10. *Ex vivo* lipolysis of BAT and WAT

The following list provides an overview of the materials and equipment used for *ex vivo* lipolysis assay:

- 96-well plates (Sarstedt, Cat. No. 83.3924)
- BSA (Sigma-Aldrich, Cat. No. A7030)
- DMEM (Gibco, Cat. No. 21063)
- Free glycerol reagent (Sigma-Aldrich, Cat. No. F6428)
- Glycerol standard (Sigma-Aldrich, Cat. No. G7793)
- Incubator, HERAcell® 150 (Heraeus)
- Inosine (Sigma-Aldrich, Cat. No. I4125)
- L-(−)-Norepinephrine (+)-bitartrate salt monohydrate (NE)(Sigma-Aldrich, Cat. No. A9512)
- Reaction tube 1.5 mL (Sarstedt, Cat. No. 72706)
- Enspire® microplate reader (Perkin Elmer, Cat. No. 2300-0000)

Adipose tissue explants were dissected, weighted and placed in ice-cold lipolysis medium (Table 15). Next, the explants were transferred into a new 96-well plate with 100µl of lipolysis medium per well in absence or presence of selected compounds. Afterwards, tissues were incubated for 2h at 37°C and 5% CO_2. Subsequently, 10µl supernatant, 30µl lipolysis medium and 60µl free glycerol reagent were pipetted to a 96-well plate in duplicates. Blank wells consisting of 40µl lipolysis medium and 60µl free glycerol reagent and standard wells (5µl standard reagent and 95µl free glycerol reagent) were also pipetted in duplicates. Afterwards, the plate was incubated for 5 minutes at 37°C. Sample (A_{sample}), blank (A_{blank}) and standard absorption ($A_{standard}$) were measured at λ540nm using EnSpire™ plate reader. Measured absorption at λ600nm was used as a reference wavelength for each sample, respectively.

Glycerol content was calculated by the formula:

$$\text{Glycerol content} = \frac{\left(A_{sample} - A_{blank} \right)}{\left(A_{standard} - A_{blank} \right)} \, x \, Concentration_{standard}$$

Finally, glycerol release was normalized to tissue weights.

Table 15 Lipolysis medium

Substance	Quantity
BSA (fatty acid free)	1g
DMEM	49ml

BSA 2% was solved in DMEM.

3.1.11. Oxygraph measurements

The following list provides an overview of the materials and equipment used for oxygraph measurements:

- Carbonyl cyanide p-trifluoro-methoxyphenyl hydrazine (FCCP) (Tocris, Cat. No. 0453)
- Digitonin (Sigma-Aldrich, Cat. No. D5628-1G)
- D-Sucrose (Roth, Cat. No. 4621.1)
- Ethylene glycol-bis(β-aminoethyl ether)-N,N,N',N'-tetraacetic acid (EGTA) (Sigma-Aldrich, Cat. No. E4378)
- Guanosine5'-diphosphate disodium salt (GDP) (Abcam, Cat. No. ab146529)
- HEPES (Sigma-Aldrich, Cat. No. H7523)
- Inosine (Sigma-Aldrich, Cat. No. I4125)
- Lactobionic acid (Sigma-Aldrich, Cat. No. 153516)
- L-glutamic acid monosodium salt hydrate (Sigma-Aldrich, Cat. No. G1626-100G)
- Magnesium chloride hexahydrate ($MgCl_2 \times 6H_2O$) (Scharlau, Cat. No. MA 0036)
- Malonic acid (Sigma-Aldrich, Cat. No. M1296-100G)
- Octanoyl-DL-Carnitine chloride (Cayman, Cat. No. 15048)
- Oxygraph-2k (Oroboros Instruments)
- Potassium dihydrogen phosphate (KH_2PO_4) (Merck, Cat. No. 104873)
- Potassium hydroxide (KOH) (Sigma-Aldrich, Cat. No. P1767)
- Sodium azide (NaN_3), (Alfa Aesar, Cat. No. L13716)
- Sodium pyruvate (Sigma-Aldrich, Cat. No. P2256-25G)
- Sodium succinate dibasic hexahydrate (Sigma-Aldrich, S2378-100G)
- Taurine (Sigma-Aldrich, Cat. No. T 0625)

Oxygen consumption of tissue sections was measured using Oxygraph 2k® apparatus. Before starting a new measurement, chambers and stoppers were washed three times with 70% ethanol, three times with water and two times with MIR05 buffer (Table 16). Finally, 2ml of MIR05 buffer were added. Subsequently, oxygen sensors were calibrated for 20 minutes until a stable baseline was achieved. Tissue explants were isolated from mice, weighed, and stored in MIR05 buffer on ice. Due to high mitochondrial respiration, 2-3mg of BAT per measurement was sufficient. 10-15mg of the less active WATi pieces were used. For pre-treatment (e.g. with inosine), tissue explants were incubated with the respective compound, dissolved in MIR05 buffer, for 15 minutes at 37ºC.

After incubation, the tissues were transferred to the oxygraph chambers, which were closed with stoppers to remove air bubbles. Measurements were performed during constant stirring. After achieving a stable state of mitochondrial respiration of the tissues, digitonin (25µg/ml) was added as a detergent to permeabilize plasma membranes. Next, octanoylcarnitine (1mM), as a substrate for fatty acid oxidation, and the tricarboxylic acid cycle substrates, pyruvate

(62.5mM), malate (2mM) and glutamate (10mM), were injected to both oxygraph chambers. After reaching a plateau of respiration rate, succinate (10mM), the substrate for Complex II of the respiratory chain reaction, was added, followed by an injection of GDP (2mM) to inhibit the UCP1 mediated proton flux. Next, to max out the mitochondrial respiration rate, the uncoupling reagent carbonyl cyanide p-trifluoro-methoxyphenyl hydrazine (FCCP) (0.5µM) was administered. Subsequently, to determine the non-mitochondrial respiration rate, sodium azide (NaN_3) (50mM) was added, which is an inhibitor of cytochrome C oxidase. Finally, oxygen consumption rates were calculated using DatLab7 software[1] and normalized to tissue weights.

Table 16 Mitochondrial respiration buffer (MIR05)

Substance	Quantity
EGTA	0.90g
$MgCl_2 x 6H_2O$	0.610g
Taurine	2.502g
KH_2PO_4	1.361g
HEPES	4.77g
D-Sucrose	37.65g
Lactobionic acid 0.5M	120ml
BSA	1g

All substances, except of lactobionic acid and BSA, were dissolved in 800ml H_2O. Afterwards, the pH was adjusted to 7.1 with KOH. Subsequently, lactobionic acid and BSA were added and the solution was filled up with H_2O to a final volume of 1l. The buffer was stored at -20ºC.

3.1.12. Microdialysis

The following list provides an overview of the materials and equipment used for microdialysis measurements:

- CONOXIA® GO2X medical oxygen (Linde, Cat. No.2020175)
- L-(−)-Norepinephrine (+)-bitartrate salt monohydrate (NE)(Sigma-Aldrich, Cat. No. A9512)
- Microdialysis probes (CMA 30 Linear MD Probe, Cat. No. 8010460)
- Myograph (Danish Myo Technology A/S, Type: DMT630M, S/N: DMT603-291116-84842)
- Perfusion fluid (M Dialysis AB, Cat. No. P000034)
- Reaction tubes 1.5 mL (Sarstedt, Cat. No. 72706)
- Syringe pump (CMA, Model: CMA 402, Cat. No. CMA8003110)

Fat tissues were isolated from 8-week-old male C57/Bl6J mice, which were housed for 7 days either at 23°C or 4°C. Next, microdialysis membranes were implanted. Subsequently, tissues were transferred to 37°C tempered oxygen saturated microdialysis buffer (Table 17) in myograph chambers. Tissues were perfused with perfusion fluid at a flow of 1µl/min for 2.5 hours ('washout-phase') using a syringe pump. Afterwards, perfusion was continued with 10mM NE solution in perfusion fluid and the flow through was collected in Eppendorf tubes every 30 minutes (flow:1µl/min) over 2 hours. Adenosine, inosine and hypoxanthine

---

[1] DatLab7, © 2021 Oroboros Instruments GmbH · Commercial Register No: 193145m, Schoepfstrasse 18, A-6020 Innsbruck, Austria

concentrations of the dialysate were measured using a UPLC-TUV system as described in section 3.9.

Table 17 Microdialysis buffer

Substance	Quantity
NaCl	23mM
KCl	100mM
Na_2HPO_4	1,2mM
$MgCl_2$	1,2mM
$CaCl_2$	1,6mM
Hepes	24mM
Glucose	10mM
H_2O	1000ml

Substances were dissolved in H_2O and the pH was adjusted to 7.54. Afterwards, the buffer was stored at 4°C.

3.1.13. Immunohistochemistry

The following list provides an overview of the materials and equipment used for immunohistochemistry:

- DAB peroxidase substrate kit (Biozol Diagnostica, Cat. No. SK-4100)
- Di-Sodium hydrogen phosphate (Roth, Cat. No. P030.1)
- Embedding tray (Leica)
- Eozyn Y solution (Sigma-Aldrich, Cat. No. HT110216)
- EVOS® FL Color Imaging System (Thermo-Fischer Scientific)
- Hematoxylin solution according to Mayer (Sigma-Aldrich, Cat. No. 51275)
- Hydrogen peroxide (H_2O_2) 30% (Roth, Cat. No. 9681.1)
- Immu-Mount® (ThermoFisher Scientific, Cat. No. 9990402)
- Menzel™ Microscope Coverslips (ThermoFisher Scientific, Cat. No. 11778691)
- Microtome: HM335E Rotary microtome (Microm)
- ParaFree disposable base mold (Leica, Cat. No. 39LC-705-1)
- Paraplast® (Carl Roth, Cat. No. 39602004)
- Potassium dihydrogen phosphate (Roth, Cat. No. 3904.1)
- Roti®histokitt (Carl Roth, Cat. No. T1602)
- Signal Stain Boost IHC Det. (HRP. Rab) (Cell Signaling, Cat. No. 8114S)
- Simport™ Scientific unisette™ Tissue Processing/Embedding Cassette (ThermoFisher Scientific, Cat. No. 11655610)
- Tissue embedding station: Embedding Center/ Dispenser & Hot plate EG1160 (Leica)
- Tri-Sodium citrate dihydrate ($C_6H_5O_7Na_3x2H_2O$) (Roth, Cat. No. 3580.1)
- Tween® 20 (Roth, Cat. No. 9127.2)
- UCP1 Antibody (ThermoFisher Scientific, SKU: HAB2110, Project: QRK1280 - PA9514)

3.1.13.1. Preparation of paraffin sections

Isolated organs were placed in a cassette and immediately fixed in 4% PFA (Table 18) at 4°C (for a maximum of 16h). Afterwards, fixed tissue samples were washed with PBS (Table 19) twice for 5 minutes each. Next, samples were washed three times with 50% ethanol and afterwards three times with 70% ethanol, for 20 minutes each, at 4°C under gentle agitation. Subsequently, the tissue samples were placed three times in 95% ethanol for 20 minutes, followed by three times 20 minutes in 100% ethanol at RT to complete dehydration. Finally, tissues were incubated three times in xylol at RT for 10 minutes. Afterwards, samples were placed in liquid paraplast and incubated twice for 1 hour at 60°C, followed by incubation overnight in a beaker containing fresh liquid paraplast. On the next day, samples were embedded in base molds, containing paraplast, and stored at RT. The obtained paraplast blocks were cut into 4μm thick sections using a microtome, then shortly warmed in a water bath before placed on a slide. Subsequently, slides were dried overnight at 42°C in an incubator.

Table 18 PFA 4%

Substance	Quantity
Paraformaldehyde	40g
PBS	960ml

PFA was dissolved under stirring at 55°C and afterwards stored at 4°C.

Table 19 Phosphate buffered saline (PBS)

Substance	Quantity
NaCl	137nM
Na_2HPO_4	8mM
KH_2PO_4	1.4mM
KCl	2.7mM

Substances were dissolved in H_2O and the pH was adjusted to 7.4. Afterwards, the solution was autoclaved.

3.1.13.2. Hematoxylin & Eosin (H&E) staining

H&E histological staining was performed to visualize cell morphology and distinguish between the nuclear and cytoplasmic parts. Hematoxylin stains the nucleic acids in the cell nuclei blue, while eosin stains the cytoplasm and extracellular matrix pink-purple.

To deparaffinize the tissue sections, incubation in xylol was performed twice, for 2 minutes each. Next, the slides were rehydrated by incubation in three changes of 100%, 90%, 80%, 70%, 50% ethanol and PBS for 2 minutes, respectively. Afterwards, the tissue sections were incubated in hematoxylin solution for 10 minutes, followed by a 15-minute wash step with tap water. Subsequently, slides were dipped into a beaker containing eosin solution for 1 minute and washed three times with tap water for 1 minute each. Lastly, samples were dehydrated by incubation in 50%,75%,95%,100% ethanol for 2 minutes each and mounted using Roti® histokit. Pictures of dried slides were taken with EVOS® FL Color Imaging System at 20x and

40x magnification. Quantification of cell size in H&E-stained tissue sections was analyzed and calculated using ImageJ2 software[2]. Contrast and brightness of the pictures were adjusted using Canvas 11 sofware[3].

3.1.13.3. UCP1 staining

To prepare the histological staining of UCP1 protein, tissue sections were deparaffinized and rehydrated by incubation in three changes of xylol, 100% ethanol, 96% ethanol and 75% ethanol for 5 minutes each. Next, samples were washed twice in water for 5 minutes. Antigen retrieval was achieved by incubation in 20mM and 10mM sodium citrate solutions (Table 20) for 20 minutes at 75-80ºC. Afterwards, slides were washed with deionized water (dH$_2$O) three times for 5 minutes each. To quench endogenous peroxidases, slides were incubated in 3% hydrogen peroxide (H$_2$O$_2$) (Table 21) for 10 minutes, followed by washing in dH$_2$O for 5 minutes. To prevent unspecific binding, sections were incubated in blocking buffer (Table 22) in a humid chamber for 1 hour. Next, an UCP1 antibody dilution (1:500) (Table 23) was applied to the slides. Samples were incubated at 4ºC in a humid chamber overnight. On the next day, slides were washed three times with PBS-T (Table 24) for 5 minutes to remove the first antibody. Subsequently, secondary HRP anti rabbit antibody was applied, and the sections were incubated at RT for 1 hour. Next, the slides were washed three times with PBS-T for 5 minutes and developed using 3,3'-Diaminobenzidine (DAB) kit following the manufacturer's instructions. Roti® histokit was used to mount the stained tissue sections. Lastly, after tissue sections were dried, pictures were taken using EVOS® FL Color Imaging System at 20x and 40x magnification. Contrast and brightness of the pictures were adjusted using Canvas 11 sofware[3].

Table 20 20mM Sodium citrate dihydrate pH6

Substance	Quantity
C$_6$H$_5$O$_7$Na$_3$x2H$_2$O	5.882g
dH$_2$O	1000ml

The pH was adjusted using HCl. The solution was stored at RT. 20mM solution was diluted 1:1 in dH$_2$O to obtain a 10mM solution.

Table 21 Hydrogen peroxide solution 3%

Substance	Quantity
H$_2$O$_2$ 30%	20ml
dH$_2$O	180ml

Table 22 Blocking buffer

Substance	Quantity
Tween ® 20	0.1%
Normal goat serum (NGS)	2.5%

Substances were diluted in PBS.

---

[2] ImageJ2, Rasband, W.S., U. S. National Institutes of Health, Bethesda, Maryland, USA
[3] Canvas 11; © 1985-2007 ACD Systems of America, Inc., Seattle, WA 98109, USA

Table 23 Antibody solution

Substance	Quantity
Tween ® 20	0.1%
Normal goat serum (NGS)	0.25%

Substances were diluted in PBS.

Table 24 PBS-T

Substance	Quantity
Tween ® 20	0.1%

Tween was diluted in PBS. The solution was stored protected from light at RT.

3.2. Cell culture

The following list provides an overview of the materials and equipment used for cell culture:

- 3,3′,5-Triiodo-L-thyronine sodium salt (Sigma-Aldrich, Cat. No. T6397)

- 3-Isobutyl-1-methylxanthine (IBMX; Sigma-Aldrich, Cat. No. I5879)

- 6-well TC plates (Sarstedt, Cat. No. 83.3920)

- 6-well TPP plates (TPP Techno Plastic Products AG, Cat. No. 92406)

- 10 cm^2 TC dishes, Standard (Sarstedt, Cat. No. 83.3902)

- 12-well TC plates (Sarstedt, Cat. No. 83.3921)

- 12-well TPP plates (TPP Techno Plastic Products AG, Cat. No. 92412)

- Autoclave, Varioklav 135 T (Faust)

- Bovine Serum Albumin (BSA; Sigma-Aldrich, Cat. No. A7030)

- Canulaes (Braun, Sterican 0,90 x 40 mm, Cat. No. 4657519)

- Centrifuge, Biofuge Primo (Heraeus)

- Collagenase, Type II (Worthington, Cat. No. CLS2)

- Conical tubes, 15 ml and 50 ml volume (Sarstedt, Cat. No. 62.554.502, 62.547.254)

- Countess Automated Cell Counter (Invitrogen, Cat. No. C10227)

- Cryogenic vials (Sarstedt, Cat. No. 72.379.992)

- Dexamethasone (Sigma-Aldrich, Cat. No. D4902)

- Dimethyl sulfoxide (DMSO; Roth, Cat. No. A994)

- Dulbecco's Modified Eagle's Medium (DMEM), high glucose, GlutaMAX(TM) (Gibco, Cat. No. 31965)

- DMEM, high glucose, GlutaMAX(TM), pyruvate (Gibco, Cat. No. 61966)

- DMEM/F-12 (1:1) (Gibco, Cat. No. 11039-047)

- Fetal Bovine Serum (FBS) (Biochrom, Cat. No. S0015)

- FGF-1 (rh) (Immuno Tools, Cat. No. 11343555)

- Human Transferrin (Lonza, Cat. No. CC-4205)

- Incubator, HERAcell® 150 (Heraeus)

- Insulin solution human (Insulin; Sigma-Aldrich, Cat. No, I9278)

- Laminar air flow, Herasafe^{TM} (Heraeus)

- Microscope, LEICA DMIL (Leica Microsystems GmbH)

- 30 µM and 100 µM nylon meshes (Millipore, Cat. No. NY3002500, NY1H00010)
- Penicillin/streptomycin (P/S) (Merck, Cat. No. A2213)
- PBS (see section 3.2.12)
- Reaction tube 1.5 mL (Sarstedt, Cat. No. 72706)
- Rosiglitazone (Sigma-Aldrich, Cat. No. R2408)
- Scissors, forceps (Fine science tools)
- Serological pipettes 5ml, 10ml, 25ml (Sarstedt, Cat. No. 86.1253.001, 86.1254.001, 86.1685.001)
- Syringe filter 0.22 µm (VWR, Cat. No. 514-0061)
- Syringes 5 mL (BD Discardit II, Cat. No. 309050)
- T175 tissue culture flasks (Sarstedt, Cat. No. 83.3912.002)
- Trypan Blue Stain (Gibco, Cat. No. 15250)
- Trypsin-EDTA (0.05 %), phenol red (Trypsin; Gibco, Cat. No. 25300054)

3.2.1. Cell culture of BA

BA described in section 4.1, 4.2 and 4.3 were isolated from interscapular BAT of neonatal C57BL/6 mice.

Experiments of section 4.4 were performed with BA isolated from interscapular BAT of neonatal ENT1-WT and -KO littermates or ENT1floxed-AdiponectinCre homozygote floxed, Cre-negative (ENT1$^{fl/fl}$ Cre-) mice and homozygote floxed, Cre-positive (ENT1$^{fl/fl}$ Cre+) littermates.

BA used for experiments in section 4.5 were isolated from interscapular BAT of neonatal A2B-WT and -KO littermates.

3.2.1.1. Isolation and immortalization of BAT derived brown preadipocytes

Interscapular BAT was dissected from newborn mice, chopped with surgical scissors in 3 mL of BA isolation buffer (Table 25) and incubated in a water bath for 30 minutes at 37°C. Subsequently, samples were shaken every 5 minutes to enable equal digestion. After dissociation of BAT, remaining pieces were filtered out using a 100 µM nylon mesh. The resulting cell suspension was collected and incubated on ice for 30 minutes. Afterwards, the middle phase was filtered a second time, through a 30 µM nylon mesh, and the filtrate was centrifuged for 10 minutes at 700g. The obtained pellet was re-suspended in 2 mL of BA culture medium (Table 26) and plated in a 6-well TC plate, followed by incubation for 24 hours at 37°C and 5% CO_2. Eventually, cells were immortalized using 200 ng of Simian Virus 40 (SV40) large T-antigen per well, containing a phosphoglycerate kinase (PGK) promoter.

Table 25 BA isolation buffer

Substance	Quantity
NaCl	123 mM
KCl	5 mM
CaCl$_2$	1.3 mM
Glucose	5 mM
HEPES	100 mM
BSA	1.5%
Collagenase II	2 mg/ml

Substances were dissolved in H$_2$O, the pH was adjusted to 7.4 and the solution was sterile filtered. BSA and collagenase type II were added freshly before use and the solution was sterile filtered again.

Table 26 BA culture medium

Substance	Quantity
FBS	10 %
HEPES	10 mM
Insulin	4 nM
P/S	1 %
Sodium-Ascorbat	25 µg/ml
T3	4 nM

Chemicals were dissolved in DMEM, high glucose, GlutaMAX(TM), (Gibco, Cat. No. 61965).

3.2.1.2. Expansion and storage of brown preadipocytes

Immortalized cells were grown in BA growth medium (Table 27) until ~90% confluency. Next, cells were washed two times with PBS at RT and detached by adding Trypsin, followed by incubation for 3 minutes at 37°C. Subsequently, trypsin was inactivated by adding BA growth medium. The obtained cell suspension was centrifuged at 1000 rpm for 5 minutes. Afterwards, the pellet was re-suspended in BA growth medium. The number of cells was counted using Trypan Blue Stain and Countess Automated Cell Counter and the cells were either re-seeded in 10 cm^2 TC dishes at a ratio of 1:10 or frozen in cryogenic vials with BA growth medium containing 10% DMSO. Vials were stored at -80°C for 24 hours and subsequently transferred to -150°C. BA were used for experiments in passage 4.

Table 27 BA growth medium

Substance	Quantity
FBS	10 %
P/S	1 %

Supplements were added to DMEM, high glucose, GlutaMAX(TM) (Gibco, Cat. No. 61965).

3.2.1.3. Differentiation of BA

Scheme 8 provides an overview of the differentiation protocol of BA. Cells were seeded (day -4) on TC plates in BA growth medium at a density of ~160.000 cells per 6-well or ~80.000 cells per 12-well. Two days after seeding (day -2), BA growth medium was changed to BA differentiation medium (Table 28). After two further days (day 0) of incubation at 37°C and 5% CO$_2$, the medium was replaced by BA induction medium (Table 29) initiating the differentiation

program of preadipocytes to mature BA. Afterwards, cells were cultured in BA differentiation medium from day 2 until day 7, while the medium was replaced every second day. All experiments were performed on day 7 with mature BA.
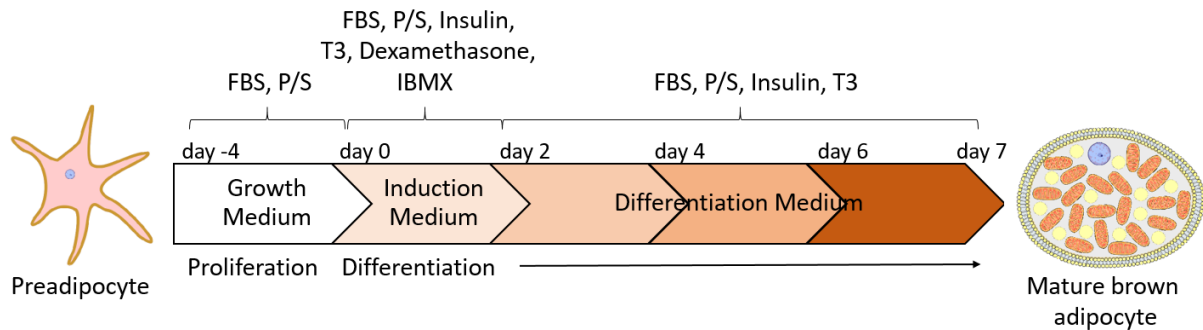
Scheme 8 Differentiation protocol for BA

Table 28 BA differentiation medium

Substance	Quantity
FBS	10 %
Insulin	1 nM
P/S	1 %
T3	20 nM

Substances were added to DMEM, high glucose, GlutaMAX(TM) (Gibco, Cat. No. 61965).

Table 29 BA induction medium

Substance	Quantity
Dexamethasone	1 µM
IMBX	0.5 mM

Supplements were added to BA differentiation medium.

3.2.2. Cell culture of primary BA

Cells were isolated from interscapular BAT of 8- to 10-week-old C57BL/6 mice. Cell culture methods applied for isolation, storage and differentiation were the same as those for BA from interscapular BAT of neonatal mice described in section 3.2.1, with the only difference that cells were not immortalized and directly expanded in 10 cm^2 TC dishes. Cells were used for experiments as primary cells without passaging.

3.2.3. Cell culture of WA

WA described in section 4.1 and 4.2 were isolated from inguinal WAT (WATi) of 8- to 10-week-old C57BL/6 mice.

Experiments of section 4.4 were performed with WA isolated from WATi of 8- to 10-week-old ENT1-WT and -KO littermates or ENT1floxed-AdiponectinCre homozygote floxed, Cre-negative (ENT1$^{fl/fl}$ Cre-) mice and homozygote floxed, Cre-positive (ENT1$^{fl/fl}$ Cre+) littermates.

WA used for experiments in section 4.5 were isolated from inguinal WAT of 8- to 10-week-old A2B-WT and -KO littermates.

3.2.3.1. Isolation and storage of WATi derived preadipocytes

For WA isolation inguinal WAT (WATi) depots of 8- to 10-week-old mice were dissected. Tissues were washed with cold DMEM (high glucose, GlutaMAX(TM), pyruvate) and cut into small pieces using surgical scissors. Next, 7 mL of WA isolation buffer (Table 30) were added to 1g of tissue. The suspension was incubated at 37°C and shaken vigorously every 5 minutes to ensure complete digestion. Afterwards, 7 mL of WA growth medium (Table 31) were added to stop collagenase activity. Following 10 minutes of incubation at RT, cells were centrifuged for another 10 minutes at 1000 rpm. Subsequently, the supernatant was siphoned and the pellet was re-suspended in 2 mL of WA growth medium. The suspension was filtered through a 100 µM nylon mesh, filled up with WA growth medium to 25ml and transferred into a T175 culture flask. Two days after seeding, cells were washed with PBS and fresh WA growth medium was added. Cell culture was maintained with WA growth medium, which was changed every second day until cells reached confluency.

Confluent cells were washed with PBS (RT) and detached by adding trypsin and incubation for 5 minutes at 37°C. Afterwards, WA growth medium was added to inactivate trypsin. Cells were collected and centrifuged for 10 min at 1000 rpm. The obtained cell pellet was re-suspended in WA growth medium. The number of cells was counted using Trypan Blue Stain and Countess Automated Cell Counter. This was followed by either seeding of WA in TPP plates or freezing in cryogenic vials with WA growth medium containing 10% DMSO. Vials were stored at -80°C for 24 hours, before being transferred to -150°C.

Table 30 WA isolation buffer

Substance	Quantity
BSA	0.5 %
Collagenase, Type II	1.5 mg/ml

Substances were dissolved in DMEM, high glucose, GlutaMAX^{TM}, (+) pyruvate (Gibco, Cat. No. 61966).

Table 31 WA growth medium

Substance	Quantity
FBS	10 %
P/S	1 %

Substances were added to DMEM, high glucose, GlutaMAX^{TM}, (+) pyruvate (Gibco, Cat. No. 61966).

3.2.3.2. Differentiation of WATi derived preadipocytes

Scheme 9 provides an overview of the differentiation protocol of WA. Initially, 150.000 cells per well were seeded in a 6-well TPP plate or 80.000 cells per well in a 12-well TPP plate. Cells were cultured to confluency in WA growth medium (day -4 till day 0). Four days later (day

0), the medium was changed to WA induction medium (Table 32) for 48 hours. Subsequently, WA were differentiated in WA maintenance medium (Table 33) and the medium was changed every second day until day 12. All experiments were performed on day 12 of the differentiation protocol.
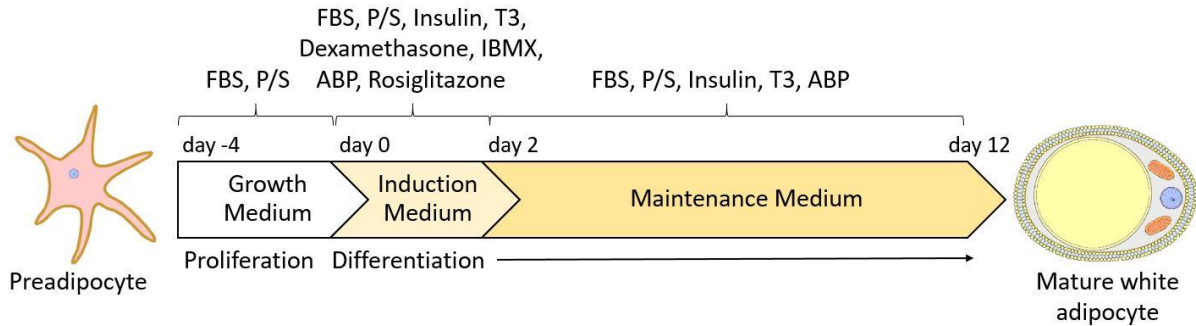
Scheme 9 Differentiation protocol for WA

Table 32 WA induction medium

Substance	Quantity
Dexamethasone	0.25 mM
IMBX	0.5 mM
Rosiglitazone	1 µM

Supplements were added to WA maintenance medium (Table 33).

Table 33 WA maintenance medium

Substance	Quantity
D-biotin	1 mM
FBS	5 %
Insulin	0.17 mM
L-ascorbate	50 mg/ml
P/S	1 %
Pantothenate	17 mM
T3	1 nM

Substances were added to DMEM, high glucose, GlutaMAX^{TM}, (+) pyruvate (Gibco, Cat. No. 61966).

3.2.4. Cell culture of primary human brown adipocytes (hBA)

Stromal vascular fraction cells from human supraclavicular brown adipose tissue biopsies (Ethical registration no. 076/18) were isolated by the technical assistances of our working group as previously described (Jespersen et al., 2013). Differentiation of hBA was performed by myself.

For differentiation 500000 hBA were seeded in hBA proliferation medium (Table 34) on a 12-well plate, the proliferation medium was changed every second day till the cells reached confluency. Two days *post* 100% confluences hBA were induced by changing the medium to hBA induction medium (Table 36). Three days after induction, hBA differentiation medium (Table 35) was added to the cells, before 200nM rosiglitazone was added to this medium.

Afterwards the differentiation was maintained for nine further days by changing the medium to fresh hBA differentiation medium (Table 35) every third day.

Table 34 hBA proliferation medium

Substance	Quantity
FBS	10 %
P/S	1 %
FGF-1	1nM

Substances were added to DMEM/F-12 (Gibco, Cat. No. 11039-047).

Table 35 hBA differentiation medium

Substance	Quantity
P/S	1 %
Dexamethasone	0.1µM
Insulin	100nM
T3	2nM
Transferrin	10µg/ml

Substances were added to DMEM/F-12 (Gibco, Cat. No. 11039-047).

Table 36 hBA induction medium

Substance	Quantity
Rosiglitazone	200nM
IBMX	540µM

Substances were added to hBA differentiation medium (Table 35).

3.3. Oil Red O staining

The following list provides an overview of the materials and equipment used for Oil Red O staining:

- Oil Red O (Sigma-Aldrich, Cat. No. O9755)
- Paraformaldehyde (PFA) (Roth, Cat. No. 0335.3)
- PBS (see table 19)
- 2-Propanol (Roth, Cat. No. 6752.4)

Mature BA and WA were washed twice with PBS (Table 19) and fixed with PFA 4% (Table 18) for 15 minutes at RT. After removal of PFA 4%, cells were washed twice with PBS. Subsequently, cells were covered with Oil Red O working dilution (Table 37) and incubated for 2 hours at RT. Afterwards, staining dilution was washed off with distilled water, plates were dried, before pictures were taken using a standard office scanner.

Table 37 Oil Red O stock solution (5mg/ml) and working dilution

Substance	Quantity
Stock solution	
Oil Red O	0.5g
Isopropanol 99%	100ml
Working dilution	
Oil Red O stock solution	6ml
H_2O	4ml

Dye and isopropanol were mixed and stirred overnight. Afterwards the stock solution was stored at RT. Before usage, Oil Red O stock solution was diluted freshly in a ratio of 3:2 with H_2O and filtered two times through filter papers.

3.4. Analysis of intracellular cAMP concentrations

The following list provides an overview of the materials and equipment used for analysis of intracellular cAMP concentrations:

- Adenosine (Sigma-Aldrich, Cat. No. A4036)
- Direct cAMP ELISA Kit (Enzo, Cat. No. ADI-901-066)
- Enspire® microplate reader (Perkin Elmer, Cat. No. 2300-0000)
- Hypoxanthine (Sigma-Aldrich, Cat. No. H9377)
- Inosine (Sigma-Aldrich, Cat. No. I4125)
- L- (−)-Norepinephrine (+)-bitartrate salt monohydrate (NE) (Sigma-Aldrich, Cat. No. A9512)
- PBS (see table 19)
- PSB 603 (Tocris, Cat. No. 3198)
- Reaction tube 1.5 mL (Sarstedt, Cat. No. 72706)

If inhibitors or antagonists were used, cells were pre-incubated with the respective compound for 10 minutes, before mature cells were stimulated with adenosine, inosine, hypoxanthine or NE for 15 minutes. Afterwards, cells were quickly washed with PBS and lyzed using 0.1M HCl. Subsequently, samples were analyzed using Direct cAMP ELISA Kit, following the manufacturer´s instructions. Measurements of optical density were performed at 405nm using a plate reader (Perkin Elmer).

3.5. *In vitro* lipolysis

The following list provides an overview of the materials and equipment used for *in vitro* lipolysis:

- 96-well plates (Sarstedt, Cat. No. 83.3924)
- Adenosine (Sigma-Aldrich, Cat. No. A4036)
- Adenosine 5'-(α,β-methylene)diphosphate (Sigma-Aldrich, Cat. No. M3763)
- Adenosine 5'-monophosphate sodium salt (AMP) (Sigma-Aldrich, Cat. No. A1752)
- Bovine serum albumin (BSA) (Sigma-Aldrich, Cat. No. A7030)
- CL-316243 disodium salt (abcam, Cat. No. 144605)
- DMEM (Gibco, Cat. No. 21063)
- Enspire® microplate reader (Perkin Elmer, Cat. No. 2300-0000)
- Free glycerol reagent (Sigma-Aldrich, Cat. No. F6428)

- Glycerol standard (Sigma-Aldrich, Cat. No. G7793)
- Incubator, HERAcell® 150 (Heraeus)
- Hypoxanthine (Sigma-Aldrich, Cat. No. H9377)
- Inosine (Sigma-Aldrich, Cat. No. I4125)
- L- (−)-Norepinephrine (+)-bitartrate salt monohydrate (NE)(Sigma-Aldrich, Cat. No. A9512)
- Levamisole hydrochloride (Acros Organics, Cat. No. 10666202)
- Reaction tube 1.5 mL (Sarstedt, Cat. No. 72706)

Mature adipocytes were washed twice with lipolysis medium (Table 15) and wells were refilled with 300µl of lipolysis medium, followed by incubation for 2 hours at 37°C and 5% CO_2 in absence and presence of selected compounds. Afterwards, free glycerol content of the conditioned lipolysis medium was measured: 40µl of conditioned lipolysis medium were pipetted in duplicates on a 96-well plate and 60µl of Free Glycerol Reagent were added. Glycerol standard wells were prepared mixing 5µl of glycerol standard with 95µl Free Glycerol Reagent (manufacturer´s instructions). Subsequently, the plate was incubated for 5 minutes at 37°C. Absorption was measured at 540nm, and 600nm as reference wavelength, using a microplate reader (Perkin Elmer). Calculation of glycerol content was carried out (see section 3.1.10 for formula). Results were normalized to protein concentrations (see section 3.7.1 for measurement of protein concentrations).

3.6. RNA methods

The following list provides an overview of the materials and equipment used for RNA analysis:

- Centrifuge (Eppendorf, Cat. No. 5415R)
- Chloroform (Roth, Cat.No. 6340.1)
- Diethylpyrocarbonate (DEPC; Roth, Cat. No. K028.1)
- Ethanol (EtOH) (Roth, Cat.No. 9065.4)
- InnuSOLV RNA Reagent (Analytik Jena AG, Cat. No. 845-SB-2090100)
- Nanodrop200 Spectrophotometer (ThermoScientific)
- 2-Propanol (Roth, Cat.No. 6752.4)
- Reaction tube 1.5 mL (Sarstedt, Cat. No. 72706)
- Real-time PCR machine, HT7900 (Applied Biosystems)
- SYBR-Green PCR master mix (Applied Biosystems, Cat. No. 4309155)
- Thermocycler Biometra TOne (Analytik Jena)
- Thermomixer comfort (Eppendorf, Cat. No. 2050-120-04)
- Protoscript® II First Strand cDNA Synthesis Kit (New England BioLabs, Cat. No. E6560S)
- Ultra-Turrax®, T8, IKA, Staufen

3.6.1. Isolation of RNA

RNA from cells or tissues was isolated using innuSOLV RNA Reagent. 1ml of innuSOLV RNA Reagent was added to lyze the cells. Tissue samples were homogenized using Ultra-Turrax®,

before innuSOLV RNA Reagent was added. Next, lysates were transferred to a reaction tube and 200µl cold chloroform were added to each sample. Afterwards, samples were vigorously shaken for 15 seconds and incubated for 5 minutes at RT. This was followed by centrifugation at 4°C and 13000rpm for 20 minutes, separating fat, protein and DNA from the upper phase containing the RNA. The upper phase was transferred to a new reaction tube and mixed with 500µl of cold isopropanol to precipitate the RNA. RNA was pelleted by centrifugation at 4°C and 13000rpm for 10 minutes. Next, the supernatant was removed and the pellet was washed twice with 75% EtOH (in DEPC-H$_2$O). Finally, the RNA pellet was air dried and dissolved in 30-50µl DEPC-H$_2$O. RNA concentration was quantified using Nanodrop Spectrophotometer.

3.6.2. Synthesis of complementary DNA (cDNA)

1000ng of RNA were transcribed to cDNA using Protoscript® II First Strand cDNA Synthesis Kit and following the manufacturer's instructions. Table 38 shows the thermocycler program used:

Table 38 cDNA synthesis program

Step	Time [min]	Temperature [°C]
1	5	25
2	60	42
3	5	80
4	∞	4

Afterwards, the obtained cDNA was diluted to a final concentration of 2.5 ng/µl.

3.6.3. mRNA analysis using Quantitative Real Time Polymerase Chain Reaction (qRT-PCR)

12.5ng of cDNA were mixed with 5µl of SYBR Green PCR mastermix and the respective primer pair [1µM] (Table 39). qRT-PCR was performed using a HT7900 instrument (Applied Biosystems) with the amplification program shown in Table 40. Quantification of mRNA was performed applying the Second Derivative Maximum Method. The cycle threshold (CT) is defined as the fractional cycle number in the log-linear region of target amplification (Guescini et al., 2008). The automated Second Derivative Maximum Method calculates this fractional cycle where the second derivative of the real-time fluorescence intensity curve reaches the maximum value (van Luu-The et al., 2005). Hypoxanthine-guanine-phosphoribosyltransferase (*Hprt*) amplification was measured as an internal control. In Table 39 the primer sequences, which were designed for murine template cDNA and used for amplification of the target genes, are shown.

Table 39 List of primers used for qRT-PCR

Target	Forward (5´- 3´)	Reverse (5´- 3´)
Cox8b	GAACCATGAAGCCAACGACT	GCGAAGTTCACAGTGGTTCC
Fabp4	GCGTGGAATTCGATGAAATCA	CCCGCCATCTAGGGTTATGA
Hprt	GTCCCAGCGTCGTGATTAGC	TCATGACATCTCGAGCAAGTCTTT
Nd5	AGCATTCGGAAGCATCTTTG	TTGTGAGGACTGGAATGCTG
Ndufa1	AGACGCATCTCTGGTGTCAA	GCCAGGAAAATGCTTCCTTA
Pparg	ACAAGACTACCCTTTACTGAAATTACCAT	TGCGAGTGGTCTTCCATCAC
Ppargc1a	GCACACACCGCAATTCTCCCTTGTA	ACGCTGTCCCATGAGGTATTGACCA
Prdm16	AGACCGAAGACGGCATCCT	CGTAGCTCGAAGTCTGGTGG
Slc29a1	AGTCACCAGCCTCAGGACAG	GGACACGTCCAGGCGGTT
Slc29a2	CGGGACAGCTACCACCTG	GCGTGAAGAGCAGTAGAGGC
Ucp1	GGCCTCTAGGACTCAGTC	TAAGCCGGCTGAGATCTTGT

Primer pair quality was assessed by analysis of respective melting curves.

Table 40 qRT-PCR program

Step	Time [s]	Temperature [°C]	
1	600	95	
2	15	95	Steps 2 and 3 were
3	60	60	repeated for 40 cycles

Melting curve:

Step	Time [s]	Temperature [°C]
4	1	95
5	15	65
6	-	95

3.6.4. NGS-mRNA-sequencing

The following list provides an overview of the materials and equipment used for NGS-mRNA-sequencing:

- BSA (Sigma-Aldrich, Cat. No. A7030)
- Collagenase, Type II (Worthington, Cat. No. CLS2)
- Centrifuge, Biofuge Primo (Heraeus)
- Centrifuge (Eppendorf, Cat. No. 5415R)
- DMEM, high glucose, GlutaMAX(TM) (Gibco, Cat. No. 31965)
- gentleMACS Octo Dissociator with Heaters (Miltenyi Biotec, Cat. No. 130-096-427)
- gentleMACS C Tubes (Miltenyi Biotec, Cat. No. 130-093-237)
- Equipment and material for RNA-Isolation (as described above)

BAT, WATi and WATg tissues were isolated from 20-week-old male C57/Bl6J mice, which were fed a control diet for 12 weeks. Tissues of two mice were pooled, chopped, transferred into a gentleMACS C-tube and 3ml of digestion buffer (Table 41) were added.

Table 41 Digestion buffer for gentleMACS Dissociator

Substance	Quantity
BSA	0.25g
Collagenase type II	0.16g
DMEM	40ml

Digestion buffer was prepared freshly before use by solving the substances in DMEM.

Adipose tissue was digested using a GentleMACS Octo tissue dissociator and the protocol 37C-mr-ATDK-1 (protocol for adipose tissue provided by the manufacturer). After dissociation, gentleMACS C tubes were centrifuged for 10 minutes at 300rcf. The floating fraction (Scheme 10), containing the mature adipocytes, was aspirated, transferred into a reaction tube and centrifuged again for 10 minutes at 300rcf. The remaining liquid phase was aspirated, discarded and 1ml of Trizol was added to the isolated mature adipocytes. Subsequently, the protocol for RNA-isolation was proceeded as described in section 3.6.1.
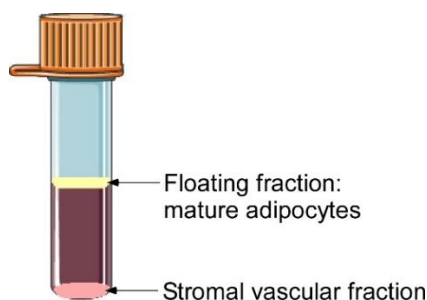
Scheme 10 Floating fraction and Stromal Vascular Fraction (SVF) of digested adipose tissue

NGS bulk 3'poly(A)-mRNA sequencing was performed by Dr. André Heimbach, NGS core facility, Medical faculty University Bonn. Bioinformatics data analysis was performed by Dr. Andreas Buness, Core Unit for Bioinformatics Data Analysis, Medical faculty University Bonn.

3.7. Protein methods

The following list provides an overview of the materials and equipment used for protein analysis:

- Acrylamide Rotiphorese® Gel 30 (37.5:1), (Roth, Cat. No. 3029.1)
- Alpha Tubulin Ab (Dianova, Cat. No. DLN-009993)
- Ammoniumperoxodisulphate (APS) (Roth, Cat. No. 9592.2)
- Anti-Calnexin, C-Terminal rabbit pAb (EMD Millipore Corp, Cat. No. 208880)
- Anti-mouse IgG (H+L) – Dylight 680™ (Cell Signaling, Cat. No. 5470S)
- Anti-rabbit IgG (H+L) – Dylight 800 ™ (Cell Signaling, Cat. No. 5151S)

Materials and methods

- aP2/FABP4 rabbit Ab (Cell Signalling, Cat. No. 2120S)
- BioPhotometer D30 (Eppendorf)
- Bovine Serum Albumin (BSA) (Roth GmbH, Cat. No. 8076.3)
- Bromophenol blue (Roth, Cat. No. T116.1)
- Cell scraper (Labomedic, Cat. No. 2015217)
- Centrifuge 5430R (Eppendorf)
- Color protein Broad Range (New England Bio Labs, Cat. No. 0021405)
- Complete protease inhibitor cocktail (Complete® EDTA free) (Roche, Cat. No. 04693116001)
- Coomassie brilliant blue G-250 (Merck, Cat. No. 1.15444.0025)
- Deoxycholic acid sodium salt (Roth, Cat. No. 3484.2)
- Ethanol (EtOH) (Roth, Cat. No.9065.4)
- Electrophoresis power supply, EV202 (Sigma-Aldrich)
- Electrophoresis/western blotting system: Mini Trans-Blot® Cell system (BioRad)
- Glas plates mini Protean® (Bio Rad, Cat. No. 1653312)
- Glycerol (Roth, Cat. No. 3908.3)
- 2-Mercaptoethanol (Sigma-Aldrich, Cat. No. M3148)
- Minispin centrifuge (Sigma-Aldrich, Cat. No. Z606235)
- Nitrocellulose blotting membranes (GE Lifesciences, Cat. No. A29434120)
- Nonidet® P 40 Substitute (NP-40) (Fluka BioChemika, Cat. No. 74385)
- N-N-N'-N'-Tetramethyl ethylene diamine (TEMED) (Sigma-Aldrich, Cat. No. T7024)
- Odyssey imaging system (LI-COR)
- Ortho-Phosphoric acid 85% (Roth, Cat. No. 6366.1)
- PBS (see section 3.2.12)
- PPARgamma rabbit mAb (Cell Signalling, Cat. No. 2430S)
- Reaction tube 1.5 mL (Sarstedt, Cat. No. 72706)
- Syringe filter 0.22 µm (VWR, Cat. No. 514-0061)
- Sodiumchloride (NaCl) (Roth, Cat. No. 3957.1)
- Sodium dodecyl sulphate (SDS) (Roth, Cat. No. 2326.2)
- Sodiumflouride (NaF) (Roth, Cat. No. 2618.1)
- Sodium orthovanadate (Na_3VO_4) (Roth, Cat. No. 0735.1)
- Thermomixer (Eppendorf)
- Tris (Roth, Cat. No. AE15.3)
- Tris HCl (Roth, Cat. No.9090.3)
- Ultrasonic bath (Bandelin)
- Ultra-Turrax® (T8, IKA, Staufen)
- UCP-1 rabbit Ab (Cell Signalling, Cat. No. 14670S)
- Whatman™ gel blot paper (GE Lifesciences, Cat. No. 10426892)

3.7.1. Isolation and quantification of proteins

Cells were washed with PBS and cold lysis buffer (Table 43) was added to the cells. Cells were scraped off the cell culture plates and transferred into a reaction tube, followed by incubation on ice for 15 minutes, sonication and centrifugation at 4°C and 13000rpm for 20 minutes. The clear middle phase was transferred into a new reaction tube and stored at -80°C or used directly.

In order to isolate proteins from tissue samples, explants were placed in a reaction tube and 250µl of cold lysis buffer were added. Next, the samples were homogenized using an Ultra-Turrax®. The next steps of isolation protocol were identical to protein isolation from cells as explained above.

Subsequently, 2µl of protein lysate were diluted in 98µl 0.15M NaCl solution and incubated with 1ml Coomassie solution (Table 44) for 1 minute at RT. Afterwards, absorbance was measured with a BioPhotometer at 595nm and protein amount was quantified using a BSA standard calibration curve, which was generated from several known BSA standard concentrations.

Table 42 RIPA buffer

Substance	Quantity
Deoxycholic acid sodium salt	0.5%
NaCl	150mM
NP-40	1.0%
Sodium dodecyl sulphate (SDS)	0.1%
Tris HCl (pH 7.5)	50mM

All substances were dissolved in Millipore H_2O. Afterwards, the solution was sterile filtered and stored at 4°C.

Table 43 Lysis buffer

Substance	Quantity
Complete® EDTA free	40µl/ml
NaF	10mM
Na_3VO_4	1mM

All substances were freshly added to RIPA buffer (Table 42) before use.

Table 44 Coomassie solution

Substance	Quantity
Coomassie brilliant blue G-250	0.01%
EtOH	5%
Phosphoric acid	8.5%

The components were dissolved in H_2O. The solution was stored at 4°C.

3.7.2. Sodium dodecyl sulphate polyacrylamide gel electrophoresis (SDS-PAGE) and Western Blot

Protein concentrations were adjusted to 50µg per sample by adding respective volumes of lysis buffer. Next, a 3-fold concentrated loading buffer (3x Laemmli, Table 45) was added to achieve a 1-fold final concentration. β-mercaptoethanol was added to the protein solution (1:20) to cleave disulfide bonds by reduction. Eventually, the samples were incubated at 95°C for 10 minutes to disrupt hydrogen bonds and thereby cancel the secondary and tertiary structures of the proteins.

Table 45 3x Laemmli buffer

Substance	Quantity
Bromophenol blue	0.015%
Glycerol	20%
SDS	17%
Tris-HCl (pH=6.8)	125mM

The components were dissolved in H_2O and the buffer was stored at -20°C.

3.7.2.1. Sodium dodecyl sulphate polyacrylamide gel electrophoresis (SDS-PAGE)

To perform discontinuous gel electrophoresis separating and stacking gels are poured on top of each other between two glass plates. The gels are produced by radical polymerisation. Acrylamide serves as gel-former, by adding N-N-N'-N'-Tetramethyl ethylene diamine (TEMED), as a catalyst, and ammoniumperoxodisulphate (APS), as a radical initiator, the polymerisation is started. The composition of the polyacrylamide gels is described in tables 46-47. After completion of polymerization, prepared protein solutions were loaded into the pockets of the stacking gel. SDS-PAGE was run in 1x electrophoresis buffer (Table 48) at 100V for 90-120 minutes at RT using the Mini Trans-Blot® Cell system.

SDS-PAGE is a discontinuous electrophoretic system, used for separation of proteins. By application of sodium dodecyl sulphate (SDS) and polyacrylamide, the influence of structure and charge of proteins can be eliminated, so that separation of proteins is mediated exclusively by the differences in their molecular masses. One SDS molecule per two amino acids binds to the proteins, thereby the proteins' intrinsic charges are masked and proteins are negatively charged with a stable charge-to-mass ratio. When a voltage is applied, proteins migrate to the anode. Firstly, they pass the stacking gel and accumulate at the interface between stacking and separating gel. Next, while passing the separating gel, the proteins are separated according to their molecular weights. The mashes of the gel act like a sieve: small proteins migrate faster through the gel and for larger proteins it is more likely to be retained.

Table 46 Composition of separating gels (10ml)

Substance	8%	10%	12%	15%
H_2O	4.6ml	4ml	3.3ml	2.3ml
30% Acrylamide	2.7ml	3.3ml	4ml	5ml
1.5M Tris (pH=8.8)	2.5ml	2.5ml	2.5ml	2.5ml
20% Ammoniumperoxodisulphate (APS)	0.05ml	0.05ml	0.05ml	0.05ml
N-N-N'-N'-Tetramethyl ethylene diamine (TEMED)	6µl	4µl	4µl	4µl

Table 47 Stacking gel (6ml)

Substance	Quantity
H_2O	3.4ml
30% Acrylamide	0.83ml
1M Tris (pH=6.8)	0.63ml
20% Ammoniumperoxodisulphate (APS)	0.05ml
N-N-N'-N'-Tetramethyl ethylene diamine (TEMED)	6µl

Table 48 10x Electrophoresis buffer

Substance	Quantity
Glycine	2M
SDS	0.1%
Tris	250mM

The substances were dissolved in H_2O and the pH was adjusted to 8.3. Before usage, electrophoresis buffer was diluted with H_2O to a final concentration of 1x.

3.7.2.2. Western Blot

After SDS-PAGE, Western Blotting was performed to transfer the proteins from the gel to a nitrocellulose membrane. Gels were placed in the Mini Trans-Blot® Cell system transfer setup: between sponges and Whatman papers with a nitrocellulose membrane on top of the gel. Next, proteins were transferred by application of a 300mA transverse electric field, in cold transfer buffer (Table 49) for 90 minutes. Upon completion of the transfer, membranes were washed with TBS-T (Table 51) and blocked in blocking buffer (Table 52) for 1 hour under constant agitation. Subsequently, membranes were incubated in primary antibody solution overnight at 4°C under gentle agitation. The 1:1000 dilutions of primary antibodies were prepared in blocking buffer. After this incubation step, the membranes were washed with TBS-T three times for 5 minutes each and incubated in appropriate fluorescence-labelled secondary antibody solutions (1:3000 dilution of secondary antibody in blocking buffer) for 1 hour at RT. Upon completion of incubation with the secondary antibody, the membranes were washed again with TBS-T, three times for 5 minutes. The protein bands were visualized using an Odyssey imaging system (LI-COR Bioscience) and quantified with Image Studio Lite 5.2 software[4], which was provided by the manufacturer. Afterwards, the membranes were stripped by applying stripping

---

[4] Image Studio Lite 5.2, LI-COR Biosciences, 4647 Superior Street, Lincoln, Nebraska USA

buffer (Table 53) for 2 minutes, washed three times with TBS-T for 5 minutes, blocked again and incubated with another primary antibody solution for the next protein of interest.

Table 49 1x Transfer buffer

Substance	Quantity
10x Electrophoresis buffer	10%
Methanol	20%
H_2O	70%

Table 50 10x Tris buffered saline (TBS)

Substance	Quantity
Tris	24.3g
NaCl	80g
H_2O	1000ml

The substances were dissolved in H_2O and the pH was adjusted to 8.0 using HCl.

Table 51 TBS-T (0.1%)

Substance	Quantity
Tween-20	1ml
10 x TBS (Table 50)	100ml
H_2O	900ml

Table 52 Blocking buffer

Substance	Quantity
BSA	5g
TBS-T (Table 51)	100ml

Table 53 Stripping buffer

Substance	Quantity
Glycine	2M
SDS	1%

The substances were dissolved in H_2O and the pH was adjusted to 2.0 using HCl.

3.8. Seahorse measurements

The following list provides an overview of the materials and equipment used for Seahorse measurements:

- Antimycin A (Sigma-Aldrich, Cat. No. A8674)
- Carbonyl cyanide-4 (trifluoromethoxy) phenylhydrazone (FCCP) (Tocris, Cat. No. 0453)
- CL-316243 disodium salt (abcam, Cat. No. 144605)
- Cytation 5 imaging reader (BioTek)
- D(+)-Glucose (Roth, Cat. No. X997.2)
- Hoechst 33258 (2′-(4-Hydroxyphenyl)-5-(4-methyl-1-piperazinyl)-2,5′-bi(1H-benzimidazol)) (Sigma-Aldrich, Cat. No. B2883)
- L-Glutamin (Roth, Cat. No. 3772.1)
- Oligomycin (Sigma-Aldrich, Cat. No. 495455)
- Rotenone (Sigma-Aldrich, Cat. No. R8875)
- Seahorse XFe24 Analyzer (Agilent)

- Seahorse XFe24 Fluxpak (Agilent, Cat. No. 102340-100)
- Seahorse XFe24 DMEM medium pH 7.4 (Agilent, Cat. No. 103575-100)
- Sodium pyruvate (Sigma-Aldrich, Cat. No. P2256)

Brown and white adipocytes were differentiated on 24-well microculture plates according to the standard protocols as explained in sections 3.2.1 and 3.2.3. On the day of the assay, mature adipocytes were washed twice with warm Seahorse medium (Table 54) and afterwards 500μl of Seahorse medium were added to each well. Next, the cells were incubated for 1 hour at 37°C in a non-CO_2-controlled environment. During this incubation step, the cartridge was loaded as listed in Table 55. To measure mitochondrial respiration Mito Stress Test (Agilent Technologies, Inc., 2019) was performed following manufacturer's instructions and using the assay protocol shown in Table 56. Firstly, basal respiration and respirometry after stimulation with the beta-3 adrenergic agonist CL-316243 were measured. This was followed by an injection of oligomycin, which inhibits ATP synthase (complex V), thereby decreasing electron flow through the Electron Transport Chain (ETC) and causing a reduction in mitochondrial respiration. This decrease in Oxygen Consumption Rate (OCR) is linked to cellular ATP production. Thirdly, FCCP was injected, this compound is an uncoupling agent, which demolishes the proton gradient interrupting the mitochondrial membrane potential. Thereby, an uninhibited electron flow through the ETC is possible, oxygen consumption by complex IV is maxed out and the respiratory chain operates at its maximal capacity. With the last injection a mixture of rotenone and antimycin A was administered. This mix of a complex I inhibitor (rotenone) and a complex III inhibitor (antimycin A) abolishes mitochondrial respiration, enabling the measurement of the non-mitochondrial respiration rate. Different parameters of mitochondrial respiration were calculated using Wave 2.6.0 software[5] and equations provided by the manufacturer. All results were normalized to Hoechst cell count of the respective well, which was performed right after the Mito stress assay using a Cytation 5 reader.

Table 54 Seahorse medium

Substance	Quantity
Glucose	25mM
Glutamin	2mM
Sodium pyruvate	2mM

The substances were dissolved in Seahorse XFe24 DMEM medium.

---

[5] Wave 2.6.0, Agilent, 5301 Stevens Creek Blvd., Santa Clara, CA 95051, USA

Table 55 Compounds used for the Seahorse assay

Compound	Stock conc.	Final Conc.	Solvent	Medium [µl]	Stock [µl]	Volume per well [µl]	Port
CL-316243	1mM	1µM	Seahorse medium	2475	25	56	A
Oligomycin	1.26mM	2µM	Ethanol 100%	2460	39.58	62	B
FCCP	20mM	1µM	Ethanol 100%	2500	1.25	69	C
Rotenone	10mM	0.5µM	DMSO 100%		1.25		
Antimycin A	20mM	0.5µM	Ethanol 100%	2500	0.625	75	D
Hoechst 33258	10mg/ml	50.8µg/ml	H$_2$O		12.7		

Table 56 Seahorse assay protocol

Condition	Number of cycles	mix-wait-measure [minutes]
Basal rate	3	3-2-2
Acute injection	4	3-2-2
Oligomycin	3	3-2-2
FCCP	3	3-2-2
Rotenone/Antimycin A	3	3-2-2

3.9. Analysis of extracellular ATP, ADP, AMP, adenosine, inosine and hypoxanthine concentrations

The following list provides an overview of the materials and equipment used for analysis of purinergic molecules:

- Acetonitrile (UPLC/MS-CC/SFC, Biosolve, Cat. No.0001204101BS)
- ACQUITY UPLC® H-Class System (Ultra Performance Liquid Chromatography) (Waters):
  -Quaternary Solvent Manager (QSM) (Waters, SN M15BQM529M)
  -bioSample Manager – FTN (Flow Through Needle) (Waters, SN A16BDI475M)
  -High Temperature Column Heater (HTCH-A) (Waters, SN A16CHA524G)
  -TUV Detector (tunable, dual wavelength ultraviolet/visible detector) (Waters, Cat. No. 176015028, SN K16TUV056A)
- Adenosine (Sigma-Aldrich, Cat. No. A4036)
- Adenosine 3',5'-cyclic monosphate (cAMP) (Sigma-Aldrich, Cat. No. A9501)
- Adenosine 5'-diphosphate sodium salt (ADP) (Sigma-Aldrich, Cat. No. A2754)
- Adenosine 5'-monophosphate sodium salt (AMP) (Sigma-Aldrich, Cat. No. A1752)
- Adenosine 5'-triphosphate (ATP): Lyophilized ATP Standard Solution (Perkin Elmer, Cat. No. ORT0621)
- ADP/ATP Ratio Assay Kit (Sigma-Aldrich, Cat. No. MAK135)
- CORTECS UPLC C18 Column, 90Å, 1.6 µm, 2.1 mm X 150 mm column (Waters, Germany, Part No. 186007096)
- ddH$_2$0 (Milli-Q Water Purification System)
- Dipyridamole (Sigma-Aldrich, Cat. No. D9766)

- Enspire® microplate reader (Perkin Elmer, Cat. No. 2300-0000)
- Glass inserts (Macherey & Nagel, Cat. No. 702813)
- Glass vials (Macherey & Nagel, Cat. No. 702283)
- HBSS (ThermoFisher, Cat. No. 14025-050)
- Hypoxanthine (Sigma-Aldrich, Cat. No. H9377)
- Inosine (Sigma-Aldrich, Cat. No. I4125)
- L-(−)-Norepinephrine (+)-bitartrate salt monohydrate (NE)(Sigma-Aldrich, Cat. No. A9512)
- Nunc™ 96-Well MicroWell™ plates (Thermo Fisher, Cat. No. 267350)
- Potassium chloride (KCl) (Roth, Cat. No. 6781.1)
- Potassium dihydrogen phosphate (KH_2PO_4) (Roth, Cat. No. 3904.1)
- Potassium hydroxide (KOH) (Merck, Cat. No. 1.05033.1000)
- Reaction tube 1.5 mL (Sarstedt, Cat. No. 72706)
- Thermomixer comfort (Eppendorf, Cat. No. 2050-120-04)
- Thermo Scientific Nalgene Filtration Products 0.45 SFCA (Thermo Fisher, Cat. No. 157-0045)
- Ultrasound Bath Sonotex TK52 (Bandelin)

3.9.1. Collection of conditioned medium

BA and WA were differentiated on 12-well plates. Afterwards, mature adipocytes were washed twice with 37°C warm HBSS and the wells were refilled with 300µl HBSS each. Next, plates were incubated for 45 minutes at 37°C. Subsequently, the plates we replaced on the bench and not moved for 15 minutes, because shaking leads to unspecific purine release, which would bias the measurements. If needed, adipocytes were treated with certain compounds, e.g. with NE [1µM]. After 0, 10, 30, 60, 90 and 120 minutes, 100µl of conditioned HBSS were taken off and immediately heat-inactivated in a thermomixer at 67°C for 5 minutes. Control samples of not treated cells were taken for all time points. Samples were stored at -20°C or directly analyzed using Waters ACQUITY UPLC TUV System.

3.9.2. Analysis of AMP, adenosine, inosine and hypoxanthine concentrations by UPLC-TUV

50µl of conditioned medium were transferred to a glass insert, which was placed in a glass vial on the UPLC sample plate. All samples were measured using a tunable UV/Vis-detector UPLC coupled system (Waters). A CORTECS UPLC C18 Column with silica as particle substrate, particle size of 1.6 µm and pore size of 90 Å was used, enabling a Reversed Phase separation mode. The UPLC method (Table 57) was applied for 30 minutes per sample starting with 100% of Eluent A (Table 58). After 8 minutes, a gradient was started by changing to 100% of Eluent B (Table 59), which contains 3% acetonitrile. 15 minutes later, the mobile phase was changed back to 100% of Eluent A. 8µl of each sample were injected and measured at a flow of 0.15ml/min. Recorded chromatograms were analyzed using Empower™ software[6] by

---

[6] Empower, Waters GmbH, Helfmann-Park 10, 65760 Eschborn, Germany

comparing retention times of external standards with the peaks of measured matrices. After integration of the identified chromatographic peaks, metabolites' concentrations were determined based on standard curves of respective substances (which represent the relationship between the concentration of a certain substance and its peak area).

Table 57 UPLC method

Time [minute]	Eluent A [%]	Eluent B [%]
0	100	0
8	100	0
8.1	0	100
23	0	100
23.1	100	0
30	100	0

Table 58 Eluent A: 0.15M KCl & 0.15M KH$_2$PO$_4$, pH 6.0

Substance	Quantity
KCl	11.183g
KH$_2$PO$_4$	20.413g
ddH$_2$O	1000ml

Chemicals were dissolved in ddH$_2$O and the pH was adjusted to 6.0 using KOH. Afterwards the solution was sterile filtered through a 0.45µm pore vacuum filter.

Table 59 Eluent B: 3% acetonitrile in 0.15M KCl & 0.15M KH$_2$PO$_4$, pH 6.0

Substance	Quantity
Eluent A	500ml
Acetonitrile	15.15ml

Standard mix:

A standard mix stock solution containing 5000nM adenosine, AMP, ADP, ATP, cAMP, inosine and hypoxanthine in HBSS was prepared.

Standard curve/ Calibration curve:

The standard mix stock solution was diluted with HBSS to 1000nM, 300nM, 200nM, 100nM and 50nM standard mixtures. Stock solution and dilutions were used to measure a standard curve. Pure HBSS was used as a blank measurement. 8µl of each standard concentration and blank were injected.

3.9.3. Analysis of ATP and ADP concentrations

40µl of conditioned medium and ATP-standard solutions of 0, 50, 100, 200, 300, 5000nM were pipetted to a 96-well plate. Reagents of the ADP/ATP Ratio Assay Kit were prepared following the manufacturer's instructions. In the first step, ATP reagent was added, followed by 1 minute of incubation at RT. Subsequently, to detect the ATP concentrations, luminescence was measured using an EnSpire™ plate reader. Afterwards, the plate was incubated for additional 10 minutes and read again to provide the background signal for the second step measurement.

In the latter measurement, ADP reagent was added and after 1 minute of incubation and mixing at RT, luminescence measurement was performed to detect ADP-concentrations.

The principle of this assay is based on luciferase catalyzed reaction: Luciferin is immediately oxidized in the presence of ATP, which leads to emission of light. Consequently, the measured luminescence intensity provides a direct measurement of ATP concentrations.

$$ATP + D\text{-Luciferin} + O_2 \xrightarrow{\text{Luciferase}} Oxyluciferin + AMP + PP_i + CO_2 + light$$
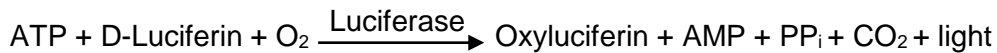
Source: (Sigma-Aldrich Corp., 2014)

Before the second step measurement, the ADP is converted to ATP by an enzymatic reaction. As in the first step measurement, the newly generated ATP reacts with the D-luciferin emitting light. The obtained luminescence intensity represents both ADP and ATP concentrations in the conditioned medium. Therefore, a background intensity must be measured right before starting the enzymatic reaction enabling calculation of the ADP concentration by subtraction of the background light intensity from the second step measurement. The background measurement represents the residual ATP signal.

3.10. Uptake of radioactive labelled inosine *in vitro*

The following list provides an overview of the materials and equipment used for measurements of ^{3}H-Inosine uptake:

- ^{3}H-Inosine (Hartmann Analytic, Cat. No. ART0738)
- Beckman Counter LS6500 (Beckman, SN 7069337, Instance No. 822725)
- Dipyridamole (Sigma-Aldrich, Cat. No. D9766)
- HBSS (ThermoFisher, Cat. No. 14025-050)
- PBS (Table 19)
- Polyethylene Vials (Perkin Elmer, Cat. No. PA6000288)
- Scintillation Fluid: Ultima Gold (Perkin Elmer, Cat. No. 6013329)
- Triton X (VWR, Cat. No. 28817.295)
- Waterbath (Köttermann)

BA were differentiated in 12-well plates. Mature BA were washed with HBSS and the wells were refilled with 900µl HBSS each. Afterwards, plates were transferred to a water bath in the isotope laboratory at 37°C and the cells were pre-incubated either with or without the ENT-inhibitor dipyridamole (1µM) for 15 minutes. Subsequently, 1µCi ^{3}H-inosine per well was added and the cells were incubated for additional 5 minutes. Afterwards, the supernatant was transferred to counter vials and 1ml of scintillation fluid was added. The cells were washed with PBS and lysed by adding 300µl Triton X dilution (1:1000 in HBSS). 2µl of the resulting lysate were used to measure the protein concentration *via* Bradford assay (see section 3.7.1). The rest of the protein lysate was transferred to a counter vial, and 2ml of scintillation fluid

were added. Counter vials, containing supernatant or cell lysates, were shaken vigorously and stored in the Beckman Counter, protected from light for 6 hours, before radioactivity was measured. Data were normalized to the protein concentrations of respective wells.

3.11. Statistical analysis

Statistical analyses were performed using GraphPad Prism 6 software[7]. For statistical comparison of two groups, unpaired (two-tailed) t-test was applied (GraphPad Software Inc., 2014). Comparisons of multiple groups were performed applying one-way ANOVA in combination with Tukey's post-hoc multiple comparisons test (GraphPad Software Inc., 2014). Analysis of covariance (ANCOVA) was carried out to control for bodyweight as a covariate. Empirical results are represented as mean ± standard error of the mean (SEM). Attained results were compared against p-values of 0.05, 0.01, 0.005 and 0.001 in order to analyze their significance; $p > 0.05$ was considered as not significant. Sample size 'n' represents, for each comparison group, either the number of mice or independently differentiated cell pools analyzed.

---

[7] GraphPad Prism 6, GraphPad Software LLC, 2365 Northside Dr., Suite 560, San Diego, CA 92108, USA

4. Results

First, purine concentrations of ATs and their effects on BA function were measured (4.1). Second, effects of inosine on AT and whole body metabolism were examined (4.2). Third, inosine transport of BA *via* ENT1 was tested (4.3). Fourth, the role of ENT1 in AT and whole body metabolism was investigated (4.4). Lastly, AdoRA2B was evaluated as a potential target of inosine in ATs (4.5).

4.1. Purine concentrations of thermogenic adipose tissue

4.1.1. Extracellular nucleotide and purine concentrations of murine brown adipocytes

To identify metabolites, that could function as auto- and paracrine regulators of EE in thermogenic AT a targeted approach measuring nucleosides and nucleotides in BA' supernatant was carried out. Since ATP has been shown to be released by adipocytes during physiological activation (see section 1.4.1) the focus was put on ATP-derived purinergic molecules.

Initially, mature BA were stimulated with and without 1µM norepinephrine (NE) to mimic sympathetic activation, and extracellular ATP, ADP, AMP, adenosine, inosine and hypoxanthine levels were measured (Figure 1). After 60 minutes of NE-stimulation, extracellular ATP concentrations of BA were significantly increased by 92%, in comparison to control cells (p≤0.05; ATP(control): 5.17 ± 0.49pmol/mg protein; ATP(NE): 9.93 ± 1.69pmol/mg protein). Moreover, a significant 8-fold increase in extracellular adenosine levels was detected (p≤0.05; adenosine(control): 7.45 ± 3.22pmol/mg protein; adenosine(NE): 59.32 ±15.45pmol/mg protein). In addition, BA' extracellular inosine concentrations were significantly increased by 92% after NE treatment (p≤0.05; inosine(control): 123.4 ± 14.12pmol/mg protein; inosine(NE): 236.7 ± 47.91pmol/mg protein). Furthermore, high levels of AMP (101.8 ± 19.83pmol/mg protein) and hypoxanthine (552.8 ± 49.76pmol/mg protein) were measured under control conditions, but extracellular concentrations of these metabolites were not significantly enhanced upon NE treatment (AMP(NE): 166.7 ± 49.23pmol/mg protein; hypoxanthine(NE): 636.7 ± 73.93pmol/mg protein). Similarly, ADP levels were not changed significantly after NE-stimulation (ADP(control): 7.19 ± 1.05pmol/mg protein; ADP(NE): 9.66 ± 1.54pmol/mg protein).
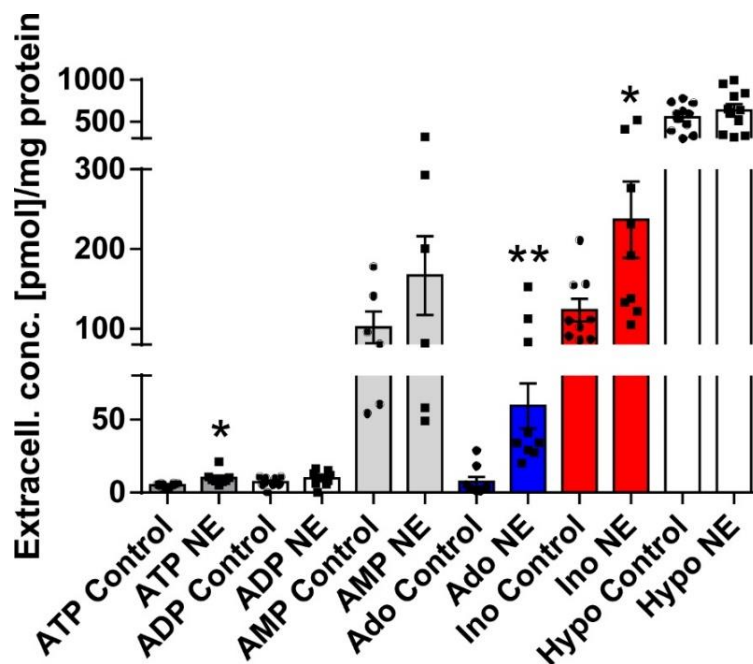
Figure 1 Extracellular nucleotide and purine concentrations of murine BA

Concentrations of ATP, ADP, AMP, adenosine (Ado), inosine (Ino) and hypoxanthine (Hypo) in the supernatant of murine BA after 60 minutes of treatment with or without 1µM NE. Data were normalized to protein content and are represented as mean ± SEM, t-test, n=6-11, *p≤0.05, **p≤0.01

These data show that a broad spectrum of purinergic molecules is present in the supernatant of murine BA under basal and stimulated conditions.

4.1.2. Effects of extracellular nucleotides and purines on murine brown adipocytes

Next, potential effects of the detected purinergic molecules on BA function were investigated. Previous experiments already showed no effects of ATP and ADP on lipolysis of BA, as measured by glycerol release (data not shown here). Moreover, different concentrations of AMP did not affect BA' lipolysis significantly (Figure 2A). NE treatment (1µM), as positive control, mediated significantly 2.3-fold elevated lipolysis levels compared to control BA (Figure 2A), proving that lipolysis of these BA cell pools can be enhanced, for instance by beta-adrenergic stimulation (Cannon and Nedergaard, 2004). To rule out false negative results due to the rapid metabolism of AMP (Gordon, 1986), the enzymes CD73 and ALP, which are responsible for AMP degradation, were inhibited using adenosine-5'-(αβ-methylene)diphosphate (αβ-methADP) and levamisole, respectively. Incubation of BA with αβ-methADP, levamisole and AMP showed no statistically significant effect on lipolysis in comparison to untreated cells (Figure 2B). Taken together, these data indicate that AMP is not an activator of BA' lipolysis.
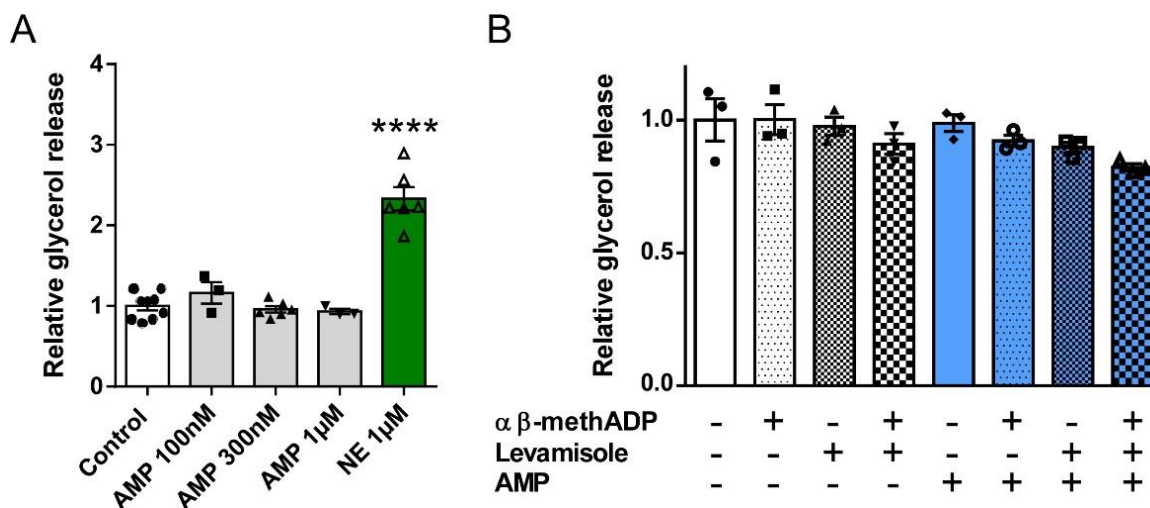
Figure 2 Effects of AMP on murine BA' lipolysis

(A) Relative glycerol release of murine BA after 120 minutes of treatment with 0, 100, 300, 1000nM AMP or 1μM NE. (B) Relative glycerol release of murine BA after 120 minutes with or without 300nM AMP treatment in absence or presence of 100μM adenosine-5'-(αβ-methylene) diphosphate (αβ-methADP) and/or 1mM levamisole (5 minutes pre-incubation). Data were normalized to protein content and are represented as mean ± SEM, ANOVA, n=3-9, ****p<0.001

In contrast, a significant 1.99 ± 0.21-fold increase (p≤0.01) in BA' lipolysis after 300nM adenosine treatment was measured (Figure 3A). Interestingly, also inosine, the direct and more stable metabolite of adenosine, induced a significant 1.89 ± 0.25-fold increase (p≤0.01) in lipolysis of BA (Figure 3A). Treatment of BA with hypoxanthine did not affect glycerol release as compared to control cells (Figure 3A). An activating effect of inosine on BA lipolysis has been recently reported (Scheibler, 2017), however the effect of inosine on adipocytes' thermogenic program, *in vivo* effects and signaling mechanisms of this purine are not described yet and still to be elucidated.

To further validate the effect of inosine on BA, intracellular cAMP was measured, which is a major second messenger in adipocytes and the master regulator of lipolysis and EE *via* PKA (Cannon and Nedergaard, 2004). Similar results as for lipolysis measurements were obtained: 300nM inosine and 300nM adenosine treatment resulted in significantly increased (+70% and +94%, respectively) intracellular cAMP levels of BA compared to control cells, whereas 300nM hypoxanthine did not increase cAMP concentrations (Figure 3B). Treatment with NE (1μM) was applied as a positive control leading to a significant increase (p≤0.001) in lipolysis and intracellular cAMP levels of BA (Figure 3A, B).

A

B
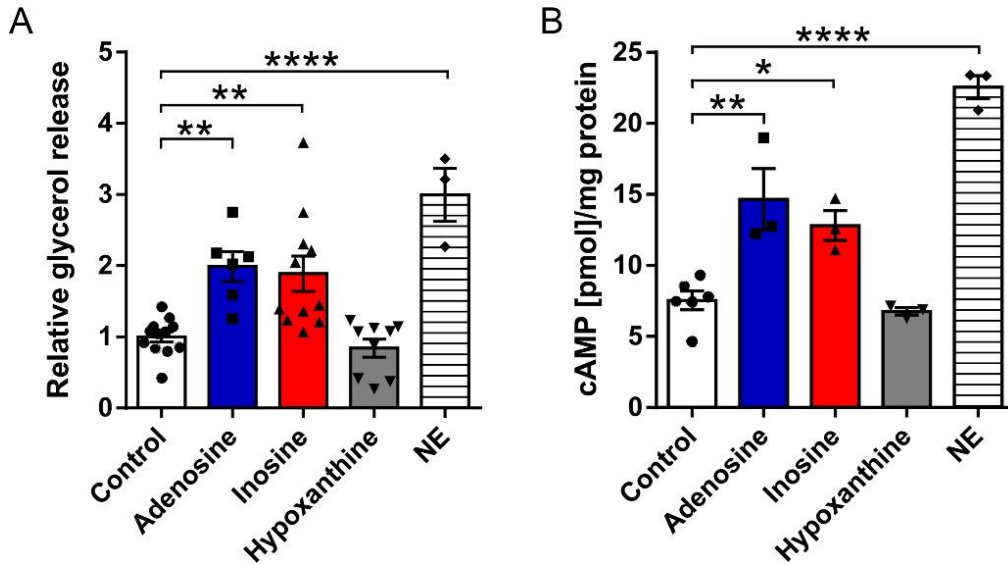
Figure 3 Effects of purines on murine BA' lipolysis and intracellular cAMP concentrations
(A) Relative glycerol release of murine BA after incubation for 120 minutes, with PBS (solvent control), 300nM adenosine, inosine, hypoxanthine or 1µM NE. (B) Intracellular cAMP-concentrations of murine BA after treatment for 15 minutes respectively, with PBS (solvent control), 300nM adenosine, inosine, hypoxanthine or 1µM NE. Data were normalized to protein content and are represented as mean ± SEM. ANOVA, n=3-12, *p≤0.05, **p≤0.01, ****p≤0.001

To assess the potency and maximum effect of inosine treatment of BA, a dose-response analysis of intracellular cAMP levels was performed and compared to adenosine and hypoxanthine dose-response curves. Inosine and adenosine treatment of BA resulted in a similar 2.4-fold maximal increase (p≤0.01) in intracellular cAMP concentrations, whereas hypoxanthine did not significantly affect maximal cAMP levels (Figure 4A). Moreover, the dose-response curves for inosine and adenosine showed stimulatory effects on intracellular cAMP levels of BA with EC_{50}-values of 173nM and 78nM, respectively (Figure 4B, C). Maximum effects were mediated by 300nM adenosine and 1000nM inosine treatments. Lastly, the dose-response curve of hypoxanthine exhibited no stimulatory effect on BA' cAMP levels and even resulted in reduced cAMP production at higher concentrations (Figure 4D).
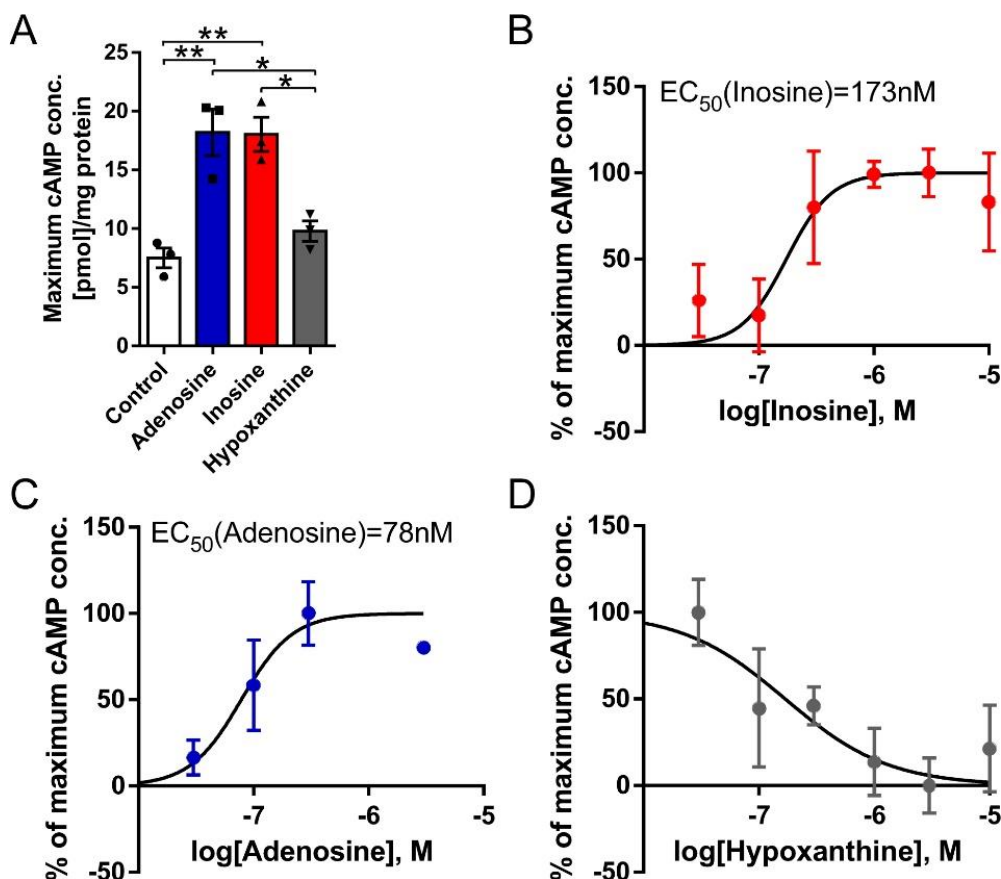
Figure 4 Effects of purines on intracellular cAMP concentrations of murine BA – dose-response curves

(A) Maximum intracellular cAMP concentrations of murine BA after treatment with 0, 30, 100, 300, 1000, 3000 and 10000nM adenosine, inosine and hypoxanthine, respectively. Dose-response curves for inosine (B), adenosine (C) and hypoxanthine (D) normalized to the maximum effect (maximum intracellular cAMP concentration, shown in A). Dose-response curves were generated by nonlinear regression with a variable slope. EC_{50}-values are calculated from the best-fit of nonlinear regression analysis. Data were normalized to protein content and are represented as mean ± SEM, A: ANOVA, n=3. *p≤0.05, **p≤0.01

In summary, stimulatory effects of inosine on intracellular cAMP levels and lipolysis of BA were observed. Adenosine treatment also led to increased BA' lipolysis and intracellular cAMP levels, while hypoxanthine did not mediate these effects.

4.1.3. Inosine plasma concentrations and extracellular purine concentrations in thermogenic adipose tissue

The following experiments focused on inosine plasma levels and extracellular inosine concentrations of thermogenic ATs after sympathetic stimulation. Since cold exposure leads to maximal activity of thermogenic fat (Cannon and Nedergaard, 2004), inosine plasma concentrations of mice housed at 4°C were measured. Interestingly, murine inosine plasma concentrations were significantly increased (2.96 ± 0.35-fold; p≤0.01) after seven days of cold exposure (4°C) compared to littermates housed at 23°C (Figure 5).
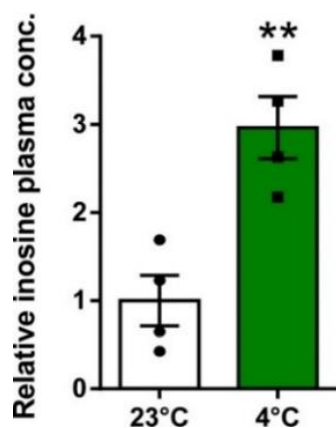
Figure 5 Inosine plasma concentrations of mice housed at 23°C and 4°C

Relative inosine plasma concentrations of 8-week-old, male C57Bl/6J mice, which were housed at 23°C or 4°C for 7 days *prior* blood draw. Data are represented as mean ± SEM, t-test, n=4, **p≤0.01

In order to study whether inosine is released in an auto- or paracrine manner from thermogenic active brown and beige AT, microdialysis experiments were performed. The microdialysis membranes were placed (*ex vivo*) in BAT and WATi of mice, which were either housed at 23°C or 4°C for seven days, and purine concentrations of the AT-dialysates were analyzed by UPLC-TUV. To mimic acute sympathetic activation ATs of mice housed at 23°C were perfused with NE (10mM).

In BAT of mice kept at 23°C basal inosine concentrations of 1982 ± 483.3nM were measured (Figure 6A). Acute stimulation of BAT with NE resulted in increased inosine levels of 5358 ± 712.5nM (+170%) (Figure 6A). Moreover, BAT dialysates of mice, which were housed at 4°C for seven days, revealed 3-fold elevated inosine levels (5978 ± 983.9nM) (Figure 6A). Adenosine and hypoxanthine levels in BAT dialysates were also measured. Strikingly, among the three purines analyzed, inosine concentrations exhibited the highest increase after direct NE-stimulation of BAT and after cold exposure (2.70 ± 0.36-fold and 3.02 ± 0.50-fold, respectively) (Figure 6B, C).
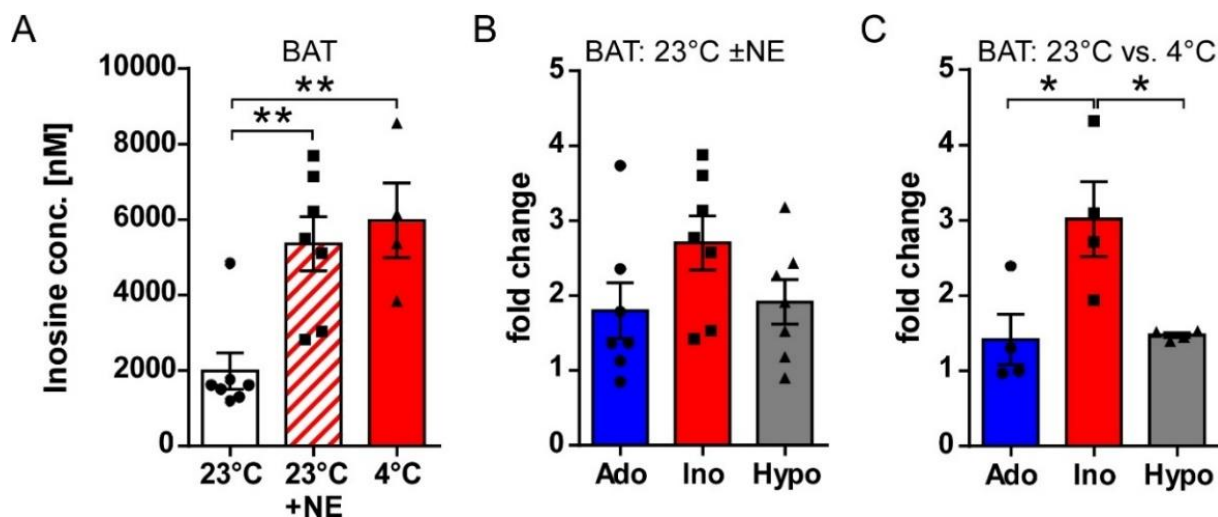
Figure 6 Extracellular inosine, adenosine and hypoxanthine concentrations of BAT

Microdialysis membranes were implanted in BAT of 8-week-old, male C57Bl/6J mice (*ex vivo*). BAT was perfused with perfusion buffer followed by 10mM NE solution and the purine concentrations of the dialysates were measured before and after 30 minutes of perfusion with NE. (A) Dialysate inosine concentrations of BAT from mice, which were either kept at 23°C or 4°C for 7 days. (B) Fold changes of adenosine (Ado), inosine (Ino) and hypoxanthine (Hypo) concentrations in dialysates of BAT from mice housed at 23°C, before and after NE stimulation. (C) Fold changes of adenosine (Ado), inosine (Ino) and hypoxanthine (Hypo) concentrations in dialysates of BAT from mice housed at 4°C or 23°C for 7 days. Results are represented as mean ± SEM, ANOVA, 7 mice kept at 23°C and 4 mice kept at 4°C were analyzed. *p≤0.05, **p≤0.01

Furthermore, inosine was studied in beige fat. In order to study browning/beiging effects, mice were either housed at 4°C or 23°C for seven days. Subsequently, WATi, the WAT depot with the highest capacity for browning (Cohen et al., 2014), was analyzed. Basal inosine levels in WATi at 23°C (47.26 ± 24.98nM) were significantly lower (p≤0.05) in comparison to the basal levels measured in BAT (1982nM ±483.3nM) (Figure 7A, 6A). This finding was in line with higher inosine concentrations in BA compared to WA observed by Scheibler (2017). Induction of browning by chronic cold exposure resulted in an 125%-increase in extracellular inosine to 106.7 ± 14.33nM (Figure 7A). Acute NE stimulation of WATi led to significantly elevated inosine levels (5.13 ± 0.98-fold; p≤0.01) reaching extracellular concentrations of 242.6 ± 46.14nM (Figure 7A, B). Moreover, comparison of fold-changes of purine concentrations after acute and chronic activation revealed that adenosine concentrations were the highest upregulated after stimulation by NE and chronic cold exposure of WATi (17.82 ± 5.23-fold and 3.82 ± 0.88-fold, respectively) (Figure 7B, C).
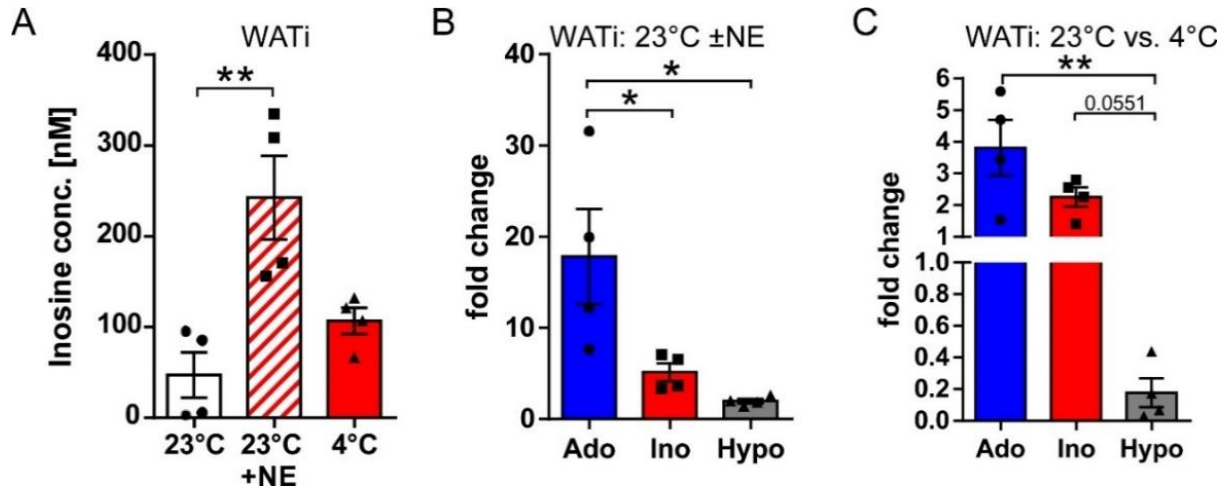
Figure 7 Extracellular inosine, adenosine and hypoxanthine concentrations of WATi
Microdialysis membranes were implanted in WATi of 8-week-old, male C57Bl/6J mice (*ex vivo*). WATi was perfused with perfusion buffer followed by 10mM NE solution and the purine concentrations of the dialysates were measured before and after 30 minutes of perfusion with NE. (A) Dialysate inosine concentrations of WATi from mice, which were either kept at 23°C or 4°C for 7 days. (B) Fold changes of adenosine (Ado), inosine (Ino) and hypoxanthine (Hypo) concentrations in dialysates of WATi from mice housed at 23°C, before and after NE stimulation. (C) Fold changes of adenosine (Ado), inosine (Ino) and hypoxanthine (Hypo) concentrations in dialysates of WATi from mice housed at 4°C or 23°C for 7 days. Results are represented as mean ± SEM, ANOVA, n=4, *p≤0.05, **p≤0.01

In order to examine the transferability of this findings in murine tissues to humans, human brown adipocytes (hBA) were treated with or without NE (1µM) and extracellular purine concentrations were measured. In the cell culture medium of untreated hBA adenosine, inosine and hypoxanthine concentrations of 80.86 ± 7.71pmol/mg protein, 1846 ± 496.1pmol/mg protein and 1301 ± 274.0pmol/mg protein, respectively, were detected (Figure 8). NE-stimulation resulted in elevated extracellular purine concentrations of adenosine (105.8 ± 23.37pmol/mg protein; +31%), inosine (2878 ± 797.8pmol/mg protein; +56%) and hypoxanthine (2041 ± 411.7pmol/mg protein; +57%) (Figure 8). However, the observed increases in extracellular purine concentrations after treatment with NE were not statistically significant. Strikingly, extracellular basal inosine concentrations of hBA were significantly higher (p≤0.005) compared to the measured extracellular inosine levels of murine BA (123.4 ± 14.12pmol/mg protein; Figure 1). In addition, inosine was detected as the most abundant purine in hBA under basal and NE-stimulated conditions (Figure 8).
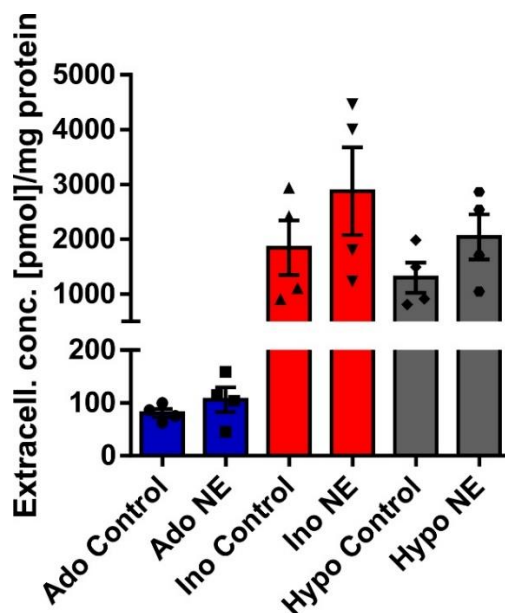
Figure 8 Extracellular purine concentrations of human BA

Concentrations of adenosine (Ado), inosine (Ino) and hypoxanthine (Hypo) in the supernatant of human BA after 60 minutes of treatment with or without 1µM NE. Data were normalized to protein content and are represented as mean ± SEM, t-test, n=4

In summary, purines were detected in the dialysates of BAT and WATi under basal and stimulated conditions, with WATi showing significantly lower inosine levels compared to BAT. Interestingly, after NE-stimulation and after cold exposure, extracellular inosine concentrations were the most highly upregulated among the detected purines in BAT. Sympathetic stimulation led to elevated extracellular inosine concentrations of BAT and WATi indicating a general role of inosine in thermogenic brown and beige AT.

4.2. Effects of inosine on adipose tissue and whole body metabolism

4.2.1. Effects of inosine on brown and white adipose tissue function

Since inosine was shown to activate BA *in vitro* (Figure 3, 4A, 4B), the effects of this purine on thermogenic fat were subsequently tested *ex* and *in vivo*.

Firstly, analysis of lipolysis, an important hallmark of BA activation, revealed that inosine stimulation significantly increased lipolysis in BAT (+26%; p≤0.005) and WATi (+54%; p≤0.05) explants (Figure 9).
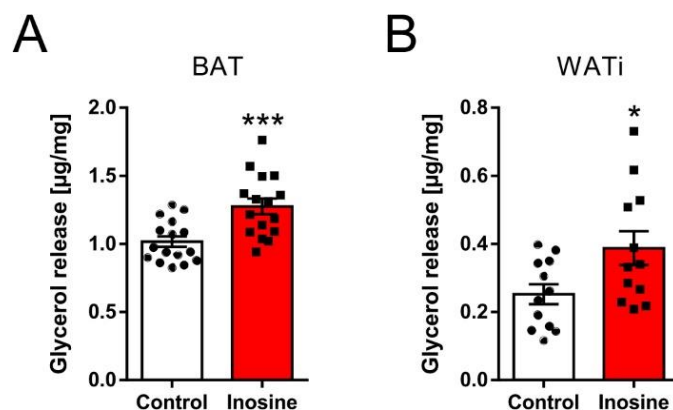
Figure 9 Effects of inosine on *ex vivo* lipolysis of BAT and WATi
Glycerol release of (A) BAT and (B) WATi explants of 8-week-old, male C57Bl/6J mice after 120 minutes of incubation with or without 300nM inosine. Values were normalized to tissue weights. Results are represented as mean ± SEM. t-test, n=12, *p≤0.05, ***p≤0.005

Secondly, effects of inosine on oxygen consumption of BAT and WATi explants were measured. Pre-incubation with 300nM inosine for 15 minutes resulted in a significant increase in basal oxygen consumption of BAT and WATi (2.2-fold and 1.8-fold, respectively; p≤0.05) (Figure 10A, B). In addition, UCP1-mediated mitochondrial respiration was significantly elevated (1.8-fold; p≤0.05) in inosine-treated BAT samples (Figure 10C). UCP1-mediated oxygen consumption of WATi was 1.8-fold increased after inosine stimulation, but the difference compared to control tissues was not statistically significant (Figure 10D).
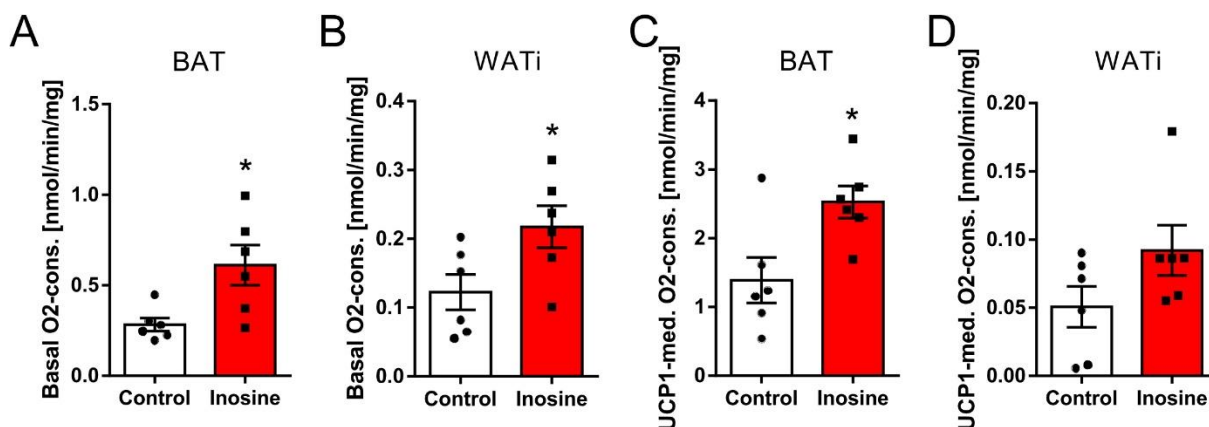
Figure 10 Effects of inosine on oxygen consumption of BAT and WATi
Basal oxygen consumption of (A) BAT and (B) WATi of 8-week-old, male C57Bl/6J mice measured by Oxygraph O2k apparatus after 15 minutes of pre-incubation with or without 300nM inosine. Respective UCP1-mediated oxygen-consumption of (C) BAT and (D) WATi. UCP1-mediated oxygen consumption was calculated as the difference of oxygen concentrations after substrates administration (octanoylcarnitine, pyruvate, malate, glutamate and succinate) and GDP injection. Data were normalized to tissue weights and are represented as mean ± SEM. t-test, n=6, *p≤0.05

Taken together, stimulation with inosine resulted in promoted thermogenic function of BAT and WATi *ex vivo*.

4.2.2. Effects of inosine administration on oxygen consumption *in vivo*

Next, to study the role of inosine in metabolism *in vivo*, the effect of inosine on whole body EE was measured using metabolic cages (TSE Phenomaster). An oral gavage of either NaCl 0.9%

(vehicle) or 100µg/kg inosine was administered to 8-week-old, male C57Bl6/J mice. Subsequently, oxygen consumption at 23°C was monitored for 2 hours. Administration of inosine resulted in a significant increase in oxygen consumption (AUC: +23%; p≤0.05) (Figure 11), which indicates elevated EE of metabolically active organs such as BAT.
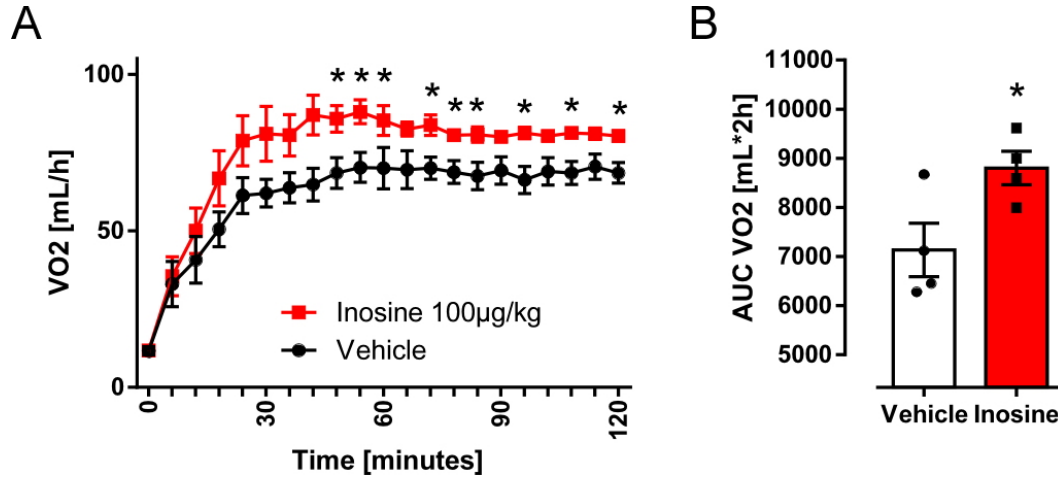
Figure 11 Acute effects of inosine on oxygen consumption *in vivo*
(A) Oxygen consumption (VO_2), after oral gavage of either NaCl 0.9% (vehicle) or 100µg/kg inosine (dissolved in NaCl 0.9%), of 8-week-old, male C57Bl6/J mice at 23°C. (B) Respective AUCs of measured V(O_2) over 2 hours. Data are represented as mean ± SEM. t-test, n=4. *p≤0.05

This acute effect of inosine on whole body EE gave rise to the question whether chronic inosine treatment also has beneficial effects on BAT function and browning of WATi. In order to investigate chronic effects *in vivo*, micro-osmotic pumps were implanted in 8-week-old, male C57Bl6/J mice to steadily apply inosine (0.11µl/h of 3.4mM solution; 2.4µg/day) or vehicle (NaCl 0.9%) for 28 days.

During the fourth week after implantation of the pumps, indirect calorimetry was measured. ANCOVA of mice housed at 23°C, showed a tendency for inosine-treated mice to consume more oxygen (p=0.0889) (Figure 12A). The AUC of V(O_2) over 24 hours at 23°C was 6% higher after inosine treatment compared to the vehicle-treated control group, but this difference was not statistically significant (Figure 12B, C). Motility and food intake were not different between the two treatment groups (Figure 12D, E). In contrast, oxygen consumption of the inosine treated mice was significantly enhanced by 11% (p≤0.01) during acute cold exposure at 4°C (Figure 12F) indicating an increased thermogenic potential of these mice after chronic inosine treatment.
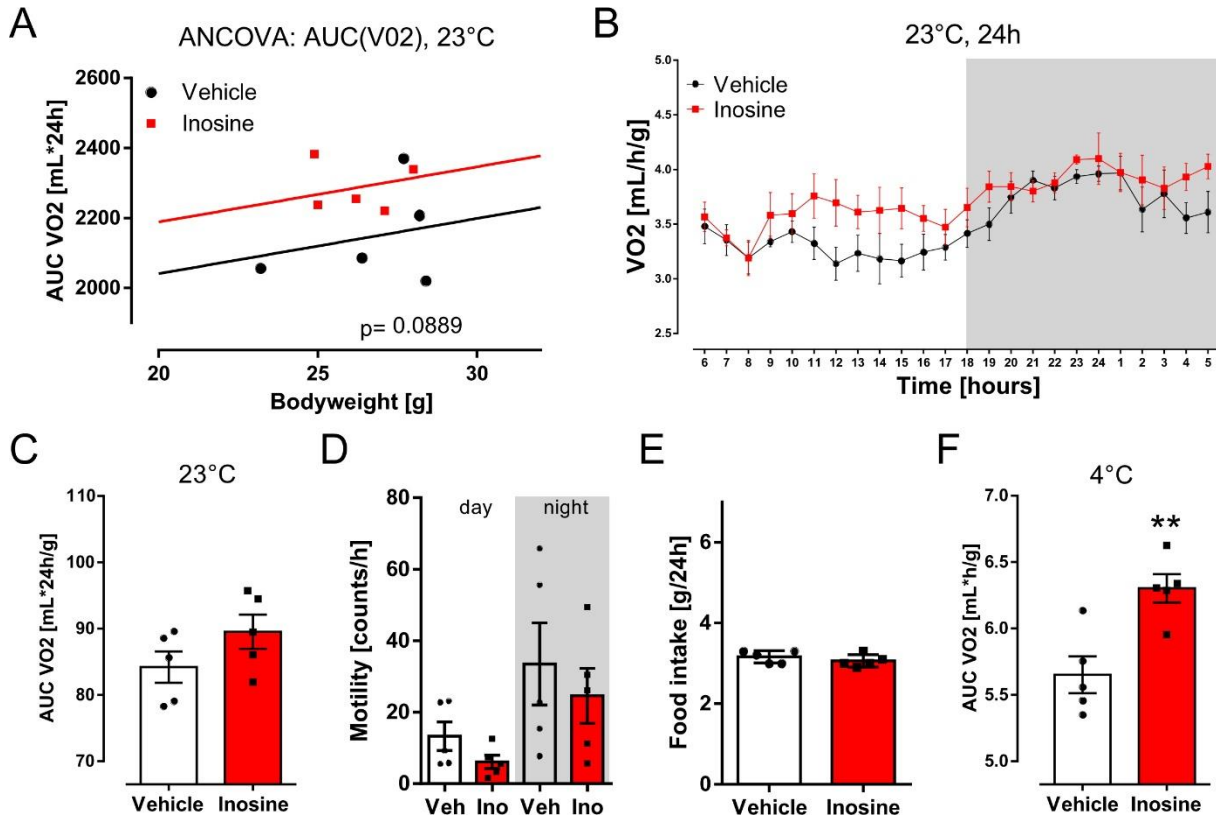
Figure 12 Chronic effects of inosine *in vivo*
C57Bl6/J mice were housed at 23°C and fed a control diet, inosine or vehicle treatment (0.11µl/h of 3.4mM solution; 2.4µg/day) was continuously administered by micro-osmotic pumps for 28 days. (A) ANCOVA (AUC(VO2) vs. bodyweight). (B) Oxygen-consumption, (C) AUC of oxygen-consumption, (D) motility and (E) food intake after 28 days of treatment. (F) AUC of oxygen consumption over 1 hour during acute cold-exposure at 4°C after 28 days of treatment. Results are represented as mean ± SEM. t-test was applied except for A (ANCOVA), n=5. **$p \leq 0.01$

In order to further investigate the molecular mechanisms underlying the improved thermogenic function, expression of thermogenic genes in ATs was analyzed. qRT-PCR analysis revealed significantly enhanced expression levels by 126% ($p \leq 0.05$) of the thermogenic marker *Ucp1* in BAT of mice, which received inosine for 28 days as compared to vehicle-treated control mice (Figure 13A). *Ucp1* mRNA-expression in inguinal and gonadal WAT depots was increased, by 43% and 81%, respectively, albeit this increase was not statistically significant (Figure 13B, C). In contrast, the browning marker gene *Prdm16* was significantly higher (+104%; $p \leq 0.05$) expressed in WATi of inosine-treated mice, while this effect was not observed in the gonadal fat depots (Figure 13D, E). Moreover, immunohistochemical staining of UCP1 showed increased amounts of UCP1-protein and multilocular adipocytes in WATi of inosine-treated mice (Figure 13F). Quantification of cell areas revealed a significantly smaller ($p \leq 0.05$) adipocytes size in WATi of mice, which received inosine (110.6 ± 12.30µm^2) compared to the vehicle-group (187.4 ± 39.81µm^2), indicating a browning effect of inosine on WATi (Figure 13G).
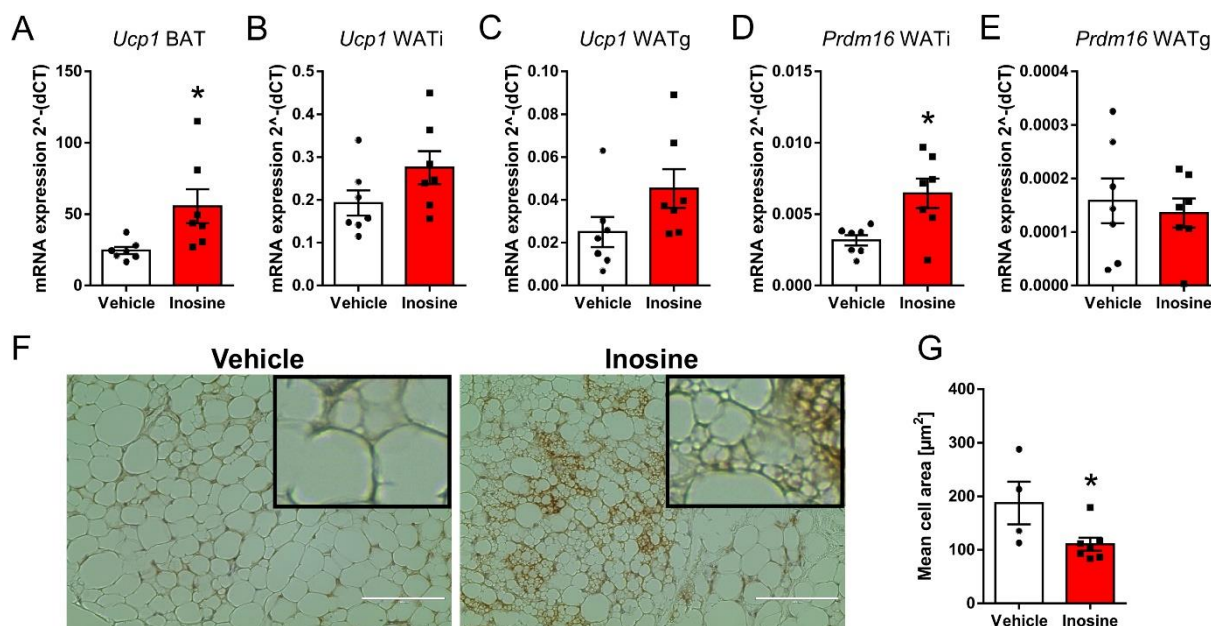
Figure 13 Effects of chronic inosine administration on thermogenic gene expression in murine ATs

C57Bl6/J mice were housed at 23°C and inosine or vehicle treatment (0.11µl/h of 3.4mM solution; 2.4µg/day) was continuously administered by micro-osmotic pumps for 28 days. mRNA expression of the thermogenic markers *Ucp1* in (A) BAT, (B) WATi and (C) WATg; and *Prdm16* in (D) WATi and (E) WATg. (F) Representative UCP1 stainings of WATi (the scale bar corresponds to 100µm; upper right corner: 4-fold magnification) and (G) mean area of inguinal WA after 28 days of constant inosine or vehicle treatment administered by micro-osmotic pumps. Expression data were normalized to *Hprt* and are represented as mean ± SEM. t-test, n=7, except for (G): n=4-7. *p≤0.05

4.2.3. Effects of inosine treatment and concomitant high fat diet

The observed stimulatory effect of inosine on whole body EE led to the question whether chronic inosine treatment might have beneficial effects during diet-induced obesity (DIO). To investigate this hypothesis, micro-osmotic pumps were implanted (using similar concentrations and mice as described in 4.2.2) and mice were subsequently fed a high fat diet (HFD) for the application period of 28 days.

Mice treated with inosine gained significantly less weight (-0.98 ± 0.43g; p≤0.05), in comparison to the vehicle-treated controls, after four weeks of HFD (Figure 14A). In addition, ANCOVA of oxygen consumption after four weeks of HFD showed that the inosine-treated mice consumed significantly (p=0.0398) more oxygen at 23°C in comparison to vehicle-treated littermates (Figure 14B). The oxygen consumption rate of mice after HFD and constant inosine administration was increased (Figure 14C, D), while motility and food intake were not statistically different between the two groups (Figure 14E, F). Assessment of the maximal thermogenic potential of brown/beige fat *in vivo*, by acute cold exposure at 4°C, demonstrated significantly elevated oxygen consumption (+1.06 ± 0.43ml*h/g; +20%; p≤0.05) of mice after chronic inosine treatment during HFD in comparison to the vehicle group (Figure 14G). In summary, after 28 days of HFD and constant inosine application, reduced weigh gain and improved oxygen consumption of the inosine-treated mice were measured.
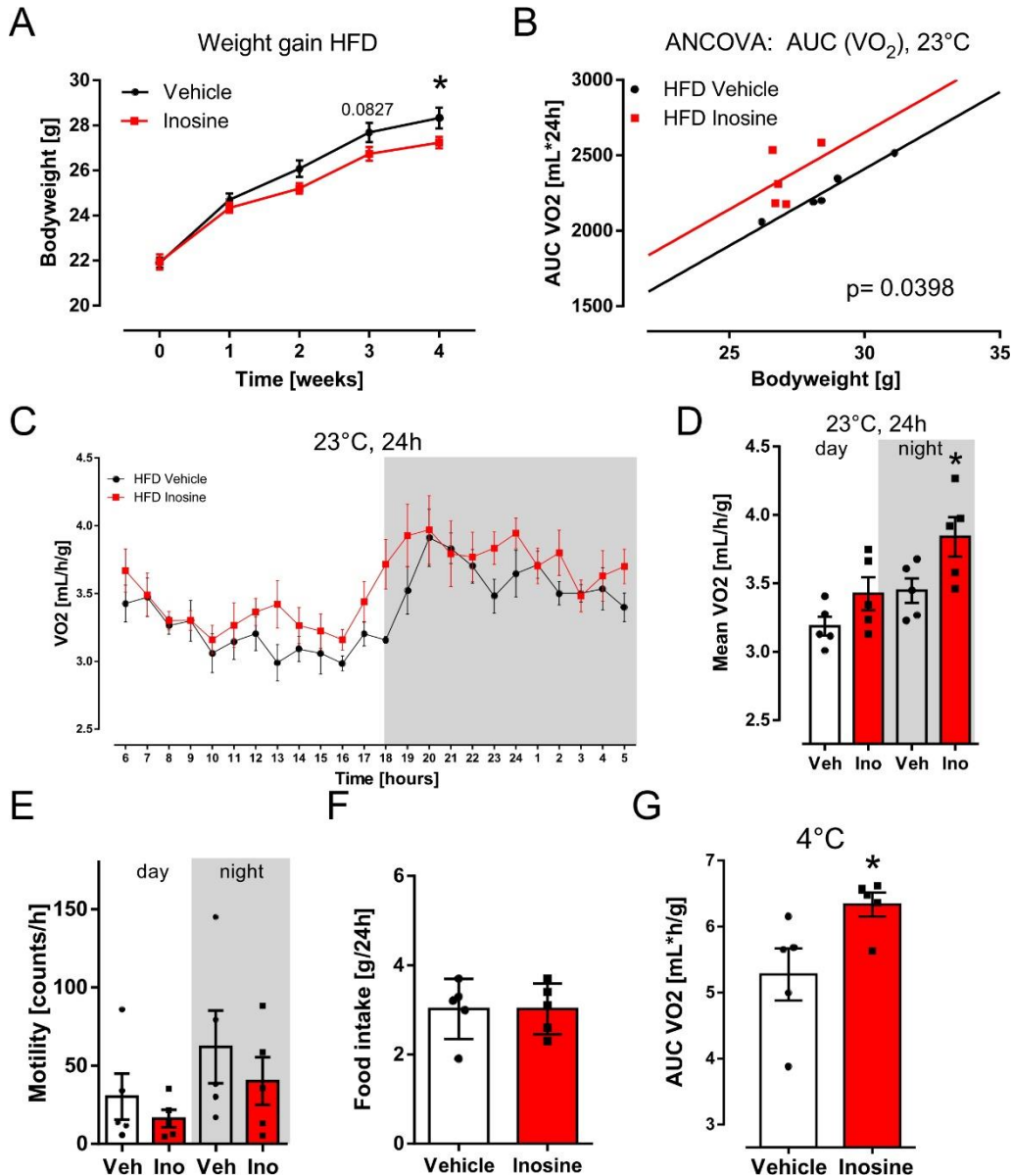
Figure 14 Effects of chronic inosine administration during HFD
C57Bl6/J mice were housed at 23°C and fed a high fat diet (60% of kcal derived by fat), inosine or vehicle treatment (0.11µl/h of 3.4mM solution; 2.4µg/day) was continuously administered by micro-osmotic pumps for 28 days. (A) Weight gain. (B) ANCOVA (AUC(VO$_2$) vs. bodyweight), (C) oxygen-consumption at 23°C and (D) mean of oxygen consumption at 23°C during day and night cycle (12 hours each), (E) motility, (F) food-intake, (G) AUC of oxygen consumption over 1 hour during acute cold-exposure at 4°C after 28 days of HFD with or without chronic inosine treatment. Results are represented as mean ± SEM. t-test was applied except for B (ANCOVA), n=5, except for A: n=10, *p≤0.05

DIO induces whitening of BAT, which is characterized by adipocyte hypertrophy, inflammation and mitochondrial dysfunction (Kusminski and Scherer, 2012; Kotzbeck et al., 2018). To investigate whether inosine administration mitigates DIO effects, expression of mitochondrial and thermogenic genes in ATs was measured. Analysis of qRT-PCR data revealed that mRNA expression levels of mitochondrial genes, such as *Ndufa1*, *Nd5* and the thermogenic marker gene *Ucp1*, were significantly increased in BAT of inosine-treated mice (+40%, +39% and +46%, respectively; p≤0.05) after 28 days of HFD compared to vehicle-treated control animals (Figure 15A-C). Moreover, also in inguinal WAT depots of the inosine treatment group elevated

expression of thermogenic genes, including *Ucp1*, *Ppargc1a* and *Prdm16* (+726%, +48% and +67%, respectively; p≤0.05), was measured (Figure 15D-F). These data indicate enhanced mitochondrial biogenesis and browning of BAT and WATi after inosine administration. In contrast, no significant differences in thermogenic marker gene expression between vehicle- and inosine-treated mice were observed in the WATg samples (Figure 15G-I).
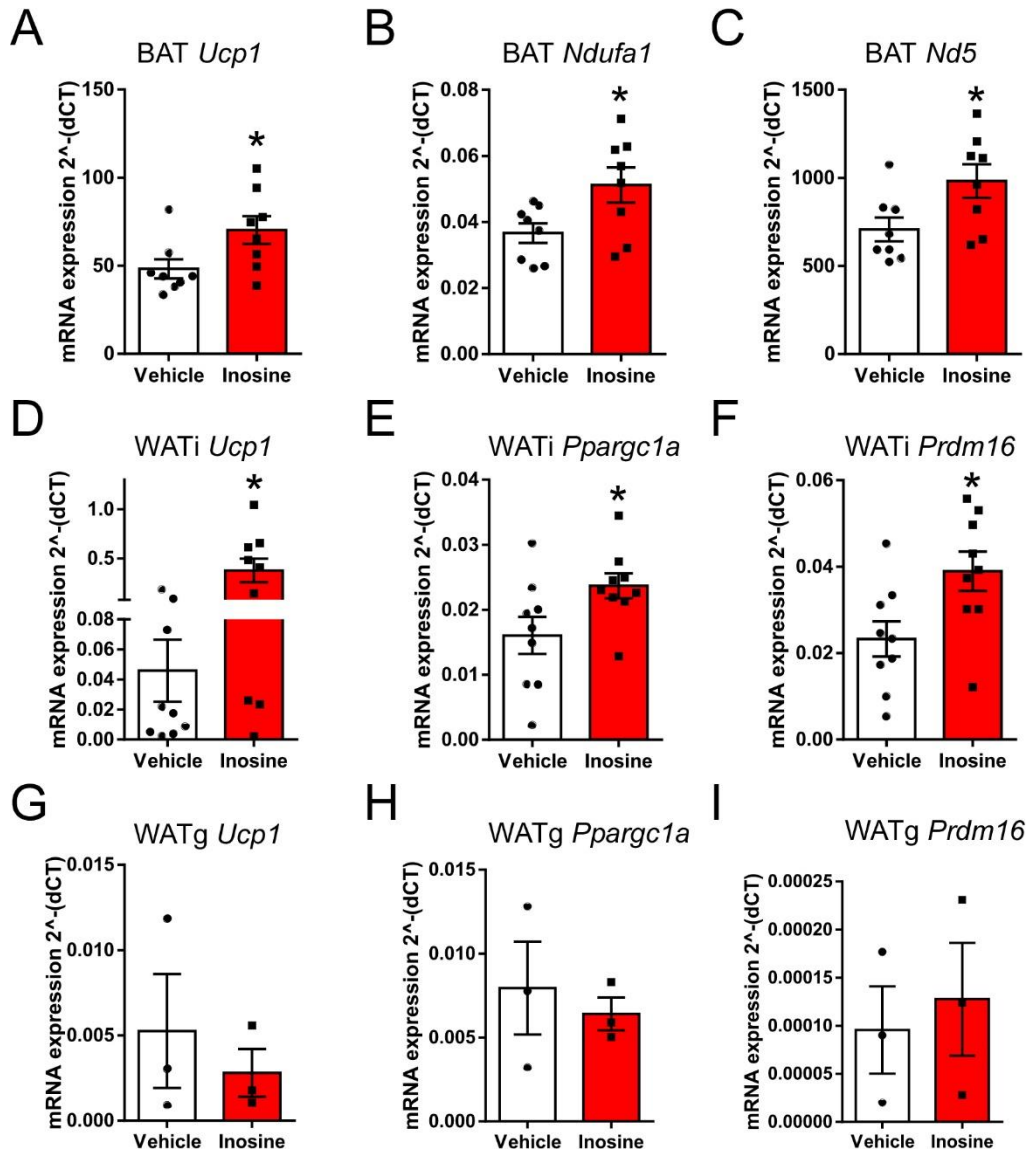
Figure 15 Effects of constant inosine administration during HFD on mRNA expression of thermogenic and mitochondrial genes
C57Bl6/J mice were housed at 23°C and fed a high fat diet (60% of kcal derived by fat), inosine or vehicle treatment (0.11µl/h of 3.4mM solution; 2.4µg/day) was continuously administered by micro-osmotic pumps for 28 days. mRNA expression of the thermogenic gene (A) *Ucp1* and the mitochondrial genes (B) *Ndufa1* and (C) *Nd5* in BAT. mRNA expression of the thermogenic genes (D) *Ucp1*, (E) *Ppargc1a* and (F) *Prdm16* in WATi. mRNA expression of the thermogenic genes (G) *Ucp1*, (H) *Ppargc1a* and (I) *Prdm16* in WATg. Values were normalized to *Hprt* and are represented as mean ± SEM. t-test; A-C: n=8, D-F: n=9, G-I: n=3. *p≤0.05

After 28 days of HFD, dissected BAT depots of mice, which received inosine, looked more brownish in comparison to control tissues (Figure 16A). Histological stainings of BAT revealed more multilocular cells in the inosine-treated animals and a tendency (p=0.0834) for smaller adipocyte size of BAT after HFD and concomitant inosine treatment was observed (Vehicle:

14.10 ± 1.25µm^2; Inosine: 11.57 ± 0.53µm^2) (Figure 16B, C). Western blot analysis of BAT showed increased UCP1 protein levels for inosine-treated mice (1.87 ± 0.23; p≤0.05) compared to vehicle-treated animals, after four weeks of HFD (Figure 16D).
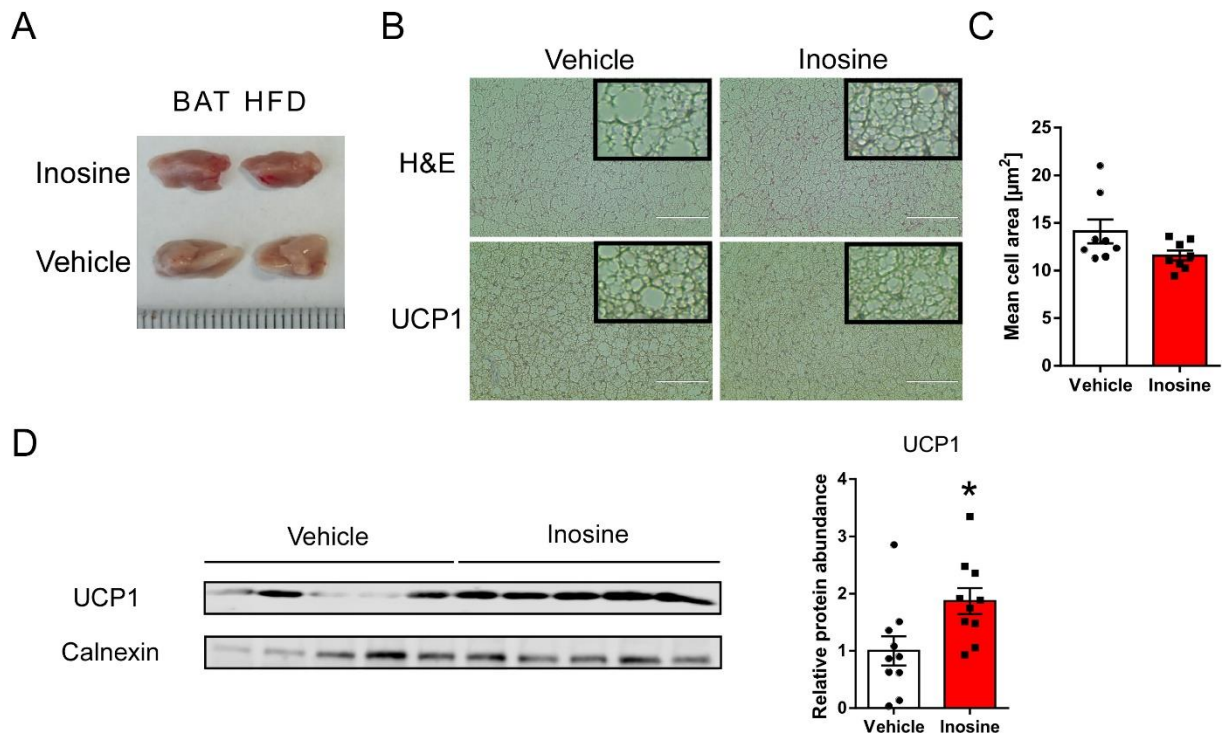
Figure 16 Effects of constant inosine administration during HFD on UCP1 protein expression and morphology of murine BAT
C57Bl6/J mice were housed at 23°C and fed a high fat diet (60% of kcal derived by fat), inosine or vehicle treatment (0.11µl/h of 3.4mM solution; 2.4µg/day) was continuously administered by micro-osmotic pumps for 28 days. (A) Representative macroscopic picture, (B) representative H&E and UCP1 stainings (the scale bar corresponds to 100µm; upper right corner: 4-fold magnification), (C) quantification of cell area and (D) representative Western-Blot and quantification of UCP1 of BAT after 28 days of HFD. Expression data of Western-Blots were normalized to Calnexin. Results are represented as mean ± SEM. t-test, C: n=8, D: n=10. *p≤0.05

In addition, histological analysis also revealed enhanced expression of UCP1 protein and an increased number of multilocular beige cells in WATi of inosine-treated mice (Figure 17A). The size of inguinal and gonadal white adipocytes after HFD was significantly decreased in the inosine treatment group (122.6 ± 15.40µm^2 and 492.3 ± 112.7µm^2, respectively) as compared to the control group (438.4 ± 76.66µm^2 and 826.9 ± 107.7µm^2, respectively) (Figure 17).
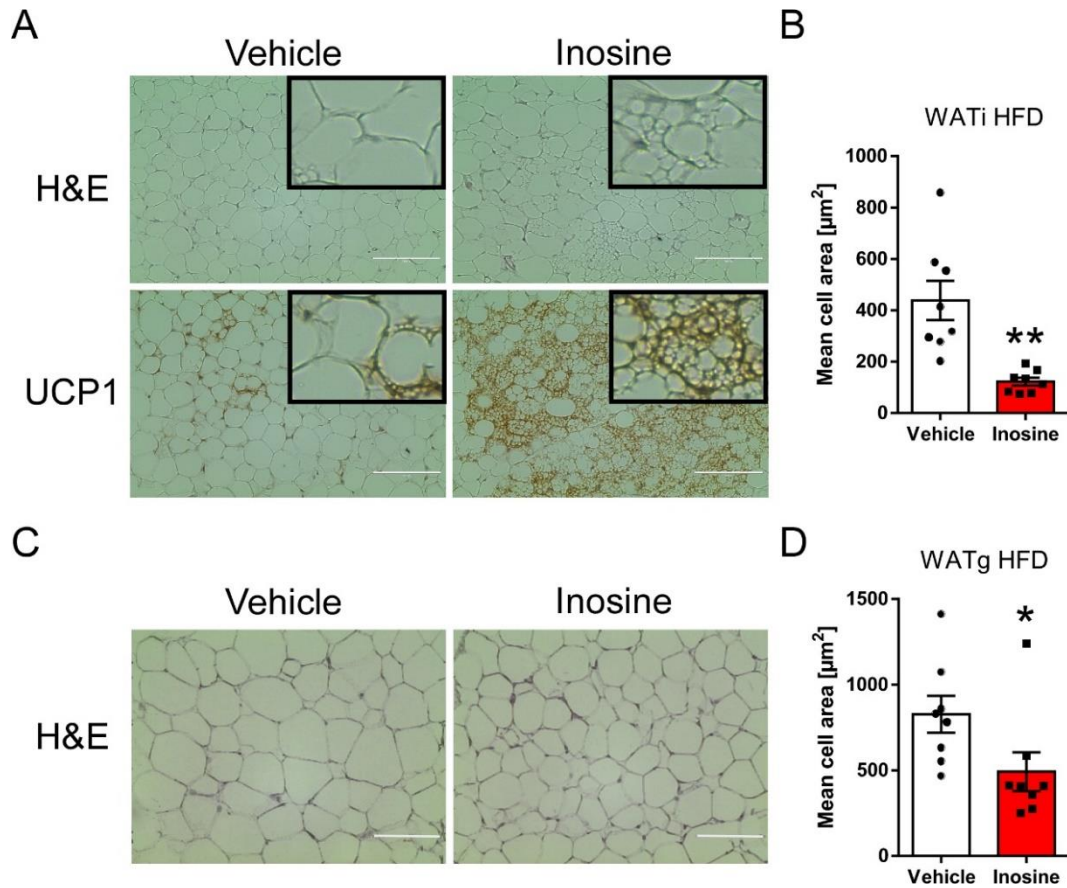
Figure 17 Effects of constant inosine administration during HFD on UCP1 protein expression and adipocyte-morphology of murine WAT
C57Bl6/J mice were housed at 23°C and fed a high fat diet (60% of kcal derived by fat), inosine or vehicle treatment (0.11µl/h of 3.4mM solution; 2.4µg/day) was continuously administered by micro-osmotic pumps for 28 days. (A) Representative H&E and UCP1 staining of WATi sections and (B) quantification of cell area. (C) Representative H&E staining of WATg sections and (D) quantification of cell area. The scale bars correspond to 100µm; upper right corner in (A): 4-fold magnification. Results are represented as mean ± SEM. t-test, n=8, *p≤0.05, **p≤0.01

Taken together, these data indicate that inosine stimulation leads to increased thermogenic potential and EE of brown and beige AT, thereby alleviating DIO effects.

4.3. Inosine transport of brown adipocytes *via* ENT1

On the one hand, several degrading enzymes determine purine concentrations (Fredholm et al., 2011; Nguyen et al., 2015). On the other hand, extracellular purine concentrations are mediated by transmembrane release or uptake *via* certain transporters (Pastor-Anglada and Pérez-Torras, 2018).

Since the equilibrative nucleoside transporters 1 and 2 (ENT1 and 2, respectively) have been shown to be essential for the flux of nucleosides through membranes in various cell types including adipocytes (see section 1.4.2), the aforementioned transporters were investigated in the context of inosine transport in adipocytes.

RNA-Sequencing enabled a direct comparison of *Slc29a1* (encoding ENT1) and *Slc29a2* (encoding ENT2) expression in mature adipocytes isolated from murine BAT, WATi and WATg. Analysis revealed that *Slc29a1* was the higher expressed gene in all types of adipocytes

analyzed (Figure 18). Moreover, BA showed significantly higher levels of *Slc29a1*-mRNA (61.25 ± 2.39) than inguinal (35.00 ± 5.73; p≤0.005) and gonadal (28.00 ± 5.05; p≤0.001) WA (Figure 18).
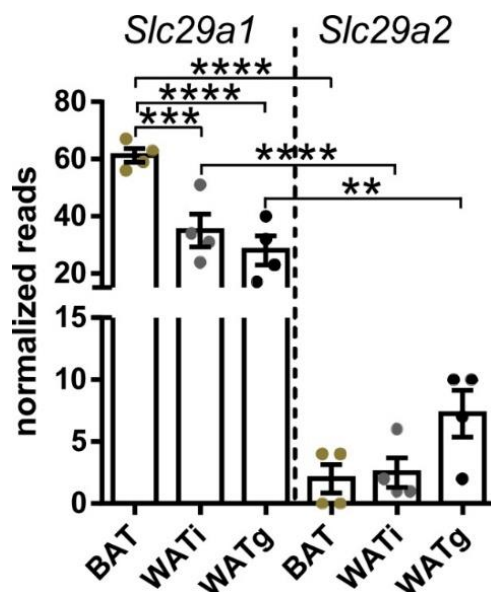
Figure 18 Expression of *Slc29a1* and *Slc29a2* in BAT-, WATi- and WATg-resident mature adipocytes
RNA-Sequencing data: mRNA expression values of *Slc29a1* and *Slc29a2* of mature adipocytes isolated from BAT, WATi and WATg depots of 20-week-old C57Bl6/J mice. Results are represented as mean ± SEM. ANOVA, n=4. **p≤0.01, ***p≤0.005, ****p≤0.001

Given the high expression of *Slc29a1* in BA, it was investigated to what extend ENT1 is involved in inosine transport of BA. Initially, BA were treated with dipyridamole. This drug is therapeutically used as an antiplatelet agent in combination with acetylsalicylic acid after stroke or transient ischemic attack and described as a potent ENT1-inhibitor (Hills and Johnston, 2008; Wang et al., 2021). Incubation of BA with 1µM dipyridamole led to 2.17 ± 0.21-fold increased (p≤0.005) extracellular inosine concentrations (Figure 19A). This result was in line with the literature reporting increased purine concentrations of adipocytes due to dipyridamole treatment (Kather, 1988; Scheibler, 2017). However, the enhanced extracellular inosine concentrations could derive from the fast enzymatic degradation of accumulating extracellular adenosine (Welihinda et al., 2016) and/or be caused by inhibition of the transmembrane transport of inosine. In order to study the direct transmembrane transport of inosine, uptake of radioactively labelled inosine in BA was measured showing significantly reduced ^{3}H-inosine uptake after pre-incubation with dipyridamole (-6.82 ± 1.47pp) compared to control cells (Figure 19B).
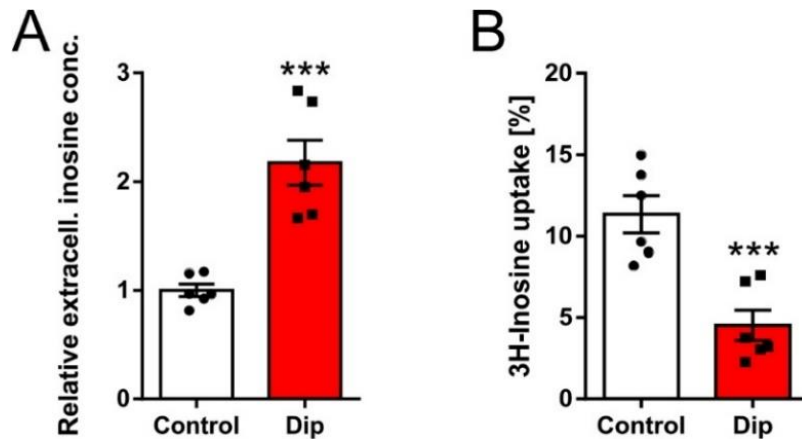
Figure 19 Effects of dipyridamole on inosine transport of murine BA

(A) Relative extracellular inosine concentrations of murine BA after 60 minutes of incubation with or without dipyridamole 1µM (Dip). (B) Uptake of ^{3}H-inosine in murine BA within 5 minutes, after pre-incubation with or without dipyridamole 1µM (Dip) for 15 minutes. Data were normalized to protein concentrations and are represented as mean ± SEM. t-test, n=6, ***p≤0.005

Within the next experiment, brown adipocytes of global ENT1-KO and WT mice were studied to compare the pharmacological approach of ENT1-inhibition with a genetic model. Dipyridamole is known to act on further targets besides ENTs (Gresele et al., 2011), therefore it was important to evaluate the ENT1-mediated effects in more detail using a genetic deletion model of ENT1. Loss of ENT1 led to significantly 5.75 ± 0.51-fold enhanced extracellular inosine concentrations compared to WT BA (Figure 20A).
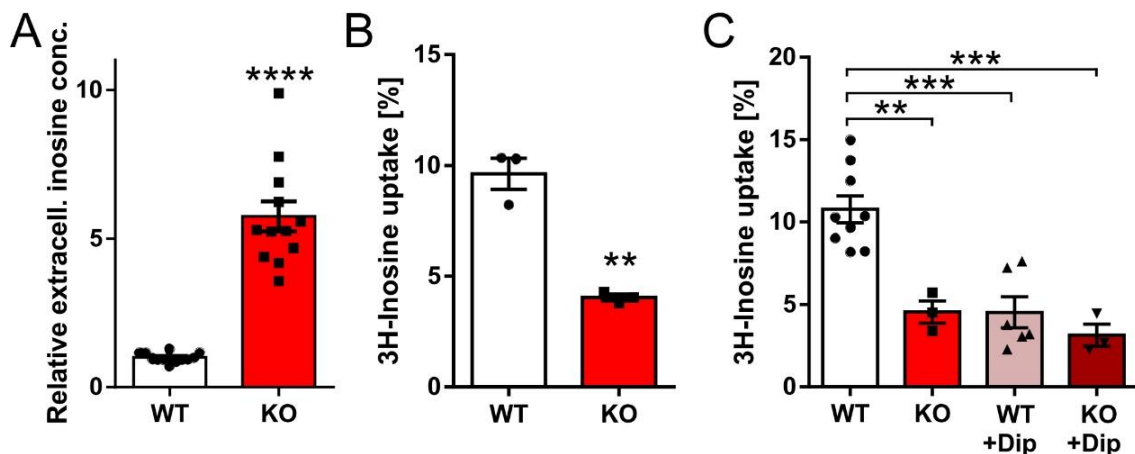
Figure 20 Effects of global ENT1-deletion on inosine uptake of murine BA

(A) Relative extracellular inosine concentrations of murine WT and ENT1-KO (KO) BA after 60 minutes. (B) Uptake of ^{3}H-inosine in murine WT and ENT1-KO BA within 5 minutes. (C) Uptake of ^{3}H-inosine in murine WT and ENT1-KO BA within 5 minutes after pre-incubation with or without dipyridamole 1µM (Dip) for 15 minutes (pooled data of Figures 22B and 23B). Data were normalized to protein concentrations and are represented as mean ± SEM. A-B: t-test, C: ANOVA, n=3-12, **p≤0.01, ***p≤0.005, ****p≤0.001

Next, radioactive labelled inosine was added to mature ENT1-KO and WT BA. During incubation for 5 minutes, ENT1-KO BA incorporated significantly less ^{3}H-labelled inosine (-5.59 ± 0.72pp; p≤0.01) from the cell culture supernatant than WT control cells (Figure 20B). Moreover, ENT1-KO and WT BA were pre-incubated with or without 1µM dipyridamole for 15 minutes, before ^{3}H-inosine was added. Measurements of ^{3}H-inosine uptake revealed that

genetic deletion of ENT1 and pharmacological inhibition of ENT1 in WT cells by dipyridamole led to a similar reduction of ^{3}H-inosine uptake in BA (Figure 20C). In addition, no significant additive effect of dipyridamole on ENT1-KO BA was observed (Figure 20C), indicating that other potential mechanisms like inhibition of ENT2 and 'off-target effects' of dipyridamole (1µM), such as phosphodiesterase 5 (PDE5) inhibition (Gresele et al., 2011), do not significantly contribute to the effects of dipyridamole in BA.

4.4. The role of ENT1 in adipose tissue metabolism

4.4.1. Effects of global deletion of ENT1 on brown and white adipocytes

Given the regulatory effects of ENT1 on extracellular inosine levels of BA, further experiments focused on the effects of ENT1-deletion on adipocyte function.

4.4.1.1. Differentiation of ENT1-KO brown and white adipocytes

Initially, pre-BA were isolated from newborn WT and global ENT1-KO mice and differentiated to mature BA. Oil Red O stainings showed that BA lacking ENT1 differentiated better, which was indicated by a higher amount of stained lipid droplets (Figure 21A).
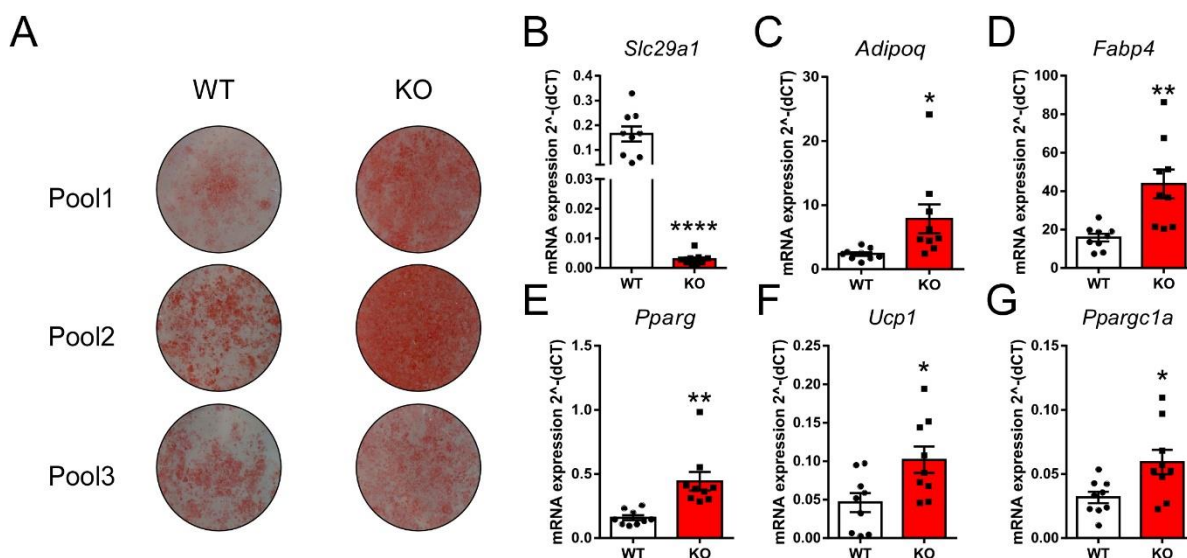
Figure 21 Differentiation of murine WT and ENT1-KO BA
(A) Representative Oil Red O stainings of murine WT and ENT1-KO (KO) BA. mRNA expression of (B) *Slc29a1*, the adipogenic marker genes (C) *Adipoq*, (D) *Fabp4* and (E) *Pparg* and the thermogenic marker genes (F) *Ucp1* and (G) *Ppargc1a* in murine WT and ENT1-KO BA. qRT-PCR values were normalized to *Hprt*. Results are represented as mean ± SEM. t-test, n=9. *p≤0.05, **p≤0.01, ****p≤0.001

As expected, qRT-PCR analysis revealed significantly decreased (p≤0.001) mRNA expression of *Slc29a1* in ENT1-KO BA (Figure 21B). Moreover, increased expression of the adipokine adiponectin (+230%; p≤0.05), a key regulator of insulin sensitivity negatively correlating with development of type 2 diabetes (Ziemke and Mantzoros, 2010), was measured in ENT1-KO BA compared to WT cells (Figure 21C). Furthermore, expression levels of the adipogenic marker genes *Fabp4* and *Pparg* were significantly enhanced in ENT1-depleted BA (+176% and +180%, respectively; p≤0.01) (Figure 21D, E). In addition, mRNA expression of *Ucp1* and

Ppargc1a was increased in ENT1-KO BA (+120% and +87%, respectively; p≤0.05) (Figure 21F, G) indicating an increased thermogenic capacity of these adipocytes.

Significantly enhanced expression of aP2 (32.97 ± 13.68), PPARγ (6.49 ± 1.36) and UCP1 (3.18 ± 0.87) in ENT1-KO BA in comparison to WT BA was also observed on protein level using Western-Blot method (Figure 22).
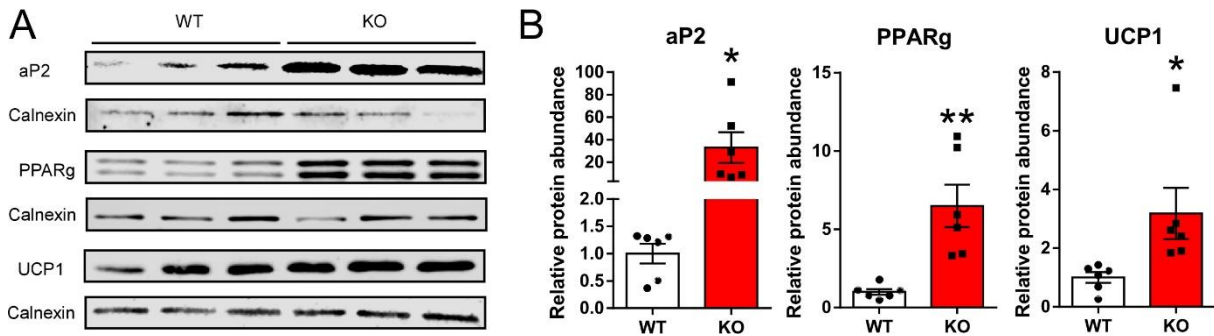
Figure 22 Adipogenic and thermogenic protein expression of murine WT and ENT1-KO BA
(A) Representative Western Blots of murine WT and ENT1-KO (KO) BA and (B) quantification of the adipogenic markers aP2 and PPARγ and the thermogenic marker UCP1. Expression data were normalized to Calnexin and are represented as mean ± SEM. t-test, n=6. *p≤0.05, **p≤0.01

Next, white pre-adipocytes were isolated from WT and global ENT1-KO mice and differentiated to mature WA. Staining of lipid droplets by Oil Red O staining revealed a larger stained area of ENT1-KO WA in comparison to WT cells (Figure 23A) suggesting improved differentiation of ENT1-KO WA. qRT-PCR analysis showed significantly decreased (p≤0.005) *Slc29a1*-mRNA expression in ENT1-KO WA, while expression levels of the adipogenic genes *Adipoq*, *Fabp4*, *Pparg* as well as the thermogenic markers *Ucp1* and *Ppargc1a* were significantly increased in ENT1-deficient WA (+535%, +459%, +125%, +2256% and +266%, respectively) (Figure 23B-G).
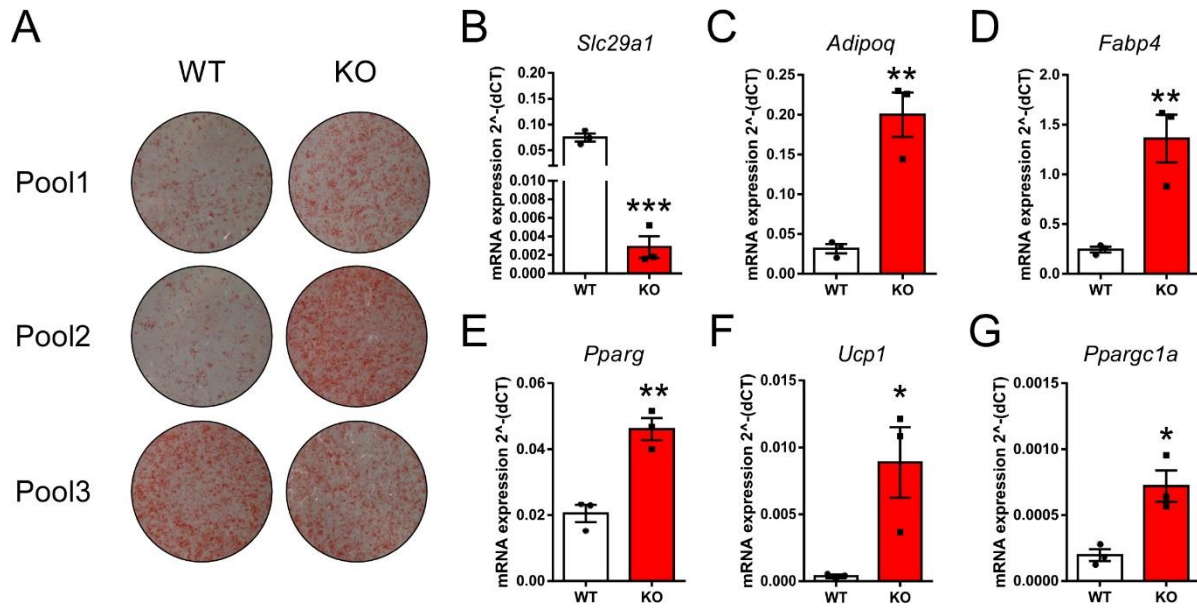
Figure 23 Differentiation of murine WT and ENT1-KO WA
(A) Representative Oil Red O stainings, mRNA expression values of (B) *Slc29a1*, the adipogenic marker genes (C) *Adipoq*, (D) *Fabp4* and (E) *Pparg* and the thermogenic marker genes (F) *Ucp1* and (G) *Ppargc1a* in murine WT and ENT1-KO (KO) WA. qRT-PCR values were normalized to *Hprt*. Results are represented as mean ± SEM. t-test, n=3. *p≤0.05, **p≤0.01, ***p≤0.005

Taken together, depletion of ENT1 resulted in improved differentiation and thermogenic gene expression of BA and WA.

4.4.1.2. Lipolysis and mitochondrial respiration of ENT1-KO brown and white adipocytes

As a functional assay, lipolysis of WT and ENT1-KO BA was measured. Cells were either not treated or stimulated with 1µM NE to mimic sympathetic activation. The basal lipolytic rate and NE-stimulated lipolysis were significantly increased in ENT1-KO BA (+177% and +58%, respectively; p≤0.05) compared to WT cells (Figure 24A). Next, mitochondrial respiration was investigated using a Seahorse XFe24 Analyzer. The basal oxygen consumption rate of ENT1-KO BA was significantly enhanced (+50%; p≤0.005) in comparison to WT BA (Figure 24B, C). Uncoupling efficiency, which is an important metabolic parameter as it reflects bioenergetic efficiency, was significantly increased by 73% (+11.30 ± 3.66pp; p≤0.01) in BA lacking ENT1 (Figure 24D).
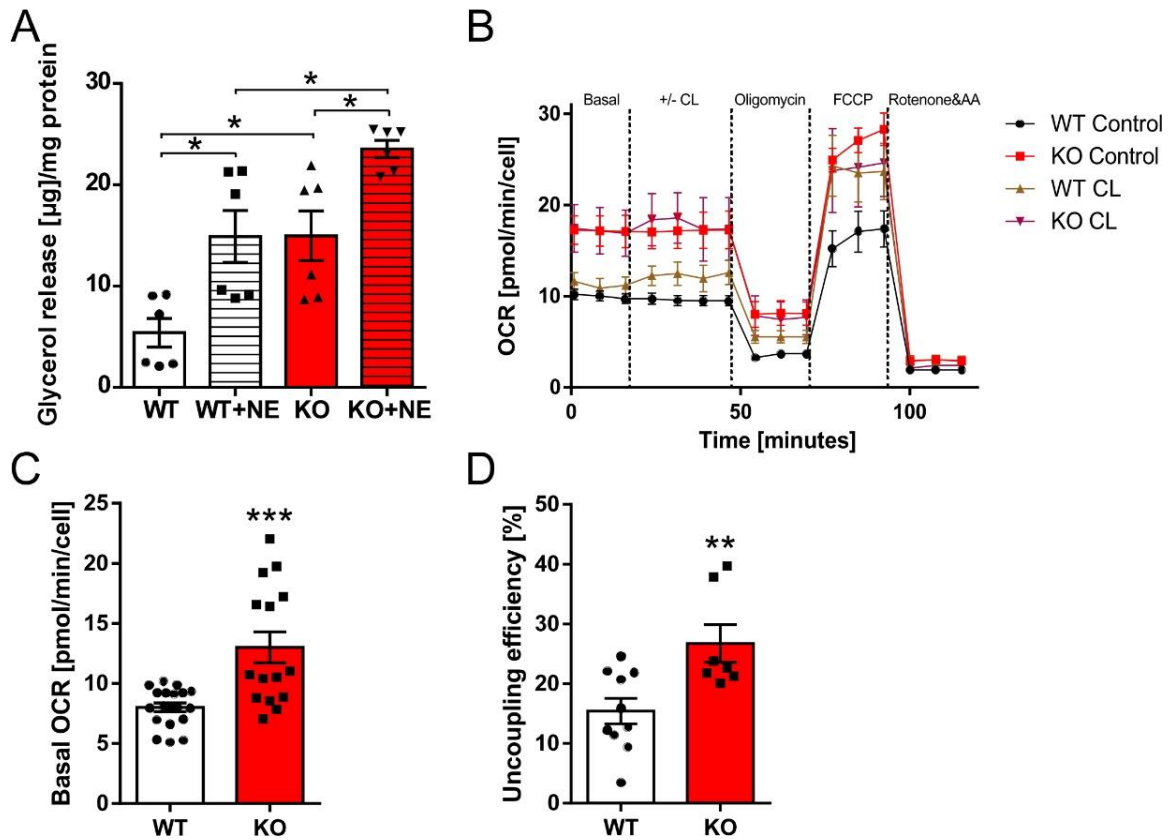
Figure 24 Lipolysis and mitochondrial respiration of murine WT and ENT1-KO BA
(A) Basal and NE-stimulated lipolysis, (B) Mito Stress Assay (Seahorse XFe24 Analyzer) and quantification of (C) basal respiration and (D) uncoupling efficiency of murine WT and ENT1-KO (KO) BA. Data were normalized to protein content for lipolysis assay and to number of cells for seahorse measurements. Results are represented as mean ± SEM. t-test, except for A: ANOVA was applied, n=6 for lipolysis, n=7-19 for seahorse experiments. *p≤0.05, **p≤0.01, ***p≤0.005

Within further experiments, the effect of ENT1-deletion on WA' function was investigated. Lipolysis measurements showed increased basal glycerol release of ENT1-deficient WA (+43%; p≤0.05) compared to WT cells (Figure 25A). Moreover, basal and uncoupled respiration were significantly enhanced in ENT1-KO WA (+16% and +30%, respectively) (Figure 25B, C, E). In addition, the effect of the β3-adrenergic agonist CL-316243 on mitochondrial respiration was stronger (p≤0.01) in ENT1-deficient WA (Figure 25B, D).
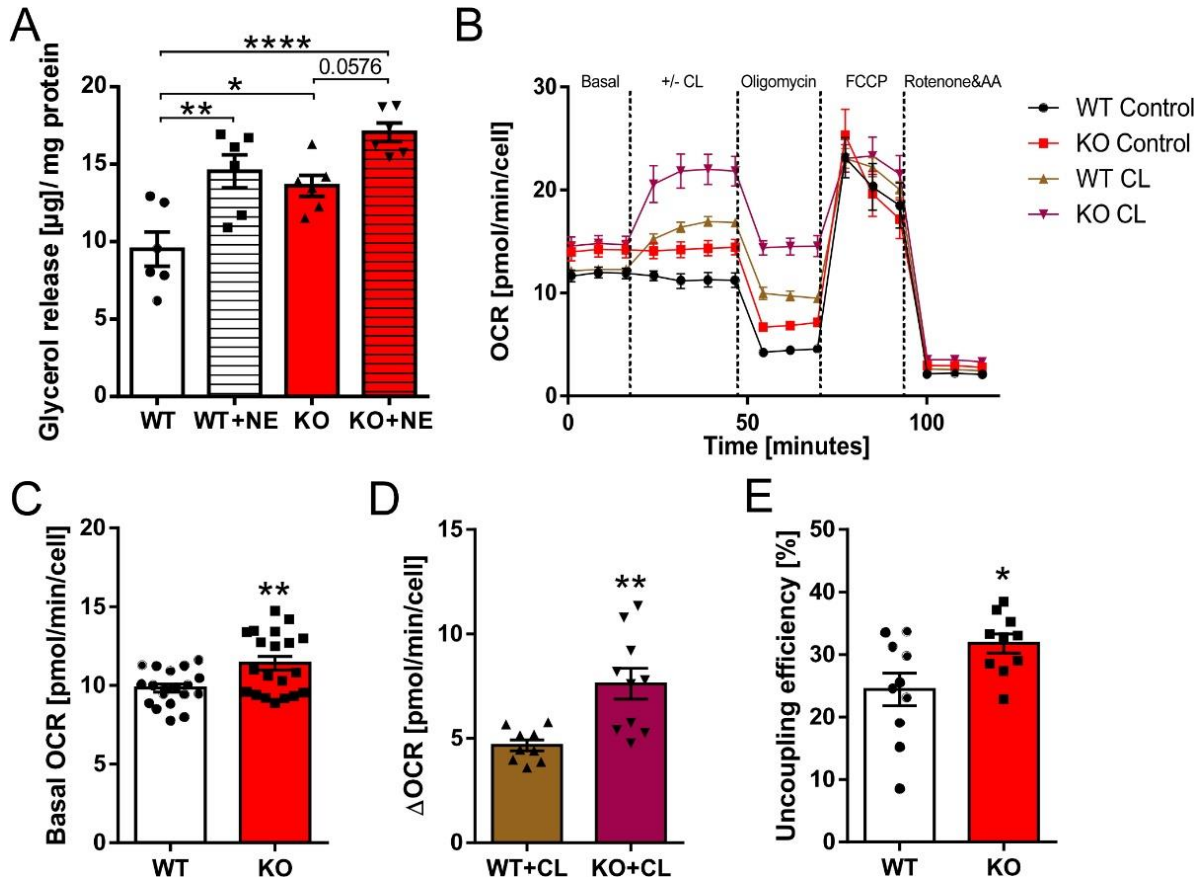
Figure 25 Lipolysis and mitochondrial respiration of murine WT and ENT1-KO WA
(A) Basal and NE-stimulated lipolysis, (B) Mito Stress Assay (Seahorse XFe24 Analyzer) and quantification of (C) basal respiration, (D) acute response to CL-316243 treatment (difference between CL and control values) and (E) uncoupling efficiency of murine WT and ENT1-KO (KO) WA. Data were normalized to protein content for lipolysis assay and to number of cells for seahorse measurements. Results are represented as mean ± SEM. t-test, except for A: ANOVA was applied, n=6 for lipolysis, n=9-20 for seahorse experiments. *p≤0.05, **p≤0.01, ****p≤0.001

In summary, loss of ENT1 led to improved adipogenic and thermogenic function of BA and WA.

4.4.2. Lipolysis and oxygen consumption of ENT1-KO adipose tissues

Next, lipolysis of adipose tissue explants from WT and global ENT1-KO mice was measured. *Ex vivo* lipolysis was upregulated in BAT (+37%), WATi (+96%) and WATg (+113%) depots of global ENT1-KO mice in comparison to WT animals (+0.34 ± 0.13µg glycerol/mg protein, +0.18 ± 0.06µg glycerol/mg protein and +0.16 ± 0.05µg glycerol/mg protein, respectively; p≤0.05) (Figure 26).
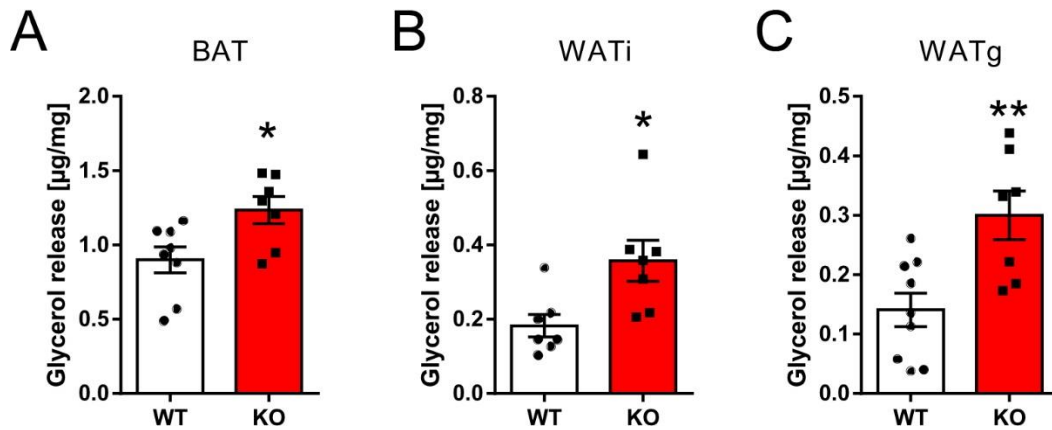
Figure 26 *Ex vivo* lipolysis of BAT, WATi and WATg explants of WT and global ENT1-KO mice
Glycerol release of (A) BAT, (B) WATi and (C) WATg isolated from 8-week-old WT and global ENT1-KO (KO) mice. Data were normalized to tissue weights. Results are represented as mean ± SEM. t-test, n=7. *p≤0.05, **p≤0.01

Oxygraph measurements showed that basal oxygen consumption of ENT1-KO BAT (1.05 ± 0.09nmol/min/mg) was increased by 81% (p≤0.05) and UCP1-mediated oxygen consumption was increased by 310% (p≤0.01) compared to WT BAT (Figure 27A, B). Basal respiration of white inguinal adipose tissue depots was increased by 49% in ENT1-KO WATi (0.19 ± 0.03nmol/min/mg), but this difference was not statistically significant (Figure 27C). Measured UCP1-mediated respiration rate was 176% higher (p≤0.05) in ENT1-KO WATi compared to WT tissues (Figure 27D).
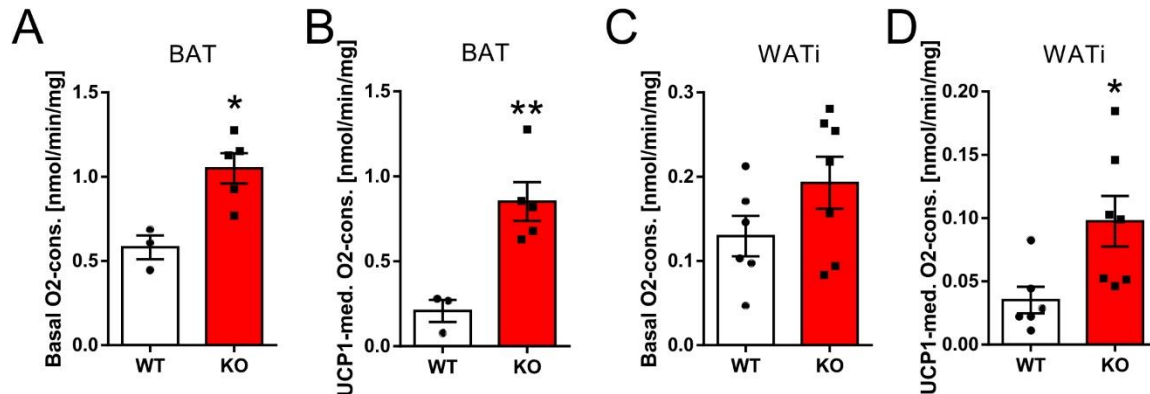
Figure 27 *Ex vivo* oxygen consumption of BAT and WATi of WT and global ENT1-KO mice
(A) Basal oxygen consumption and (B) UCP1 mediated oxygen consumption of BAT isolated from 8-week-old WT and global ENT1-KO (KO) mice. (C) Basal oxygen consumption and (D) UCP1 mediated oxygen consumption of WATi isolated from 8-week-old WT and global ENT1-KO (KO) mice. Oxygen consumption was measured using Oxygraph O2k apparatus and UCP1 mediated oxygen consumption was calculated as the difference of oxygen concentrations after substrates administration (octanoylcarnitine, pyruvate, malate, glutamate and succinate) and GDP injection. Data were normalized to tissue weights and are represented as mean ± SEM. t-test, n=3-7. *p≤0.05, **p≤0.01

Taken together, metabolic function and thermogenic properties were elevated in BAT and WAT of global ENT1-KO mice *ex vivo*. These findings were in line with the metabolic phenotype of ENT1-deficient adipocytes observed in the *in vitro* experiments.

4.4.3. Glucose- and fatty acids-uptake of global ENT1-KO mice

To identify organs, which consume additional energetic substrates during (increased) metabolic activity, radioactively labelled glucose and fatty acids were administered to global ENT1-KO and WT mice. A significantly increased uptake of ^{3}H-DOG and ^{14}C-Triolein in WATi depots was observed for ENT1-KO animals (1.5 ± 0.15-fold and 1.5 ± 0.22-fold, respectively) (Figure 28). In addition, a tendency (p=0.0785) for elevated ^{14}C-Triolein uptake was observed in BAT of ENT1-KO mice (Figure 28B).
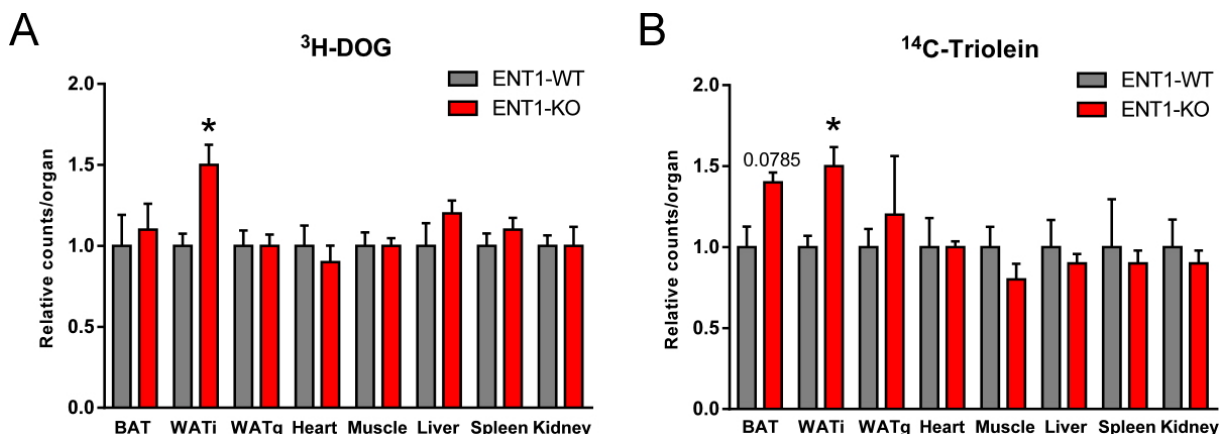
Figure 28 Organ specific uptake of glucose and fatty acids of WT and global ENT1-KO mice
Relative counts of (A) ^{3}H-DOG and (B) ^{14}C-Triolein in respective organs of 8-week-old WT and global ENT1-KO mice (2 hours after oral administration). Results are represented as mean + SEM. Multiple t-tests (corrected for multiple comparisons), n=5. *p≤0.05

4.4.4. Fat mass of global ENT1-KO mice

Body composition of 18-week-old WT and global ENT1-KO mice was measured by NMR. The analysis revealed significantly reduced fat mass in animals lacking ENT1(-3.83 ± 1.50 pp; p≤0.05) compared to WT littermates (Figure 29A). Moreover, inguinal and gonadal fat pads of ENT1-KO mice were 27% and 25% lighter, respectively (p≤0.05) (Figure 29B). To rule out that reduced fat mass is mediated by intestinal malabsorption of global ENT1-KO animals (if global deletion of ENT1 would affect the intestine), bomb calorimetry was applied to measure the energy content of feces of WT and ENT1-KO mice. The results indicate that the amount of energy excreted *via* the feces was not significantly different between the two genotypes (Figure 29C), while food intake was also similar (Figure 29D).
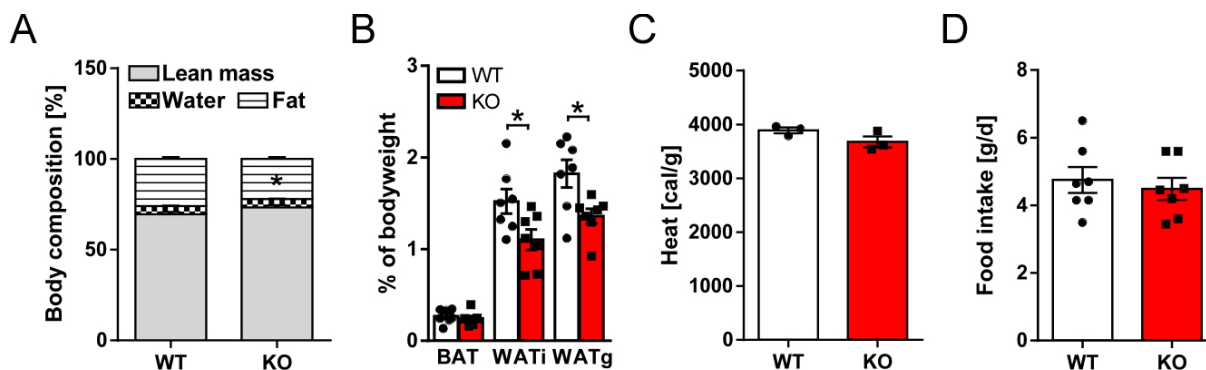
Figure 29 Body composition, adipose tissue weights, energy content of feces and food intake of WT and global ENT1-KO mice
(A) Body composition, (B) adipose tissue weights, (C) energy content of feces and (D) food intake of 18-week-old male WT and global ENT1-KO (KO) mice, which were fed a CD for 12 weeks. Results are represented as mean ± SEM. t-test, n=7, except for C: n=3. *p≤0.05

4.4.5. Effects of global ENT1-deletion on bodyweight and glucose tolerance under high fat diet

Since ENT1-KO adipocytes and ATs showed a promoted metabolic function, it was hypothesized that ENT1-deletion might counteract metabolic imbalance and DIO. To test this hypothesis, global ENT1-KO mice and WT littermates were fed a HFD for 12 weeks, while a control group received a CD.

Mice, which were fed a CD, did not show differences in weight gain between the two genotypes during 12 weeks of observation (Figure 30A, B). Remarkably, ENT1-KO animals gained significantly less weight (-5.08 ± 1.13g; -38%; p≤0.005) compared to WT littermates during 12 weeks of HFD (Figure 30B). The bodyweight curves separated from the third week of HFD onwards (Figure 30A). In addition, NMR measurement revealed changes in body composition between WT and KO. Relative fat mass of ENT1-KO mice was significantly decreased by 8.78 ± 2.79 percentage points (-22%) after HFD in comparison to WT animals (Figure 30C). While BAT mass was not affected, ENT1-KO animals exhibited significantly reduced WATg weights (-1.72 ± 0.34pp; p≤0.005) (Figure 30D). After 12 weeks of HFD, WATi and WATg depots of ENT1-KO mice weighed 26% and 41% less, respectively, in comparison to the WT tissues (Figure 30D).
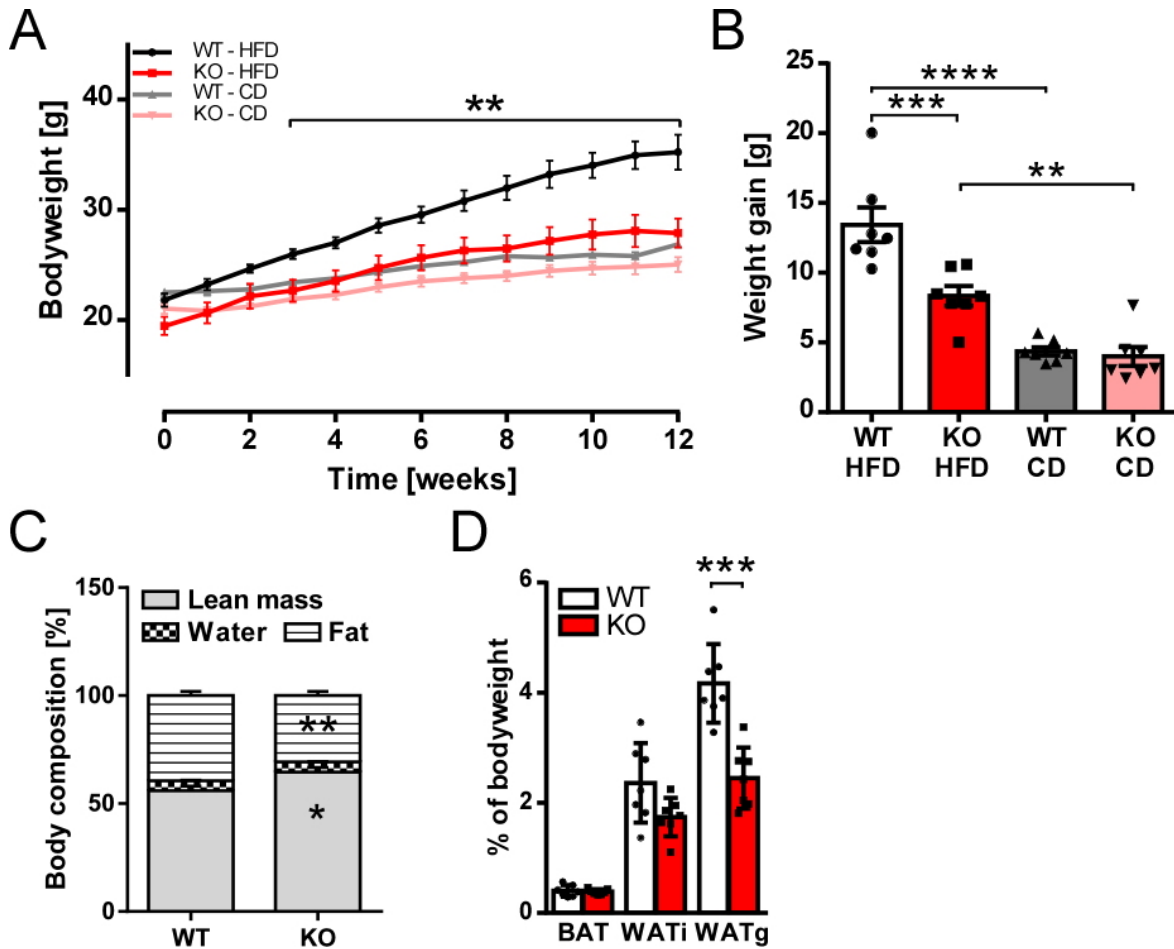
Figure 30 Weight gain and body composition of WT and global ENT1-KO mice after HFD
(A) Bodyweight and (B) weight gain of WT and global ENT1-KO (KO) mice during/after 12 weeks of CD or HFD.
(C) Body composition and (D) weight of adipose tissues of WT and global ENT1-KO (KO) mice after 12 weeks of
HFD. Results are represented as mean ± SEM. ANOVA was applied for A and B, t-test for C and D. n=7, *p≤0.05,
**p≤0.01, ***p≤0.005

Furthermore, the ENT1-KO animals showed improved glucose tolerance after 11 weeks of
HFD, when challenged with a glucose tolerance test (GTT) (Figure 31A, B). Inosine plasma
levels of WT mice were decreased after HFD compared to CD (p≤0.05) (Figure 31C). In
contrast, inosine plasma concentrations of ENT1-KO mice were not significantly different after
CD and HFD, while inosine plasma concentrations of ENT1-KO animals after HFD were
significantly higher in comparison to WT (HFD) littermates (Figure 31C). This finding was in
line with the *in vitro* data showing that deletion of ENT1 led to increased endogenous
extracellular inosine concentrations.
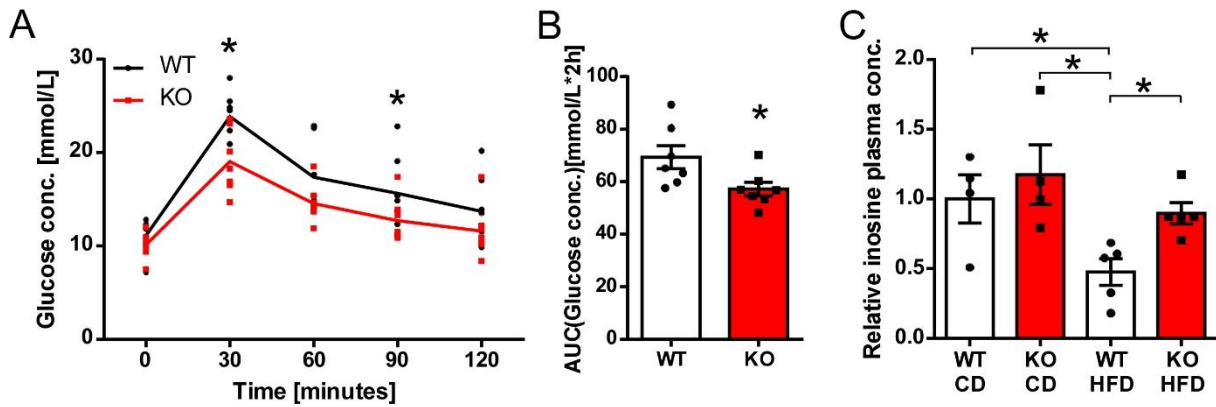
Figure 31 GTT and inosine plasma concentrations of WT and global ENT1-KO mice after HFD
(A) Glucose tolerance test (GTT) and (B) AUCs of glucose concentrations of WT and global ENT1-KO (KO) mice after 11 weeks of HFD. (C) Inosine plasma concentrations of WT and global ENT1-KO (KO) mice after 12 weeks of CD or HFD. Results are represented as mean ± SEM. t-test, except for C: ANOVA. n=7, except for C: n=4-5. *p≤0.05

4.4.6. Energy expenditure of global ENT1-KO mice after high fat diet

To investigate the metabolic properties of global ENT1-KO animals after HFD, indirect calorimetry was measured using metabolic cages. Analysis of (whole-body) oxygen consumption at 23°C revealed that HFD-fed ENT1-KO mice consumed significantly more oxygen compared to WT littermates indicating higher EE (Figure 32A, B, C). The mean of $V(O_2)$ was increased by 23% in ENT1-KO animals (p≤0.005) (Figure 32B). ENT1-KO mice moved less (p≤0.01) during the night cycle, while food intake was not different between the genotypes (Figure 32D, E). To analyze the maximal thermogenic capacity of ENT1-KO mice after HFD, oxygen consumption upon acute cold exposure at 4°C was measured. The obtained results showed increased oxygen consumption of ENT1-KO mice (66min: 6.39 ± 0.34ml/h/g; p≤0.05) at 4°C after 42 minutes until the last measurement (after 66 minutes) as compared to WT animals (66min: 5.20 ± 0.36ml/h/g) (Figure 32F).
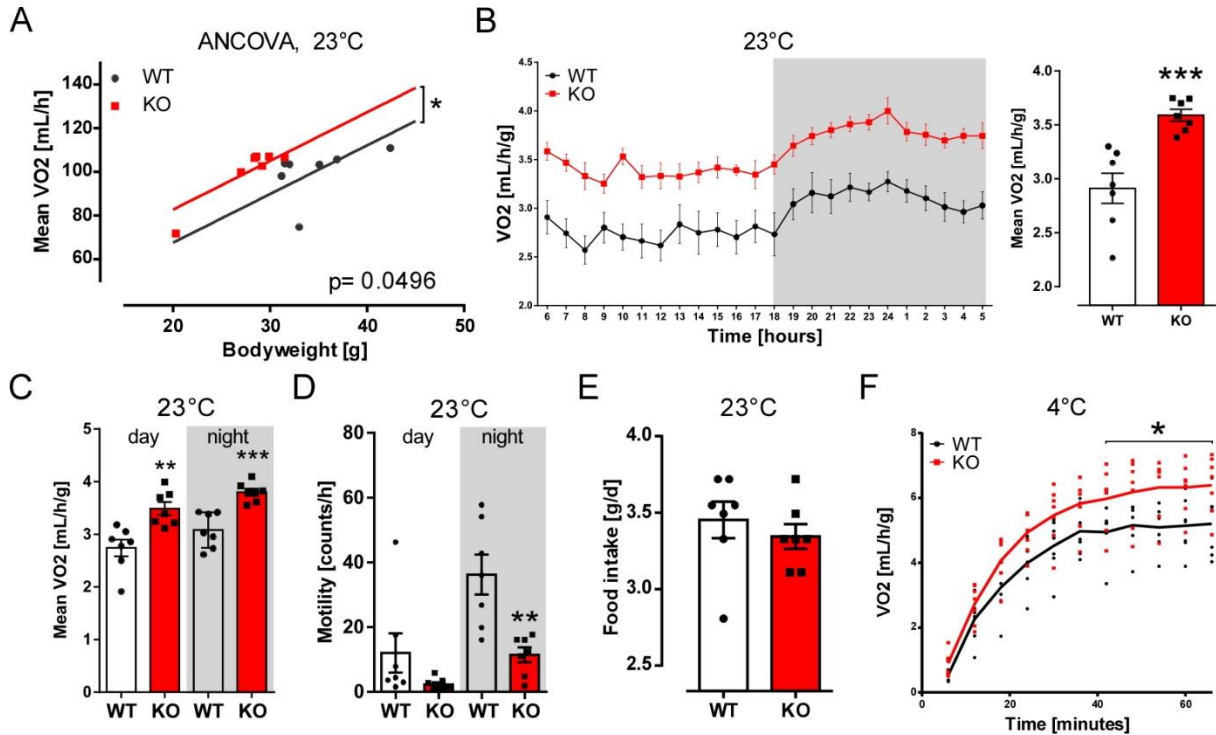
Figure 32 Oxygen consumption of WT and global ENT1-KO mice after HFD
(A) ANCOVA (mean(VO2) vs. bodyweight), (B) oxygen consumption during 24 hours, (C) oxygen consumption during day and night cycle (12 hours each), (D) motility and (E) food intake at 23°C of WT and global ENT1-KO (KO) mice after 12 weeks of HFD. (F) Oxygen consumption of WT and global ENT1-KO (KO) mice during acute cold exposure at 4°C after 12 weeks of HFD. Results are represented as mean ± SEM. t-test, except for A: ANCOVA. n=7. *p≤0.05, **p≤0.01, ***p≤0.005

Moreover, after HFD, loss of ENT1 resulted in significantly elevated mRNA-expression of *Ucp1* and *Ppargc1a* in BAT (+50% and +83%, respectively) (Figure 33A, B). In addition, UCP1 protein expression after HFD was significantly increased in ENT1-KO BAT (1.86 ± 0.36; p≤0.05) in comparison to control tissues (Figure 33C, E).

After 12 weeks of HFD, indicative of the typical 'whitening' effect of DIO in BAT, an increased number of unilocular adipocytes were detected in BAT of WT mice compared to the CD group of WT animals (Figure 33D, E). Moreover, this effect was associated with increased cell size of WT BAT after HFD compared to CD (p≤0.01, Figure 33D-F). Histological analyses after HFD showed significantly smaller (p≤0.01) adipocyte size in ENT1-KO BAT (12.02 ± 0.64µm^2) compared to WT tissues (16.46 ± 1.36µm^2), while after CD no significant difference in adipocytes' area was observed between the two genotypes (WT: 11.41 ± 0.40µm^2; KO: 9.19 ± 0.86µm^2) (Figure 33D-F).
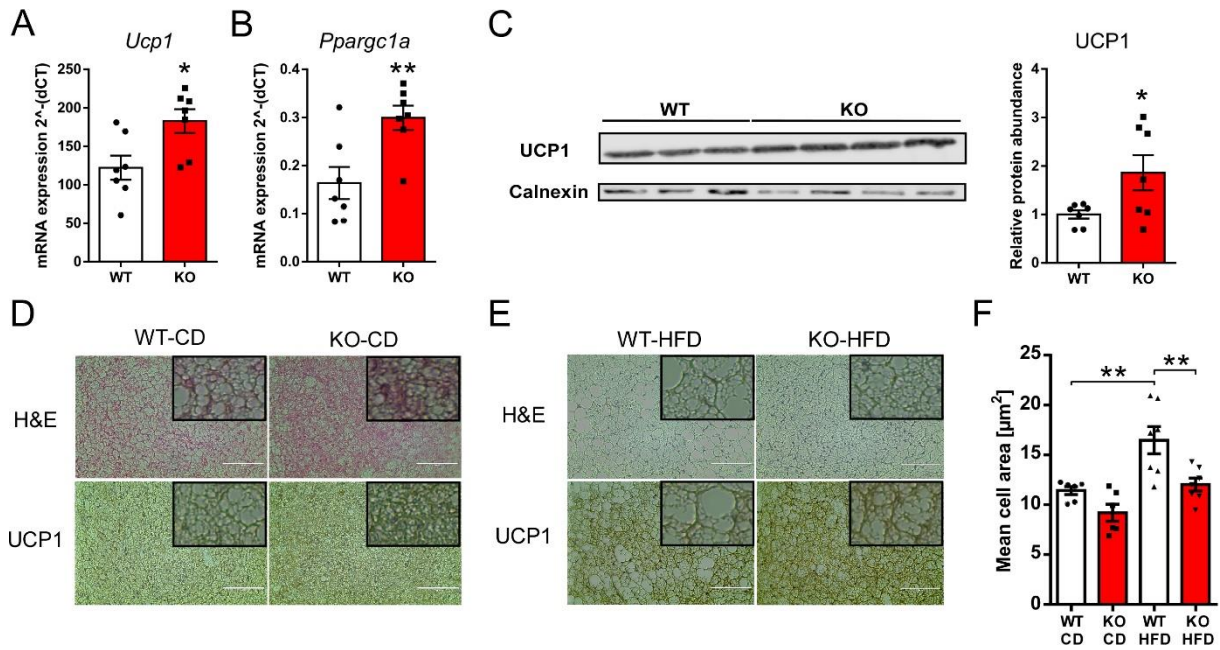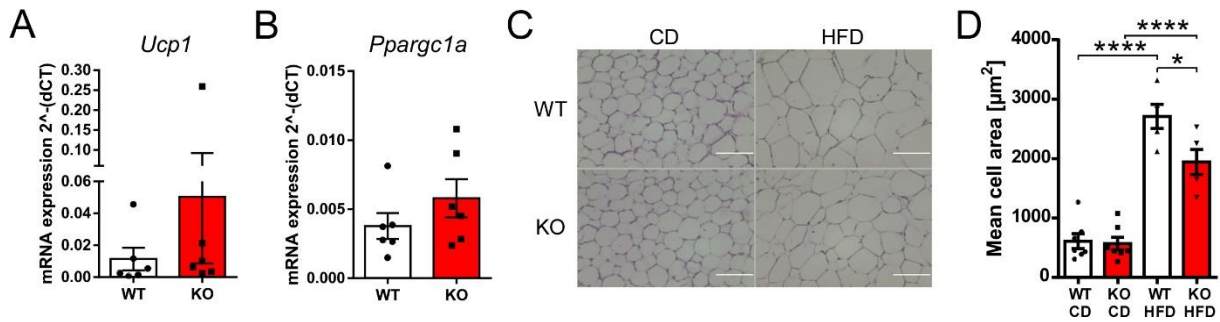
Figure 33 Expression of thermogenic genes and cell morphology of BAT of WT and global ENT1-KO mice after HFD

mRNA expression of (A) *Ucp1* and (B) *Ppargc1a* (values were normalized to *Hprt*), (C) representative Western-Blot and quantification of UCP1 (expression data of Western-Blots were normalized to Calnexin) of BAT of WT and global ENT1-KO (KO) mice after 12 weeks of HFD. Representative H&E and UCP1 stainings of WT and ENT1-KO (KO) BAT after 12 weeks of (D) CD and (E) HFD (the scale bar corresponds to 100μm; upper right corner: 4-fold magnification). (F) Quantification of cell area of BAT of WT and ENT1-KO (KO) mice after 12 weeks of CD or HFD. Results are represented as mean ± SEM. t-test, except for F: ANOVA. 7 mice per genotype were analyzed after HFD and 6 after CD. *p≤0.05, **p≤0.01

Analysis of WATi revealed 18-fold increased (p=0.1767) mRNA expression of *Ucp1* in ENT1-KO mice compared to WT animals after HFD (Figure 34A). Expression levels of the thermogenic gene *Ppargc1a* were 5-fold elevated in ENT1-KO WATi, albeit this increase was not statistically significant (p=0.0552) (Figure 34B). Moreover, expression of UCP1 protein was increased in the histology sections of WATi of ENT1-KO mice in comparison to WT littermates after CD and HFD (Figure 34C, D). In addition, histological analyses revealed significantly smaller (p≤0.01) adipocyte size in ENT1-KO WATi (596.1 ± 123.9μm^2) compared to WT tissues (1446 ± 278.1μm^2), after HFD (Figure 34D, E). In contrast, no statistically significant difference in adipocytes' area between the two genotypes was observed in the CD groups (WT: 410.9 ± 48.63μm^2; KO: 200.0 ± 22.29μm^2) (Figure 34C, E).
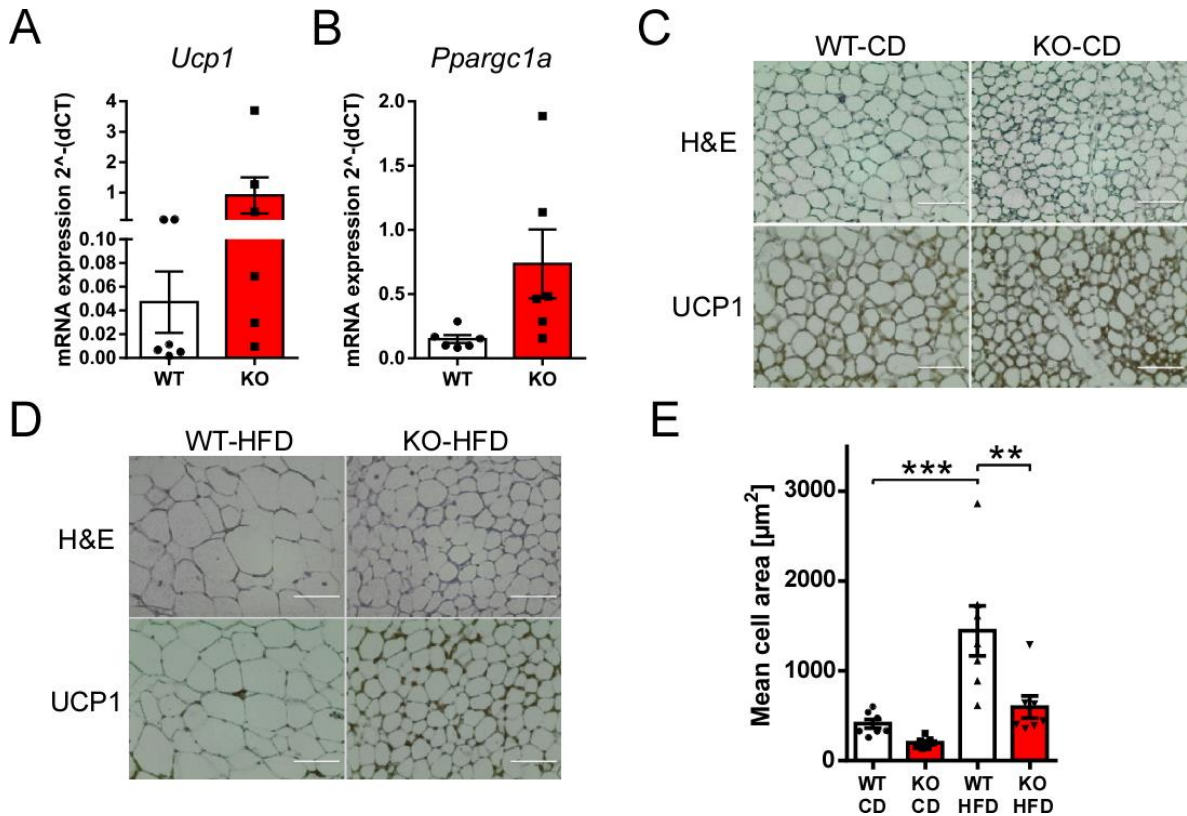
Figure 34 Expression of thermogenic genes and cell morphology of WATi of WT and global ENT1-KO mice after HFD

mRNA expression of (A) *Ucp1* and (B) *Ppargc1a* in WATi of WT and global ENT1-KO (KO) mice after 12 weeks of HFD (values were normalized to *Hprt*). Representative H&E and UCP1 stainings of WT and global ENT1-KO (KO) WATi after 12 weeks of (C) CD and (D) HFD (the scale bar corresponds to 100µm). (E) Quantification of cell area of WATi isolated from WT and global ENT1-KO (KO) mice after 12 weeks of CD or HFD. Results are represented as mean ± SEM. t-test, except for E: ANOVA. n=6-7. **p≤0.01, ***p≤0.005

After 12 weeks of HFD, expression levels of *Ucp1* and *Ppargc1a* in WATg were not statistically different between WT and ENT1-KO mice (Figure 35A, B). However, the cell size of gonadal WA was significantly smaller (p≤0.05) in ENT1-KO mice (1943 ± 209.7µm^2) as compared to WT littermates (2709 ± 202.3µm^2) (Figure 35C, D). No differences in cell area were observed between the genotypes in the CD groups (Figure 35C, D).

Figure 35 Expression of thermogenic genes and cell morphology of WATg of WT and global ENT1-KO mice after HFD
mRNA expression of (A) *Ucp1* and (B) *Ppargc1a* in WATg of WT and global ENT1-KO (KO) mice after 12 weeks of HFD (values were normalized to *Hprt*). (C) Representative H&E stainings (the scale bar corresponds to 100µm) and (D) quantification of cell area of WATg of WT and global ENT1-KO (KO) mice after 12 weeks of CD or HFD. Results are represented as mean ± SEM. t-test, except for D: ANOVA. n=5-7. *p≤0.05, ****p≤0.001

Taken together, global deletion of ENT1 led to increased extracellular inosine levels and activation of thermogenic AT during HFD. Thereby, whole body EE of ENT1-KO mice was increased and weight gain during DIO was reduced.

4.4.7. Adipocyte-specific knockout of ENT1

To investigate whether the observed phenotype of global ENT1-KO mice is mediated by loss of ENT1 in adipocytes, an adipocyte-specific KO (ENT1-A-KO) mouse model was generated and studied. In these 'ENT1fl-ApnCre' mice the loxP flanked/floxed sequence of the *Slc29a1* gene (ENT1fl) (Choi et al., 2004) was deleted under the control of the adipocyte specific adiponectin promoter Cre (ApnCre). ENT1-A-KO mice (homozygote floxed, Cre-positive, ENT1$^{fl/fl}$ ApnCre+) were compared to homozygote floxed, Cre-negative littermates (Control: ENT1$^{fl/fl}$ ApnCre-).

mRNA analysis of AT depots of 8-week-old male mice showed a 48% knockdown (KD) of the target gene *Slc29a1* in A-KO-BAT and 57% reduced expression in A-KO-WATi compared to control mice (Figure 36A, B). The KD efficiency in WATg amounted to only 23% and this reduction in comparison to the control group was not significant (Figure 36C). As a negative control, expression levels of *Slc29a1* in the liver were analyzed, which showed no difference between the two genotypes (Figure 36D). To rule out a compensatory mechanism by ENT2 in the ENT1-A-KO model, also mRNA expression of *Slc29a2* was measured by qRT-PCR. The obtained results showed no significant differences in expression levels of *Slc29a2* in BAT, WATi, WATg and liver of ENT1-A-KO and control mice (Figure 36E-H).
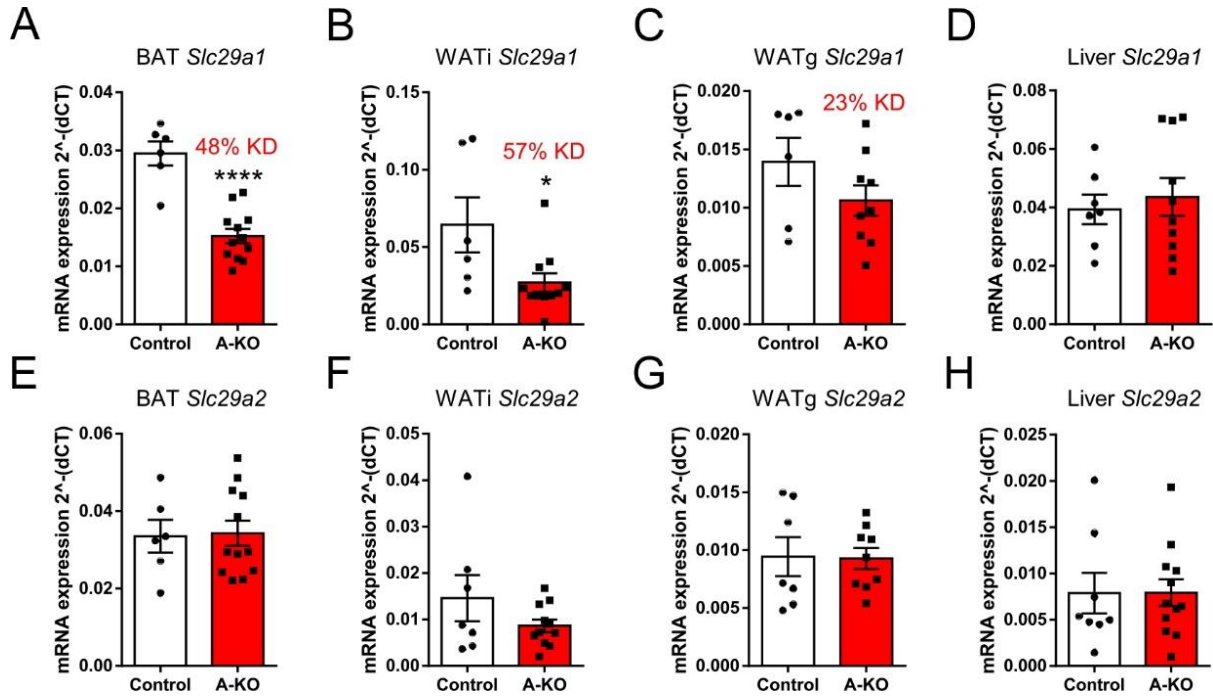
Figure 36 Knockdown efficiency of the ENT1fl-ApnCre mouse model
mRNA expression of *Slc29a1* in (A) BAT, (B) WATi, (C) WATg and (D) liver; and mRNA expression of *Slc29a2* in (E) BAT, (F) WATi, (G) WATg and (H) liver of 8-week-old male ENT1fl-ApnCre mice (A-KO: ENT1$^{fl/fl}$ ApnCre+, Control: ENT1$^{fl/fl}$ ApnCre-). Expression values were normalized to *Hprt*. Results are represented as mean ± SEM. t-test, n=6-12. *p≤0.05, ****p≤0.001

4.4.8. Effects of adipocyte-specific deletion of ENT1 on mitochondrial respiration and lipolysis of brown and white adipose tissue

In the next series of experiments, mitochondrial respiration was measured *ex vivo* and *in vitro*. BAT and WATi isolated from 8-week-old male ENT1-A-KO mice showed significantly enhanced basal (+42% and +61%, respectively) and UCP1-mediated (+120% and +95%, respectively) oxygen consumption in comparison to control tissues (Figure 37A-D). In addition, mitochondrial respiration of primary WA isolated from ENT1fl-ApnCre mice was measured by Seahorse Mito Stress Assay. ENT1-A-KO WA consumed significantly more oxygen during basal (+69%) and CL-316243-stimulated respiration (+259%) compared to control WA (Figure 37E-G). Moreover, the ENT1-A-KO WA showed a significantly higher rate of uncoupled/UCP1-mediated respiration (+17.34 ± 1.95pp; p≤0.001) (Figure 37H).
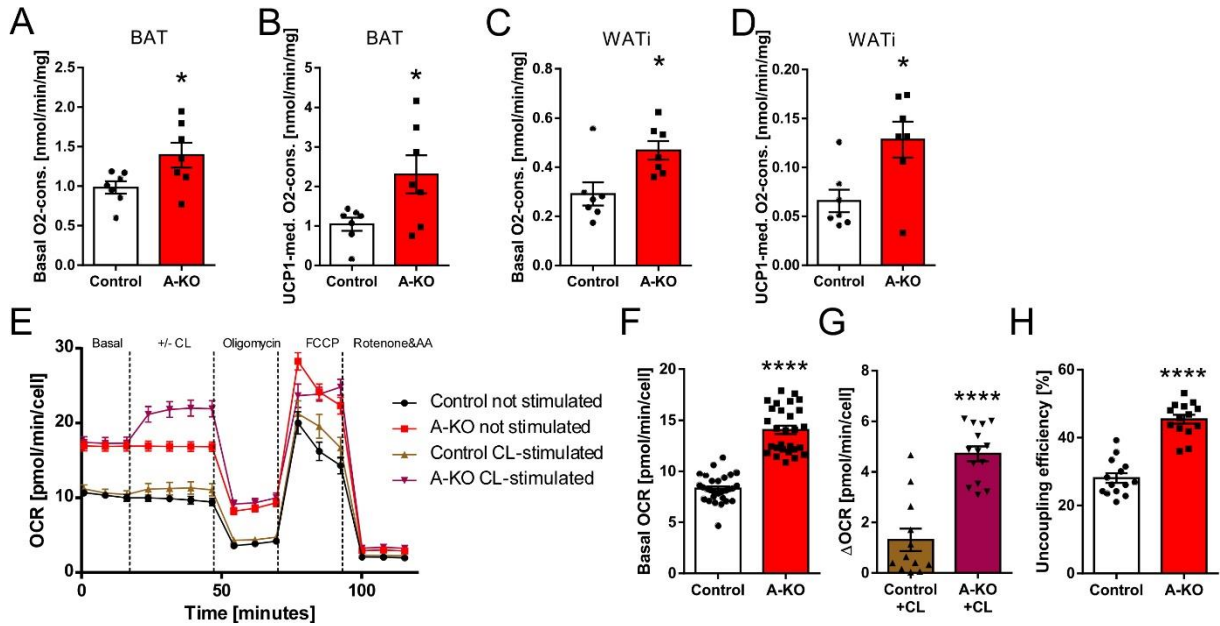
Figure 37 Oxygen consumption of ENT1fl-ApnCre BAT and WATi
(A) Basal oxygen consumption and (B) UCP1-mediated oxygen consumption of BAT; (C) Basal oxygen consumption and (D) UCP1-mediated oxygen consumption of WATi of 8-week-old ENT1fl-ApnCre mice (A-KO: ENT1$^{fl/fl}$ ApnCre+, Control: ENT1$^{fl/fl}$ ApnCre-). Oxygen consumption was measured using Oxygraph O2k apparatus, data were normalized to tissue weights and UCP1-mediated oxygen consumption was calculated as the difference of oxygen concentrations after substrates administration (octanoylcarnitine, pyruvate, malate, glutamate and succinate) and GDP injection. (E) Mito Stress Assay (Seahorse XFe24 Analyzer) and quantification of (F) basal respiration, (G) response to CL-316243 and (H) uncoupling efficiency of murine ENT1-A-KO and ENT1-floxed control WA. Results are represented as mean ± SEM. t-test, n=7 for Oxygraph measurements, n=14 for Seahorse experiments. *p≤0.05, ****p≤0.001

Furthermore, elevated lipolysis was observed in BAT (+16%; p≤0.05) and WATi (+57%; p≤0.01) explants of ENT1-A-KO mice (Figure 38A, B) as compared to control tissues, while WATg samples did not show significant differences between the two genotypes (Figure 38C).
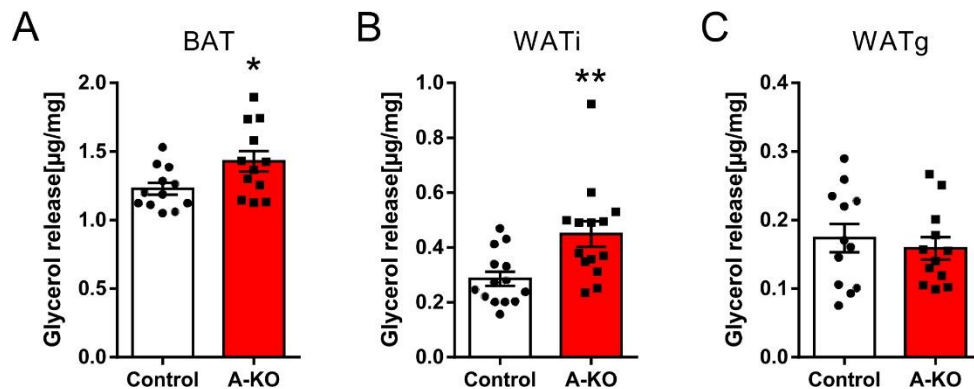
Figure 38 Lipolysis of adipose tissue explants of ENT1fl-ApnCre mice
Ex vivo lipolysis of (A) BAT, (B) WATi and (C) WATg of 8-week-old ENT1-A-KO and ENT1-floxed control mice (A-KO: ENT1$^{fl/fl}$ ApnCre+, Control: ENT1$^{fl/fl}$ ApnCre-). Data were normalized to tissue weights. Results are represented as mean ± SEM. t-test, n=12. *p≤0.05, **p≤0.01

In summary, ENT1-A-KO BAT and WATi showed improved metabolic properties in comparison to control tissues.

4.4.9. Adipogenic and thermogenic gene expression of primary ENT1-A-KO adipocytes

Next, to further investigate the metabolic phenotype of ENT1-A-KO ATs, primary BA and WA were isolated from ENT1fl-ApnCre mice, differentiated and analyzed by qRT-PCR. ENT1-A-KO BA and WA showed increased mRNA expression values of the adipogenic genes *Fabp4*, *Pparg* and *Adipoq* as well as of the thermogenic markers *Ucp1* and *Ppargc1a* compared to control cells (Figure 39).
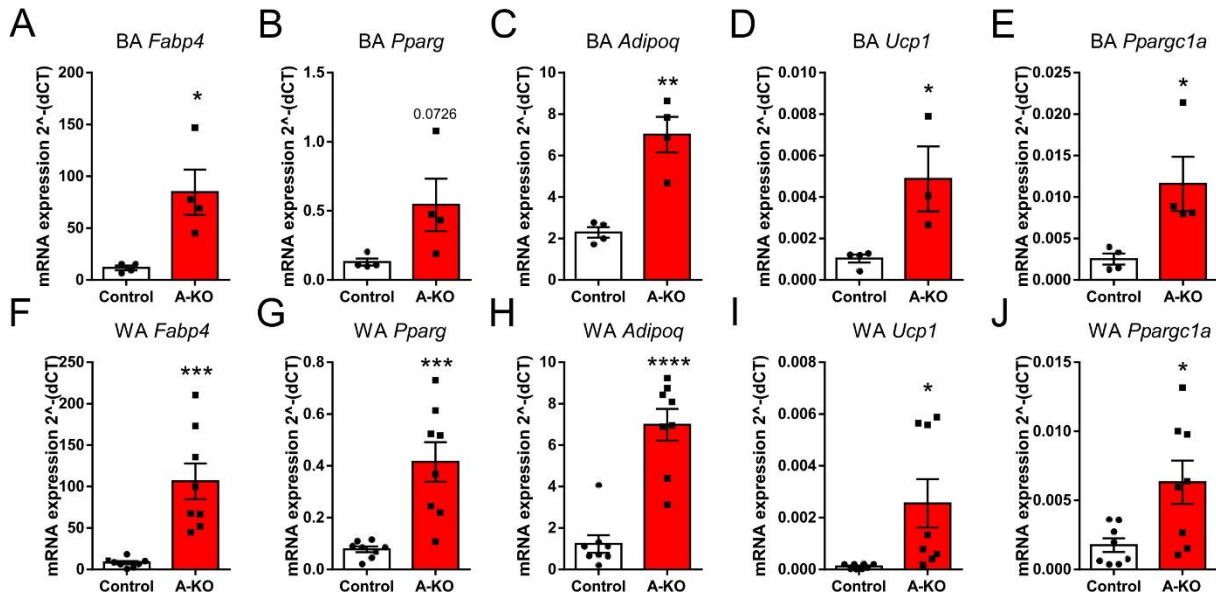
Figure 39 Expression of adipogenic and thermogenic genes in ENT1fl-ApnCre BA and WA
mRNA expression of the adipogenic genes (A) *Fabp4*, (B) *Pparg*, (C) *Adipoq* and the thermogenic marker genes (D) *Ucp1* and (E) *Ppargc1a* in primary ENT1fl-ApnCre BA (A-KO: ENT1$^{fl/fl}$ ApnCre+, Control: ENT1$^{fl/fl}$ ApnCre-). mRNA expression of the adipogenic genes (F) *Fabp4*, (G) *Pparg*, (H) *Adipoq* and the thermogenic marker genes (I) *Ucp1* and (J) *Ppargc1a* in primary ENT1fl-ApnCre WA. Expression values were normalized to *Hprt*. Results are represented as mean ± SEM. t-test, 4 cell pools of BA and 8 pools of WA were analyzed. *$p \leq 0.05$, **$p \leq 0.01$, ***$p \leq 0.005$, ****$p \leq 0.001$

4.4.10. Oxygen consumption of adipocyte-specific ENT1-A-KO mice

Finally, *in vivo* studies of ENT1-A-KO mice were performed. The analyzed 8-week-old male ENT1-A-KO mice showed no statistically significant differences in bodyweight and adipose tissue weights compared to ENT1-floxed control littermates (Figure 40A, B). WATi depots of ENT1-A-KO animals weighed 17% less (Figure 40B). Furthermore, food intake and the amount of energy secreted by the feces were not different (Figure 40C, D), while the ENT1-A-KO animals moved less during the night cycle ($p \leq 0.01$) (Figure 40E).
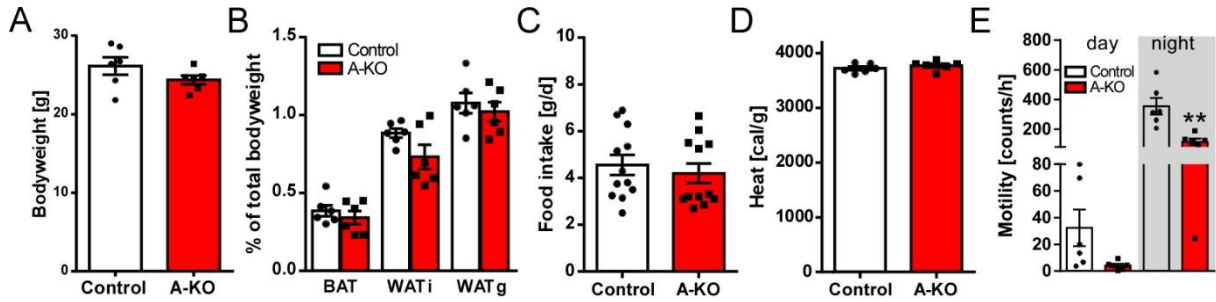
Figure 40 Analysis of 8-week-old male ENT1fl-ApnCre mice
(A) Bodyweight, (B) adipose tissue weights, (C) food intake, (D) energy content of feces and (E) motility of 8-week-old, male ENT1fl-ApnCre mice (A-KO: ENT1$^{fl/fl}$ ApnCre+, Control: ENT1$^{fl/fl}$ ApnCre-). Results are represented as mean ± SEM. t-test, n=6. **p≤0.01

Furthermore, indirect calorimetry of these 8-week-old ENT1-floxed and -A-KO mice was measured using metabolic cages. Oxygen consumption of ENT1-A-KO mice at 23°C was significantly increased (p≤0.05) in comparison to control littermates during day and night cycles (Figure 41A-C). Oxygen consumption of ENT1-A-KO mice during acute cold exposure at 4°C was significantly enhanced at the 78 minutes' time point (Control: 6.63 ± 0.22ml/h/g; ENT1-A-KO: 7.85 ± 0.36ml/h/g) (Figure 41D). AUC values of oxygen consumption of ENT1-A-KO mice over 78 minutes of cold exposure were increased by 8% compared to control mice, albeit this increase was not statistically significant (p=0.1273) (Figure 41E).
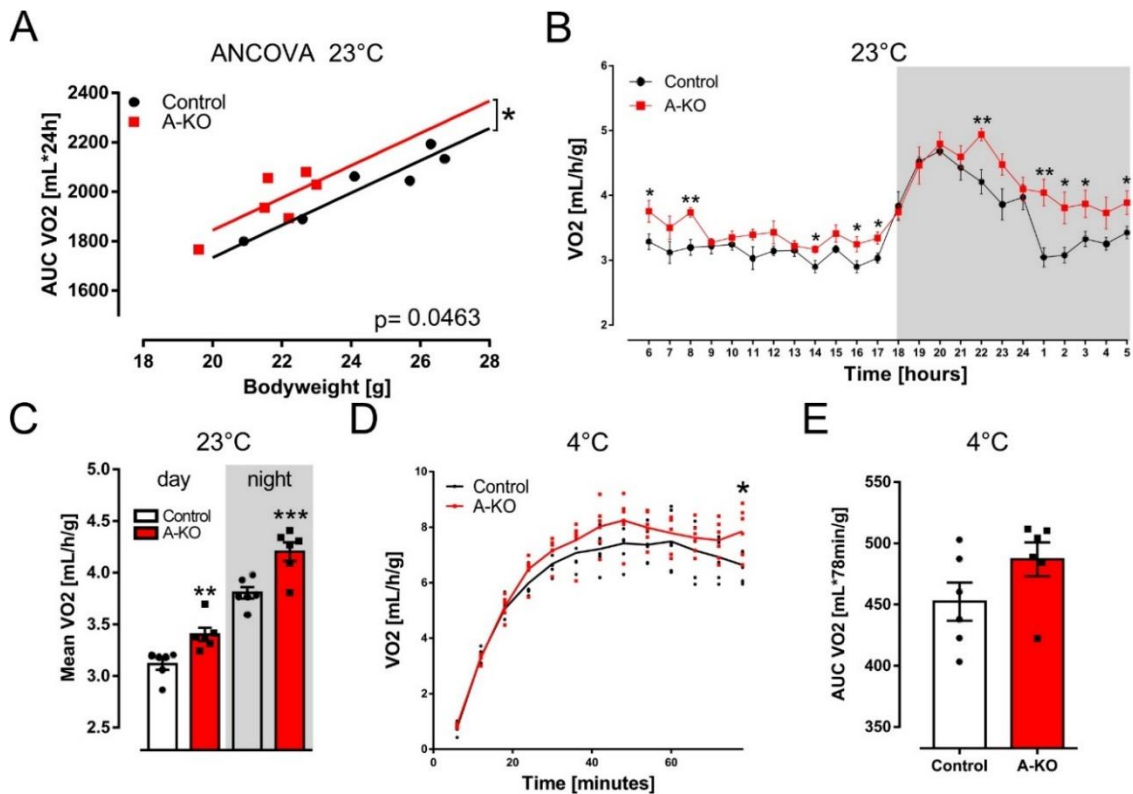
Figure 41 Oxygen consumption of 8-week-old ENT1fl-ApnCre mice
(A) ANCOVA (AUC(VO2) vs. bodyweight), (B) oxygen consumption at 23°C and (C) mean of oxygen consumption at 23°C during day and night cycle (12 hours each), (D) oxygen consumption during acute cold exposure at 4°C, (E) AUC of oxygen consumption during acute cold exposure at 4°C of 8-week-old male ENT1fl-ApnCre mice (A-KO: ENT1$^{fl/fl}$ ApnCre+, Control: ENT1$^{fl/fl}$ ApnCre-). Animals were housed at 23°C and fed a chow diet. Results are represented as mean ± SEM. t-test was applied except for A (ANCOVA). n=6. *p≤0.05, **p≤0.01, ***p≤0.005

qRT-PCR analysis of ATs dissected from these mice revealed significantly elevated mRNA levels of several mitochondrial genes, including *Ucp1*, *Ppargc1a* and *Prdm16*, in BAT of ENT1-A-KO mice compared to ENT1-floxed control littermates (+77%, +76% and +118%, respectively) (Figure 42A-C). Expression levels of the mitochondrial markers *Ndufa1* and *Nd5* were increased in ENT1-A-KO BAT, albeit not significantly (+75% and +19%, p=0.0734 and p=0.0668, respectively) (Figure 42D, E). Expression values of the thermogenic genes *Ucp1* and *Ppargc1a* were enhanced in WATi depots of ENT1-A-KO mice, but not significantly (+280% and +66%, p=0.0874 and p=0.0803, respectively; Figure 42F, G). *Prdm16* expression in WATi was not statistically different between the two genotypes (Figure 42H). In contrast, ENT1-A-KO WATg depots showed increased mRNA expression of *Ucp1* (p≤0.05), even though the measured expression levels of *Ucp1* were low in WATg for both groups (Figure 42I). No significant differences in mRNA expression of the co-transcription factor *Ppargc1a* in WATg were observed between the different genotypes (Figure 42J).
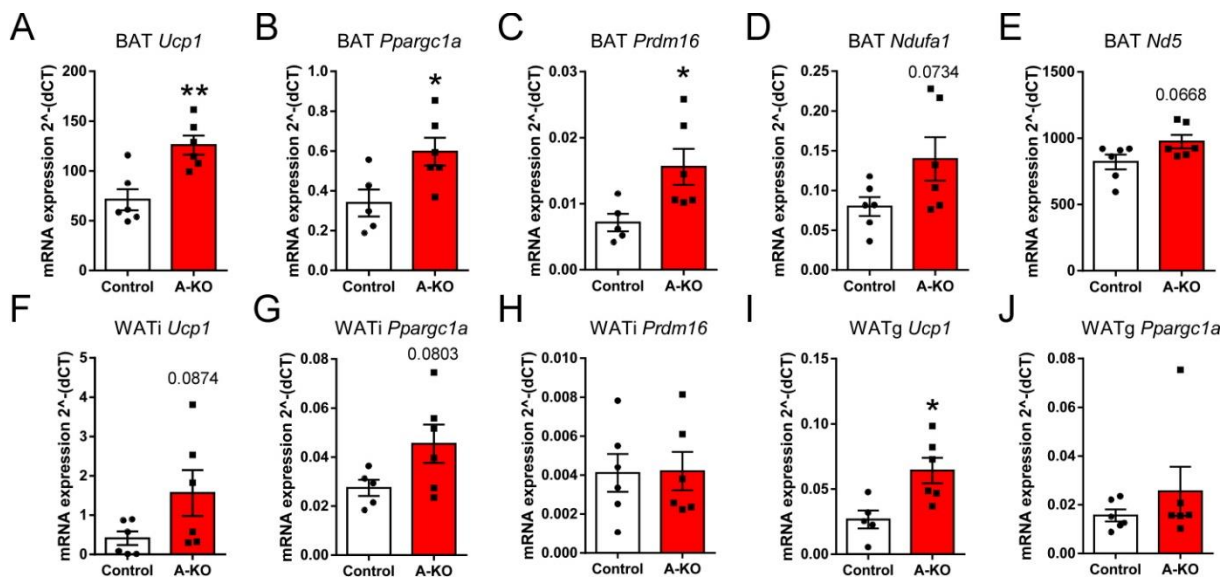
Figure 42 Expression levels of mitochondrial genes in ENT1fl-ApnCre adipose tissues
mRNA expression of the mitochondrial genes (A) *Ucp1*, (B) *Ppargc1a*, (C) *Prdm16*, (D) *Ndufa1* and (E) *Nd5* in BAT; mRNA expression of the mitochondrial genes (F) *Ucp1*, (G) *Ppargc1a*, (H) *Prdm16* in WATi and (I) *Ucp1* and (J) *Ppargc1a* in WATg of 8-week-old ENT1fl-ApnCre mice (A-KO: ENT1^{fl/fl} ApnCre+, Control: ENT1^{fl/fl} ApnCre-). Expression data were normalized to *Hprt* and are represented as mean ± SEM. t-test, n=5-6, *p≤0.05, **p≤0.01

Taken together, adipocyte-specific deletion of ENT1 resulted in promoted BAT thermogenesis and whole body oxygen consumption of 8-week-old mice.

4.4.11. Effects of adipocyte-specific deletion of ENT1 on bodyweight and glucose tolerance under high fat diet

Next, to challenge the ENT1fl-ApnCre mice with DIO, either a HFD or a CD was fed for 12 weeks. During 12 weeks of HFD, ENT1-A-KO animals gained 1.69 ± 1.09g less weight (-13%) in comparison to control littermates, but this difference was not statistically significant (Figure 43A, B). After 12 weeks of HFD, NMR measurements revealed no significant differences in

body composition between the two genotypes (Figure 43C). Tissue weights of ENT1-A-KO WATi and WATg were reduced by 17% and 18%, respectively, albeit these reductions were not statistically significant (Figure 43D).

In addition, glucose tolerance test was performed after CD and HFD. Strikingly, after HFD, an improved glucose tolerance (p≤0.05) was observed in ENT1-A-KO mice compared to control animals (Figure 43E, F). The glucose tolerance of ENT1-A-KO mice was not changed significantly between the CD and HFD groups, while in the ENT1-floxed control groups it was worsened after HFD compared to CD (p≤0.01) (Figure 43F).
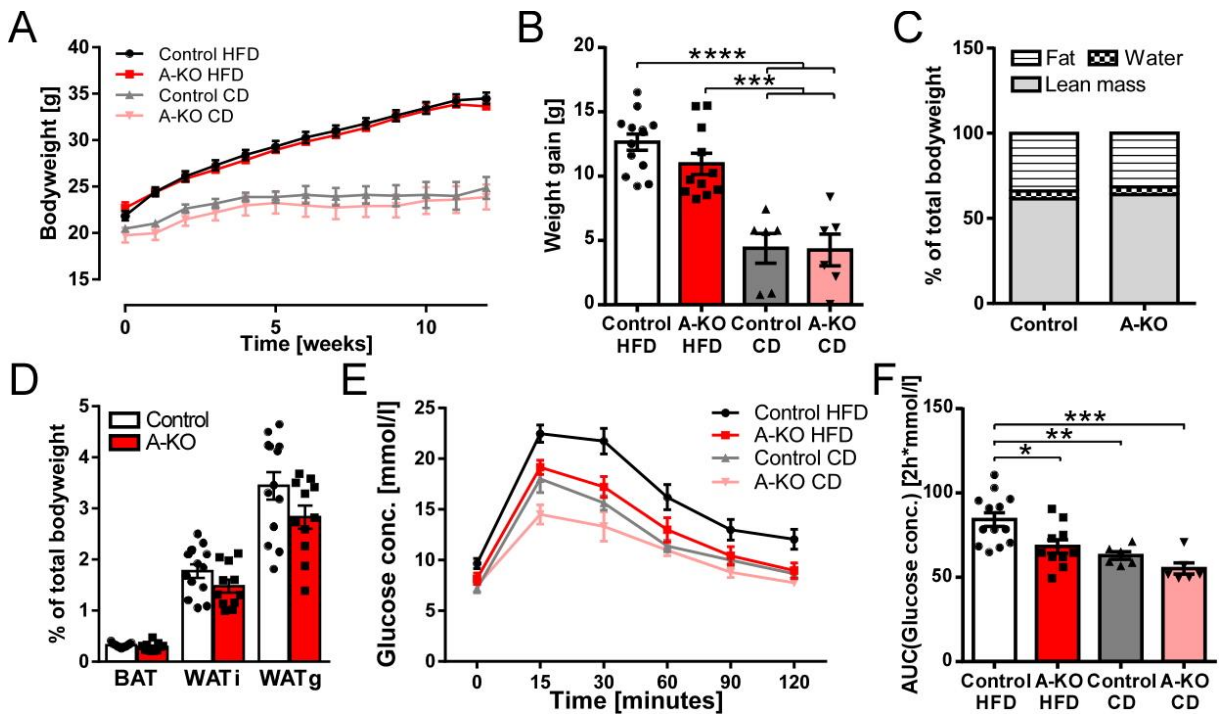
Figure 43 Weight gain and glucose tolerance of ENT1fl-ApnCre mice after HFD or CD
(A) Bodyweight and (B) weight gain of ENT1fl-ApnCre mice (A-KO: ENT1$^{fl/fl}$ ApnCre+, Control: ENT1$^{fl/fl}$ ApnCre-) during 12 weeks of CD or HFD. (C) Body composition and (D) weight of fat pads of ENT1fl-ApnCre mice after 12 weeks of HFD. (E) Glucose tolerance test and (F) respective AUCs of glucose concentrations of ENT1fl-ApnCre mice after 11 weeks of CD or HFD. Results are represented as mean ± SEM. ANOVA was applied for B and F, t-test for C and D. 6 mice per genotype were analyzed for the CD experiment, 13 ENT1-floxed control and 11 ENT1-A-KO mice were challenged with a HFD and analyzed. *p≤0.05, **p≤0.01, ***p≤0.005, ****p≤0.001

In summary, adipocyte-specific KO of ENT1 did not significantly affect weight gain, but resulted in improved glucose tolerance of ENT1-A-KO mice after twelve weeks of HFD.

4.4.12. Energy expenditure of adipocyte-specific ENT1-A-KO mice after high fat diet

ANCOVA showed increased oxygen consumption (p=0.0208) of ENT1-A-KO mice after 12 weeks of HFD as compared to control littermates (Figure 44A). AUC values of oxygen consumption, which was measured for 24 hours, to monitor one full day and night cycle each, revealed significantly elevated oxygen consumption of HFD-fed ENT1-A-KO mice at 23°C compared to control animals (Figure 44B, C). The AUC of V(O$_2$) over 24 hours was significantly

increased by 7% (p≤0.01) in ENT1-A-KO animals (Figure 44C). In contrast, motility, food intake, and intestinal absorption, which was measured *via* bomb calorimetry of feces, were not statistically different between the two genotypes (Figure 44D-F). In order to measure the maximal thermogenic capacity of the ENT1fl-ApnCre mice after HFD, animals were acutely cold-exposed at 4°C and indirect calorimetry was monitored. ENT1-A-KO mice showed improved EE, indicated by higher oxygen consumption, during the first 12 to 18 minutes of cold exposure (Figure 44G). Calculated AUC values of oxygen consumption over 78 minutes of cold exposure showed increased oxygen consumption of ENT1-A-KO mice by 5%, albeit this difference was not statistically significant (p=0.1097) (Figure 44H).
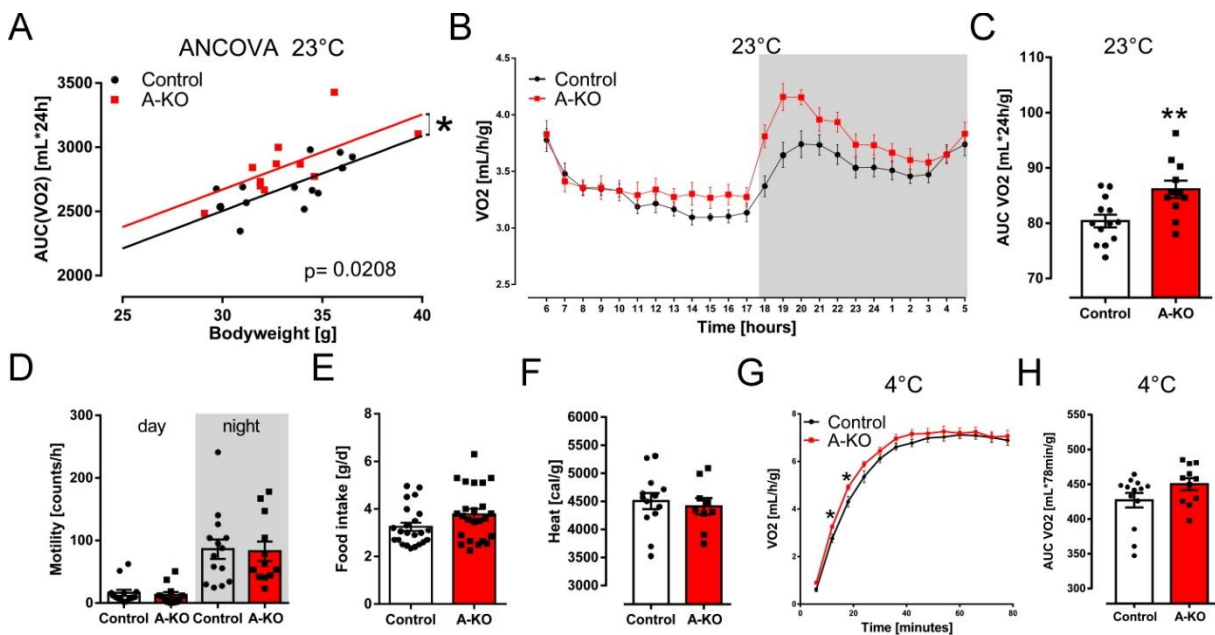
Figure 44 Metabolic characterization of ENT1fl-ApnCre mice after HFD
(A) ANCOVA (AUC(VO2) vs. bodyweight), (B) oxygen consumption, (C) AUC of oxygen consumption, (D) motility during day and night cycle (12 hours each), (E) food intake and (F) energy content of feces of 18-week-old male ENT1fl-ApnCre mice (A-KO: ENT1$^{fl/fl}$ ApnCre+, Control: ENT1$^{fl/fl}$ ApnCre-) at 23°C; after 12 weeks of HFD. (G) Oxygen consumption during acute cold exposure at 4°C, (H) AUC of oxygen consumption during acute cold exposure at 4°C of 18-week-old male ENT1fl-ApnCre mice after 12 weeks of HFD. Results are represented as mean ± SEM. t-test was applied except for A (ANCOVA). 13 ENT1-floxed control and 11 ENT1-A-KO mice were analyzed. *p≤0.05, **p≤0.01

In further experiments the expression of mitochondrial and thermogenic genes was investigated. Western-Blots of BAT of ENT1fl-ApnCre mice after 12 weeks of HFD showed enhanced UCP1 protein expression in BAT of ENT1-A-KO mice (2.37 ± 0.49; p≤0.05) (Figure 45A). In addition, qRT-PCR analysis revealed increased expression of *Ucp1* (+45%; p≤0.01) in ENT1-A-KO BAT after HFD (Figure 45B), while also significantly elevated mRNA expression values of *Ppargc1a* and *Cox8b* (+41% and +48%, respectively) were measured (Figure 45C, D). Statistical tendencies for increased mRNA levels in A-KO-BAT were observed for the mitochondrial genes *Nd5* and *Ndufa1* (+38% and +43%; p=0.0682 and p=0.0577, respectively) (Figure 45E, F). WATi depots, dissected from ENT1-A-KO mice after HFD, showed elevated mRNA expression of the thermogenic genes *Ucp1, Ppargc1a* and *Cox8b* (+336%, +207% and

+128%, respectively; p≤0.05) in comparison to WATi of control animals (Figure 45G-I). In contrast, these differences were not observed in the gonadal WAT (Figure 45J, K).
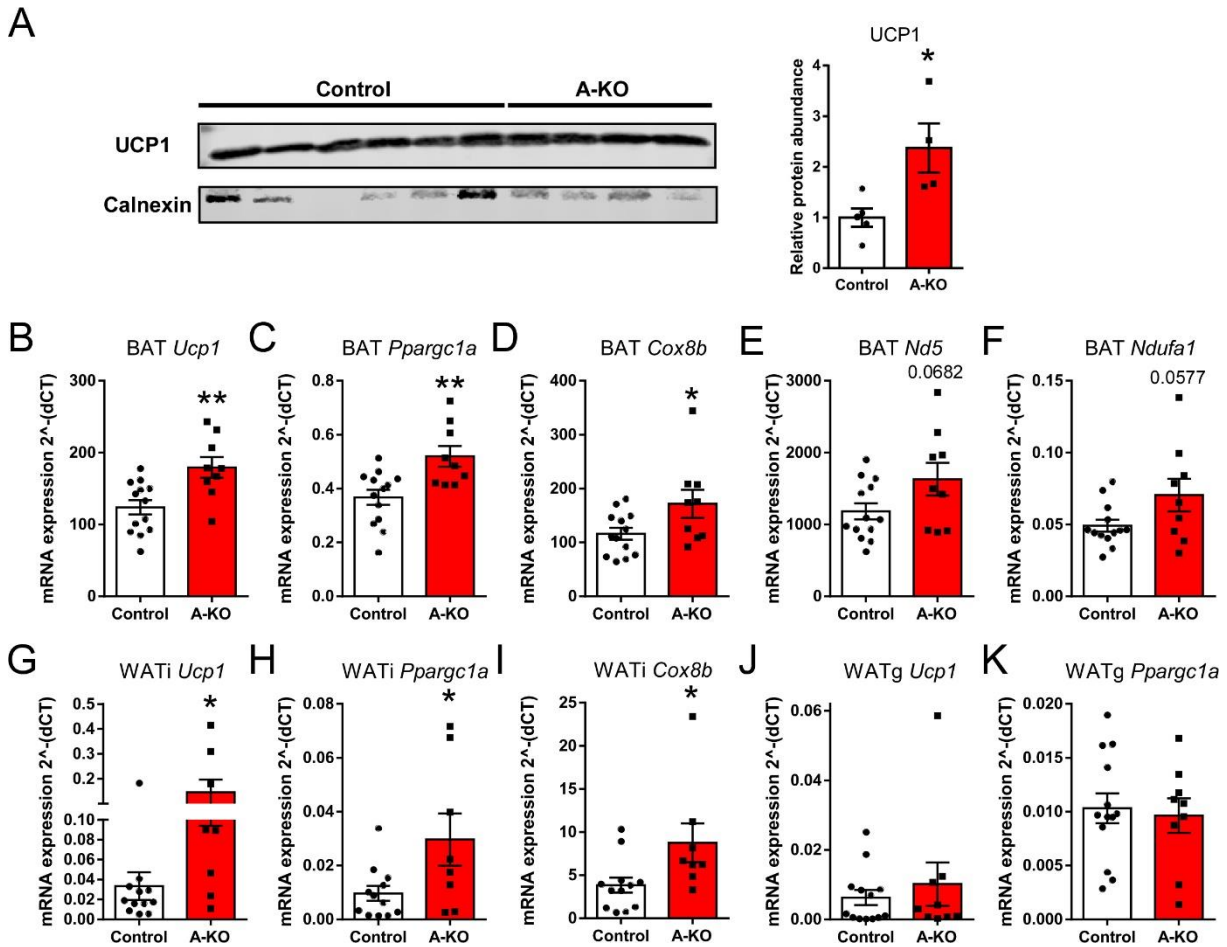
Figure 45 Expression of thermogenic genes in ATs of ENT1fl-ApnCre mice after HFD
(A) Representative Western-Blot and quantification of UCP1 (expression data were normalized to Calnexin) of BAT; mRNA expression of the mitochondrial genes (B) *Ucp1*, (C) *Ppargc1a*, (D) *Cox8b*, (E) *Nd5* and (F) *Ndufa1* in BAT, (G) *Ucp1*; (H) *Ppargc1a* and (I) *Cox8b* in WATi; (J) *Ucp1* and (K) *Ppargc1a* in WATg of ENT1fl-ApnCre mice (A-KO: ENT1^{fl/fl} ApnCre+, Control: ENT1^{fl/fl} ApnCre-) after 12 weeks of HFD. qRT-PCR data were normalized to *Hprt*. Results are represented as mean ± SEM. t-test. n=4-5 for A; B-K: n(Control)=12-13; n(A-KO)=8-9. *p≤0.05, **p≤0.01

Taken together, adipocyte-specific ENT1-A-KO mice showed enhanced EE and increased expression of thermogenic genes in BAT and WATi after 12 weeks of HFD.

4.5. Inosine signaling in adipose tissue *via* AdoRA2B

In order to identify potential signaling pathways of inosine in brown and beige adipocytes another series of experiments was carried out. Inosine has been shown to bind to adenosine receptors (AdoRAs) in other cell types, especially to the A2A-subtype (Gomez and Sitkovsky, 2003; Welihinda et al., 2016; Welihinda et al., 2018). Preliminary data of our working group suggested that inosine signals *via* both, AdoRA2A (A2A) and AdoRA2B (A2B) receptors, in BA, and that the effects mediated by A2B are more pronounced in comparison. Therefore, this target was further investigated.

4.5.1. Effects of inhibition of AdoRA2B on inosine-mediated intracellular cAMP levels in brown adipocytes

Initially, intracellular cAMP levels of BA after inosine treatment (300nM) with pre-incubation in presence or absence of the A2B-antagonist PBS603 (300nM) were measured. Obtained results showed a significant increase in cAMP concentrations of inosine treated cells (+49%; $p \leq 0.05$) compared to controls (Figure 46A). In contrast, this stimulatory effect of inosine was not observed in BA, which were pre-incubated with the A2B-antagonist PSB603 (Figure 46A). A similar pattern of cAMP levels was observed using a genetic model for deletion of A2B: While WT BA responded to 300nM inosine treatment with significantly increased intracellular cAMP concentrations (+8.7 ± 3.6pmol/mg protein; +57%; $p \leq 0.05$), no significant effect was measured in A2B-KO BA (Figure 46B).
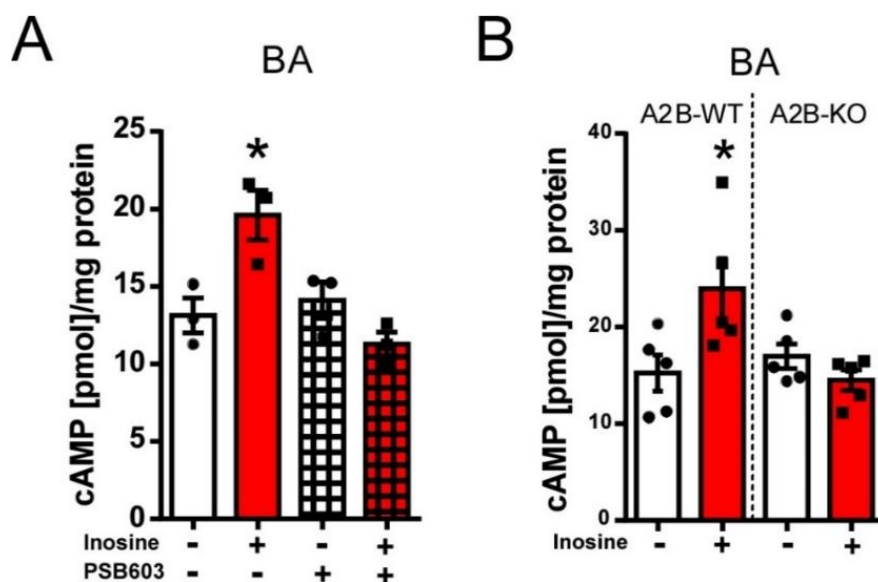
Figure 46 Effect of AdoRA2B-inhibition on inosine-mediated intracellular cAMP concentrations of murine BA

(A) Intracellular cAMP concentrations of murine BA after 15 minutes of incubation with or without 300nM inosine after pre-treatment with vehicle (1%DMSO in PBS) or PSB603 (300nM). (B) Intracellular cAMP concentrations of murine WT and A2B-KO BA after incubation with or without 300nM inosine for 15 minutes. Data were normalized to protein content and are represented as mean ± SEM. ANOVA, A: n=3, B: n=5. *$p \leq 0.05$

Taken together, inhibition of AdoRA2B abolished the stimulatory effect of inosine on intracellular cAMP levels of BA.

4.5.2. Effects of AdoRA2B-deletion on inosine-induced lipolysis in brown and white adipocytes

Next, inosine-induced lipolysis of WT and A2B-KO BA as well as WA was studied. The stimulatory effect of inosine on lipolysis observed in WT BA and WA (+42% and +56%, respectively; $p \leq 0.05$) was absent in A2B-KO adipocytes (Figure 47A, B). In both cell models CL-316243 (1µM) was applied as a positive control, to rule out that the absence of inosine-induced lipolysis is caused by general functional disorders of the A2B-KO adipocytes. This

was not the case, because all cell pools used showed significantly increased lipolysis after incubation with CL-316243 compared to control cells (Figure 47).
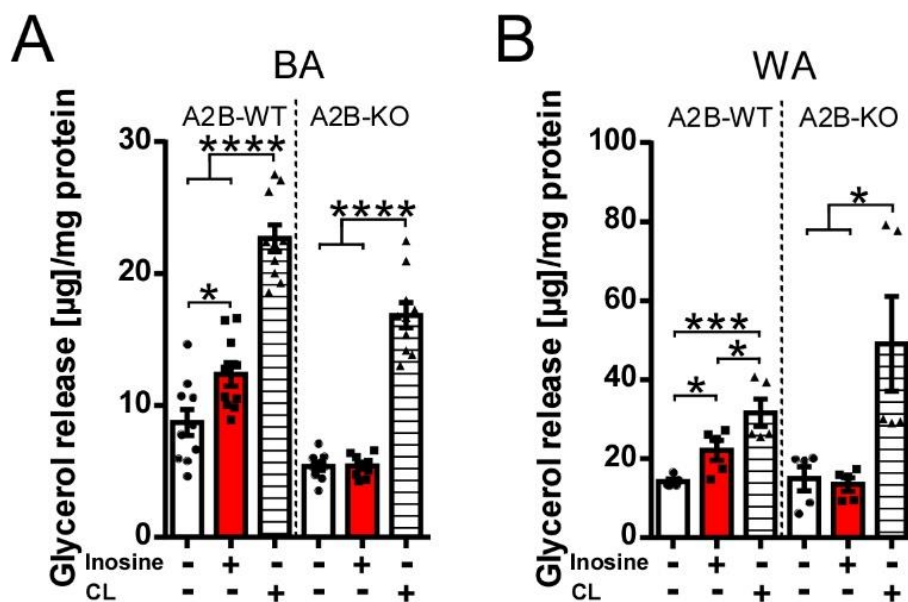
Figure 47 Inosine-induced lipolysis of murine WT and A2B-KO BA and WA
Glycerol release of murine WT and A2B-KO (A) BA and (B) WA after incubation for 120 minutes with PBS (solvent control), 300nM inosine or 1µM CL-316243. Data were normalized to protein content and are represented as mean ± SEM. ANOVA, 10 cell pools of BA and 5 pools of WA were analyzed. *p≤0.05, ***p≤0.005, ****p≤0.001

In summary, deletion of AdoRA2B revoked the stimulatory effect of inosine on lipolysis in BA and WA.

4.5.3. Effects of AdoRA2B-KO on inosine-stimulated *Ucp1* expression of brown and white adipocytes

Previous experiments in this thesis indicated a browning effect of inosine on ATs. Therefore, *Ucp1* mRNA-expression levels, as an indicator of browning, were measured in WT and A2B-KO adipocytes, after 16 hours of stimulation by 300nM inosine. *Ucp1* expression of WT BA was significantly elevated after inosine treatment (+0.86 ± 0.33; p≤0.05), while no significant change was observed in A2B-KO BA (Figure 48A). A significant increase of *Ucp1* expression was also detected in WT WA, after 16 hours of inosine treatment (+212.3 ± 11.4; p≤0.001), indicating browning (Figure 48B). In contrast, *Ucp1* expression levels of A2B-KO WA were not affected significantly by inosine-stimulation (Figure 48B).
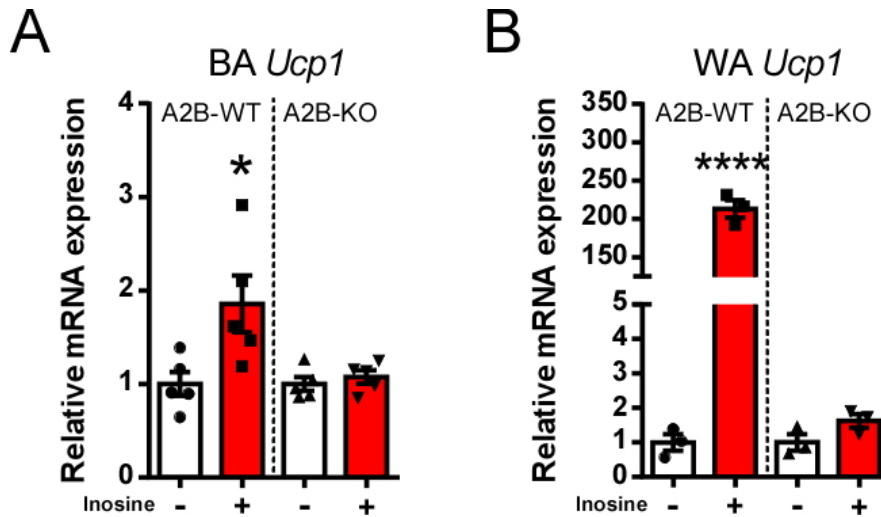
Figure 48 Influence of inosine on UCP1 expression of murine WT and A2B-KO adipocytes
mRNA expression of the thermogenic gene *Ucp1* after 16 hours of treatment with or without 300nM inosine of (A) murine WT and A2B-KO BA and (B) murine WT and A2B-KO WA. qRT-PCR data were normalized to *Hprt*. Results are represented as mean ± SEM. t-test. 5 pools of BA and 3 pools of WA were analyzed. *p≤0.05, ****p≤0.001

Taken together, loss of AdoRA2B abrogated the increase in *Ucp1* expression by inosine-stimulation in BA and WA.

4.5.4. Effects of inosine administration to AdoRA2B-KO mice

In order to confirm the *in vitro* findings *in vivo*, WT and A2B-KO mice were injected with inosine (*i.p.*, 100µg/kg) and oxygen consumption was monitored using metabolic cages. Inosine injections in WT mice resulted in significantly increased (+14%; p≤0.05) oxygen consumption compared to vehicle-injected WT animals indicating enhanced thermogenesis, while this effect was not observed in A2B-KO mice (Figure 49A, B).
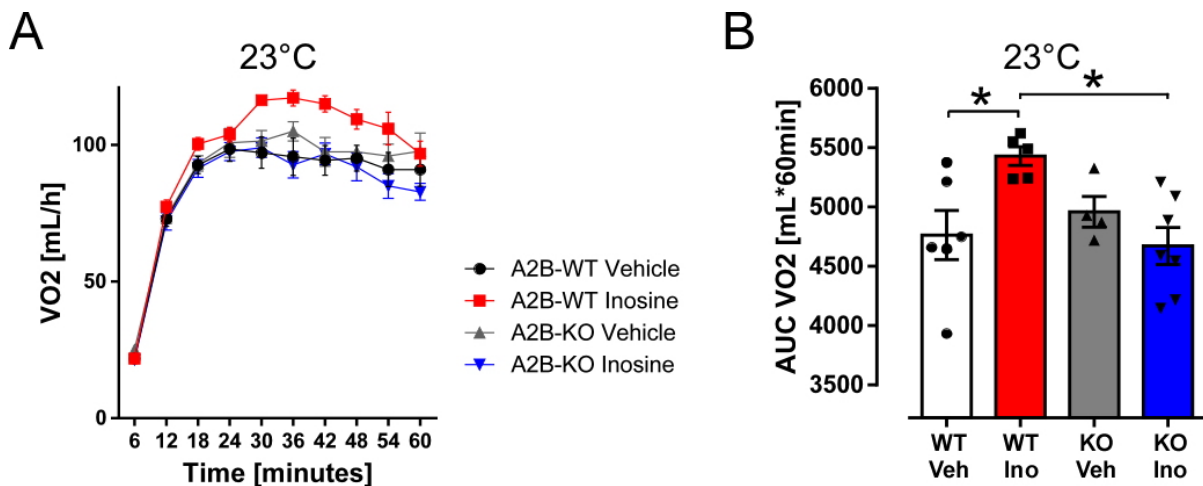
Figure 49 Oxygen consumption of WT and A2B-KO mice after inosine injections
(A) Oxygen consumption at 23°C after *i.p* injection of either NaCl 0.9% (Vehicle, Veh) or 100µg/kg inosine (Ino) (dissolved in NaCl 0.9%) in 8-week-old, male WT and global A2B-KO mice. (B) Respective AUCs of measured V(O$_2$) over 60 minutes. Data are represented as mean ± SEM. ANOVA, n=4-7. *p≤0.05

In summary, deletion of AdoRA2B abolished the stimulatory effects of inosine on oxygen consumption *in vivo* confirming prior *in vitro* findings.

5. Discussion

Obesity has long been recognized as a pandemic and as one of the major public health problems (World Health Organization, 2000). In 2016, more people suffered from overnutrition than from undernutrition (Di Cesare et al., 2016), with over 650 million adults classified as obese (World Health Organization, 2018). The abnormal accumulation of fat is caused by a disturbed energy balance, when calorie intake exceeds energy consumption. Obese individuals have and increased risk to suffer from comorbidities, such as diabetes mellitus type 2, fatty liver disease, cardiac complications and several types of cancer, contributing to reduced quality of life and life expectancy (Blüher, 2019).

The currently approved anti-obesity medications focus primarily on the reduction of calorie intake. Another approach to treat or prevent obesity and its comorbidities is to increase EE. In this context, the discovery of metabolic active BAT in human adults (Nedergaard et al., 2007; Virtanen et al., 2009) revealed a new promising therapeutic target to treat obesity. Upon activation of BAT, UCP1 enables NST, in which energy is consumed and dissipated as heat (Cannon and Nedergaard, 2004). Consequently, stimulation of human BAT increases EE, which can induce a 'melting of white fat depots'. In other studies, it was shown that beige adipocytes, which develop during browning of WAT, also express UCP1 and perform thermogenesis, thereby contributing to improved metabolism and calorie consumption (Barbatelli et al., 2010; Wu et al., 2012).

With regard to the progressing epidemic of obesity and previous findings highlighting the important role of thermogenic active AT in the regulation of metabolic function, novel approaches targeting and activating AT metabolism are of high scientific and therapeutic relevance. This includes the identification of molecules, that mediate increased EE of thermogenic AT.

In this thesis, the role of inosine in adipose tissue metabolism was investigated, focusing on its stimulatory effects on EE of brown and beige AT. In the following sections, the findings are summarized and discussed with respect to the research questions posed in chapter two.

5.1. Extracellular inosine in thermogenic adipose tissue

Since ATP is released by adipocytes during physiological activation (Adamson et al., 2015), an initial screening focused on ATP-derived purinergic molecules, which were quantitatively measured and investigated regarding their influence on BA *in vitro*.

Obtained UPLC data showed that purinergic molecules were present in the extracellular space of BA, under basal conditions and upon sympathetic stimulation. Extracellular inosine and adenosine concentrations of murine BA were significantly increased after 60 minutes of NE-stimulation compared to control values. Increased extracellular inosine concentrations were

also observed in human brown adipocytes after 60 minutes of NE-stimulation. Strikingly, extracellular inosine levels of hBA were significantly higher compared to murine BA and inosine was found to be the most abundant purine in hBA under basal and NE-stimulated conditions. These data suggest a possible role of inosine in human BAT. In order to investigate the differences in inosine concentrations between murine and human BA, expression levels of purine degrading enzymes and nucleoside transporters should be compared.

Inosine treatment (300nM) of BA resulted in significantly increased lipolysis and intracellular cAMP levels, suggesting that the direct metabolite of adenosine plays a stimulatory role in AT metabolism. Interestingly, the maximal effects on intracellular cAMP levels of adipocytes were similar for adenosine and inosine, while comparison of the EC_{50}-values identified adenosine to be the more potent purine in comparison to inosine. Moreover, high extracellular levels of AMP and hypoxanthine were measured in BA under basal and stimulated conditions, but treatment with AMP and hypoxanthine did not affect lipolysis of BA. Consequently, inosine was identified to activate BA metabolism mediating a comparable maximal effect on intracellular cAMP levels as its progenitor molecule adenosine, while hypoxanthine, the direct metabolite of inosine, showed no effects on BA' function.

Comparison of inosine concentrations found in dialysates of BAT and WATi showed that inosine levels were significantly higher in BAT. This finding was in line with recent literature describing higher purine concentrations in murine BA compared to WA (Scheibler, 2017). Interestingly, extracellular inosine concentrations were the most upregulated among the detected purines in BAT after NE-mediated activation and cold exposure. Cold exposure of mice also led to elevated extracellular inosine concentrations of WATi, the white adipose tissue having the highest capacity for browning (Collins et al., 1997; Barbatelli et al., 2010; Seale et al., 2011).

Previous studies revealed that the purine adenosine promotes BAT activation and function (Gnad et al., 2014; Gnad et al., 2020). However, adenosine has been described to be rapidly degraded (Welihinda et al., 2016). Consistent with these findings, the experiments in this thesis showed that adenosine was not the most abundant stimulatory extracellular purinergic molecule in brown adipocytes, but rather inosine accumulated in high concentrations. In addition, extracellular inosine concentrations of thermogenic ATs were increased upon stimulation, indicating that inosine plays a general role in thermogenic AT metabolism. Consequently, inosine might function as an autocrine/paracrine molecule to prolong SNS-signaling within ATs.

These findings outline a general role of inosine in brown and beige AT. While this study focused on ATP-derived purinergic metabolites, future untargeted secretomic screenings are needed to potentially identify further molecules involved in AT metabolism.

In summary, extracellular inosine was detected in thermogenic AT under basal and stimulated conditions. Moreover, extracellular inosine concentrations were increased upon SNS activation and stimulatory effects of inosine on BA were observed. These results indicate that inosine acts as a stimulatory autocrine/paracrine molecule in brown and beige AT.

5.2. Effects of inosine on adipose tissue function and whole body energy expenditure

Following the detection of high extracellular inosine concentrations in thermogenic AT and its observed activating *in vitro* effects, *ex vivo* and *in vivo* effects of inosine on AT function and whole body metabolism were studied.

Preliminary experiments showed that inosine-stimulation promoted *ex vivo* lipolysis and oxygen consumption of BAT and WATi. In the first *in vivo* experiment, acute oral administration of inosine to mice resulted in significantly increased oxygen consumption of the inosine-treated group compared to control animals. Moreover, chronic administration of inosine *in vivo* was investigated by implantation of micro-osmotic pumps in C57Bl6/J mice. Thereby, inosine or control solvent was constantly applied for 28 days. When mice were fed a CD during the experiment, oxygen consumption of the inosine-treated animals at 23°C, was not significantly elevated in comparison to vehicle-treated mice. In contrast, oxygen consumption of inosine-treated mice was significantly increased during acute cold exposure at 4°C, suggesting an enhanced thermogenic potential of ATs. Furthermore, mRNA expression levels of the thermogenic gene *Ucp1* in BAT and the browning marker *Prdm16* in WATi were significantly increased in animals treated with inosine. After 28 days of HFD, in combination with constant inosine application by micro-osmotic pumps, a significantly reduced weight gain of the inosine-treated group compared to control animals was observed. Moreover, oxygen consumption of the inosine-treated mice was significantly increased under both conditions: at 23°C, which means mild cold-exposure for mice, and at 4°C, when the thermogenic capacity is maxed out (Cannon and Nedergaard, 2004; Nedergaard and Cannon, 2014). In summary, chronic inosine treatment of mice increased EE and mitigated DIO.

Further experiments, including qRT-PCR, Western-Blots and histological analysis, showed an enhanced function of BAT after HFD and concomitant inosine treatment, indicated by significantly increased expression of the thermogenic gene *Ucp1* and other mitochondrial markers, such as *Ndufa1* and *Nd5*. In addition, inosine treatment resulted in pronounced browning of WATi, indicated by an increased number of beige cells. In the CD and HFD cohort, browning markers, such as *Prdm16*, were significantly higher expressed in WATi of inosine-treated mice as compared to control animals. Increased thermogenesis resulting from browning of WATi may contribute to the observed improved whole body EE after inosine treatment. In contrast to the WATi depots, no statistically significant differences in mRNA

expression of browning markers between the two treatments were observed in the gonadal WAT depots. These findings are in line with the literature describing brown-like transformation of WAT most prominent in inguinal subcutaneous fat, while gonadal fat is recognized to be less prone to browning (Collins et al., 1997; Guerra et al., 1998; Barbatelli et al., 2010). However, smaller adipocyte size was observed in WATg of inosine-treated mice. This effect might be explained by improved whole body EE mediated by the promoted thermogenic function of BAT and WATi. In accordance with the *ex vivo* analyses of AT samples, inosine-stimulation led to improved thermogenic function of BAT and WATi *in vivo*.

Whereas a potential limitation of the experiments was the application period of only 28 days (maximal application period of the microosmotic pumps), significant effects of inosine treatment after HFD were observed. In fact, measured differences in bodyweight increased over time; significant differences were only detected after 28 days of treatment. A longer application period could potentially increase the effect of inosine on DIO. Nevertheless, the attained findings demonstrate the potential of inosine as a candidate for future pharmacological obesity therapy. Since NST works independent of muscle work, inosine treatment might serve as an approach for obese patients, limited in physical activity. However, it has to be considered that (severely) obese subjects are expected to have reduced size and function of BAT depots (Cypess et al., 2009), limiting the activation of brown adipocytes. In the absence of (sufficient) functional BAT, WATi depots could be stimulated to brown by application of inosine.

Currently, inosine pranobex (delimmun®), a combination of inosine and the immunostimulant dimepranol-4-acetamidobenzoate, is the only approved and therapeutically used inosine-containing medication in Germany (Rote Liste® Service GmbH, 2021). Due to its immune stimulating effects, inosine pranobex is used to treat herpes simplex infections and subacute sclerosing panencephalitis (Kora Healthcare Ltd., 2012). Moreover, inosine was evaluated in clinical trials for multiple sclerosis and Parkinson's disease therapy. A Phase II study about inosine treatment against Parkinson's disease showed that oral administered inosine was generally safe and tolerable, even at doses of up to 3 grams per day over 24 month (Schwarzschild et al., 2014). The risk for cardiovascular side effects was not increased in the inosine treatment group compared to placebo (Schwarzschild et al., 2014). In contrast, it was observed that the risk of 'urate-related crystallopathies' correlates with (increased) urate concentrations in blood or urine. Due to concerns about uric acid stones formation or development of gout, an urine alkalinization protocol was applied during the study, no participant developed gout, but for one participant the development of an uric acid stone was documented. These findings suggest that, on the one hand, the risk of urolithiasis can be adequately managed during inosine treatment. On the other hand, monitoring of urine acidity, serum urate and uric acid crystal formation is recommended to further reduce potential side effects. In another clinical trial for Parkinson's disease, which was conducted in Japan, subjects

received 1g inosine per day for 1 year, over the observation-period no long-term adverse effects were reported (Iwaki et al., 2017) indicating the safety of oral inosine in human studies. However, inosine has not been investigated in the context of obesity in human studies yet.

To further investigate the potential of inosine as an anti-obesity medication, clinical trials investigating the effect of inosine on human AT metabolism and whole body EE are needed. In order to measure the impact of inosine on whole body EE in human subjects, indirect calorimetry could be applied. To study the thermogenic AT-specific effects of inosine, uptake of ^{18}F-fluorodeoxyglucose in BAT after activation by inosine could be monitored *via* PET-CT. In accordance with previous phase II studies, monitoring of uric acid concentrations is needed during (long-term) application of inosine. In addition, contraindications of inosine, including patients with gout, increased uric acid levels, uric acid stones or renal insufficiency, need to be considered and further evaluated.

Taken together, the results indicate that inosine activates thermogenic AT, thereby alleviating DIO. Furthermore, the potential of inosine as a novel compound to treat or prevent obesity was demonstrated. While within this study the beneficial *in vivo* effects of inosine were investigated in mouse models, further (clinical) research is needed to examine the transferability of the findings to humans.

5.3. Effects of global deletion of ENT1 on adipose tissue and whole body metabolism

Motivated by the observed abundance of inosine in the extracellular space of thermogenic AT and the beneficial effects of exogenous inosine on AT metabolism, regulation of endogenous inosine concentrations was investigated. In particular, the experiments focused on the effects of deletion of the nucleoside transporter ENT1 on whole body EE and on the function of BAT and WAT. To study the extent, to which deletion of ENT1 affects endogenous extracellular inosine levels and AT metabolism, *in vitro, ex vivo* and *in vivo* experiments were performed using pharmacological and genetic approaches.

Certain CNTs and ENTs are recognized to transport purines (Guallar et al., 2007). Given the high expression of *Slc29a1* (encoding ENT1) in BA, this transporter was further investigated. In order to study the role of ENT1 in regulation of inosine levels, the transporter was inhibited by dipyridamole as a pharmacological approach, while ENT1-KO BA were investigated as a genetic model. Dipyridamole has been described to enhance extracellular purine concentrations of various cell types including adipocytes (Kather, 1988; Rose et al., 2011; Scheibler, 2017; Alarcón et al., 2020). However, dipyridamole is also recognized to inhibit several targets besides ENT1, such as PDE5 (Gresele et al., 2011). Therefore, a genetic model of ENT1-deletion was needed to differentiate whether the described beneficial effects of dipyridamole on oxygen consumption (Scheibler, 2017) are mediated by inhibition of ENT1 or

other targets. For example, it has been shown that treatment of mice with the PDE5-inhibitor sildenafil resulted in increased EE leading to reduced body weight and fat mass (Ayala et al., 2007). Moreover, extracellular inosine levels can be regulated by enzymatic degradation of adenosine *via* ADA and/or by direct transmembrane transport. In order to investigate inhibition of the transmembrane transport as a possible source of extracellular inosine, uptake of radioactively labelled inosine was additionally measured. Pharmacological inhibition and genetic deletion of ENT1 both resulted in significantly reduced inosine-uptake of BA. Consequently, endogenous inosine accumulated extracellularly. These findings confirm that ENT1 is a relevant regulator of extracellular inosine concentrations of BA and show that inosine is taken up *via* ENT1 into BA.

The salvage pathway is a basic intracellular mechanism; purinergic metabolites, like bases and nucleosides, are reutilized and converted to nucleotides (Zoref-Shani, 1992). This pathway is especially important in cell types that cannot perform *de novo* synthesis or in metabolically highly active cells (Frenguelli, 2019). Therefore, reuptake (e.g. *via* ENT1) of purinergic metabolites, such as inosine, to reutilize them to energetic molecules in form of nucleotides, can be favorable for metabolically active BA, but also terminates the potential extracellular signaling of the purinergic metabolites.

After ENT1 was validated as a transmembrane transporter of inosine in BA, it was further investigated whether the positive effects on ATs' EE observed under administration of exogenous inosine (section 4.2, 5.2) can also be achieved by increasing endogenous inosine concentrations *via* deletion of ENT1. Global ENT1-KO mice and WT littermates were studied to test this hypothesis. Isolated ENT1-KO BA and WA revealed improved differentiation and thermogenic capacity as compared to control cells. This was indicated by improved Oil Red O stainings, significantly elevated mRNA expression of adipogenic and thermogenic genes as well as significantly enhanced basal and uncoupled mitochondrial respiration. Consistent with these results, increased lipolysis and oxygen consumption was measured in BAT and WAT explants. Interestingly, global ENT1-KO mice had significantly less fat mass compared to control animals, while there was neither a statistical difference in intestinal absorption nor in food intake between the two genotypes. In ENT1-KO mice, WATi was found to take up significantly more glucose and fatty acids in comparison to WT animals, while there was also a statistical tendency for ENT1-KO BAT taking up more fatty acids.

Next, WT and global ENT1-KO mice were challenged with a HFD. After 12 weeks of HFD, the ENT1-KO animals gained significantly less weight in comparison to WT littermates. In addition, NMR analysis after HFD showed significantly less fat mass of ENT1-deficient mice, especially the WATg mass was strongly reduced. Moreover, ENT1-KO animals had improved glucose tolerance after 11 weeks of HFD in comparison to control mice, indicating that deletion of ENT1

mitigates development of insulin-resistance during DIO. Furthermore, EE and thermogenic capacity of ENT1-KO mice and WT littermates after HFD challenge were examined using metabolic cages. Significantly increased oxygen consumption of ENT1-KO mice was detected at 23°C. When mice were cold-exposed at 4°C, in order to measure the maximal thermogenic capacity (Nedergaard and Cannon, 2014), oxygen consumption of ENT1-KO animals was also significantly enhanced. In summary, these *in vivo* results indicate that ENT1-deficiency promotes thermogenesis, leading to increased EE and mitigation of DIO.

In addition, the typical 'whitening' effect on BAT during DIO, characterized by an increased number of unilocular white-like adipocytes and reduced expression of UCP1, was observed in WT mice, but not in ENT1-KO animals. Thus, ENT1-KO BAT seemed to be protected from whitening during DIO. Since qRT-PCR analysis showed the highest expression levels of *Slc29a1* in BAT compared to WATi and WATg, the strongest effect in the ENT1-KO mouse model was expected in BAT. This was the case for thermogenic gene expression; mRNA expression levels of the thermogenic marker genes *Ucp1* and *Ppargc1a* were significantly upregulated in BAT of global ENT1-KO mice in comparison to WT littermates after HFD. In contrast, no significant differences in thermogenic gene expression between the two genotypes were observed in the white adipose tissues WATi and WATg. However, increased levels of UCP1 protein were detected in the WATi depots of ENT1-KO mice by immunohistochemical stainings. Furthermore, after HFD, the size of adipocytes in WATi and WATg of ENT1-deficient mice was significantly smaller as compared to WT littermates. This can be explained by the enhanced energy consumption of thermogenic AT in ENT1-KO mice leading to less overflow of energetic substrates as fatty acids, which are stored in fat depots. Consequently, less white fat mass accumulates and expansion of ENT1-KO WA is reduced. In summary, the results of *ex vivo* analyses of AT samples are consistent with the observed improved metabolic phenotype of global ENT1-KO mice. In particular, it was shown that global deletion of ENT1 increased thermogenesis of brown and beige adipocytes.

When drawing conclusions from the results of the *in vivo* experiments, it has to be considered that the findings in WT and ENT1-KO mice are based on studying male, 6- to 18-week-old animals. In addition, the effects of ENT1-deletion in ATs were studied using a global ENT1-KO mouse model. In future experiments, inclusion of female subjects and other age-groups is advisable to improve the external validity. To specify the contribution of ENT1-KO AT metabolism to the measured whole body effects, and to rule out that AT metabolism is influenced by ENT1-deletion in other organs, an adipocyte-specific ENT1-KO model was investigated in further experiments.

Recently the ENT1-inhibitor dipyridamole has been described to enhance oxygen consumption of mice (Scheibler, 2017). However, the effect was only detectable in combination with strong

sympathetic stimulation (seven days of cold exposure at 4°C) and potential underlying mechanism, such as thermogenic gene expression of ATs, as well as effects during DIO were not further examined. The data obtained from the analyses of global ENT1-KO mice of this thesis were in accordance with the effect observed after dipyridamole administration to WT mice. Strikingly, using the genetic ENT1-KO model significantly increased oxygen consumption of ENT1-KO mice was already observed at 23°C, which is a mild cold stimulus for mice (Nedergaard and Cannon, 2014). Importantly, reduced weigh gain of ENT1-KO mice during DIO was observed underlining the potential of ENT1 as a target for future obesity therapies.

In order to utilize the beneficial effects of increased endogenous extracellular inosine concentrations by inhibition of ENT1 to potentially treat or prevent obesity of human patients, pharmacological tools or compounds inhibiting ENT1 need to be developed. Dipyridamole is described as a potent inhibitor of ENTs and therapeutically used as an antiplatelet agent in combination with acetylsalicylic acid after stroke or transient ischemic attack (Hills and Johnston, 2008; Wang et al., 2021). However, it has to be considered that this drug is not suitable for patients with heart failure, bleeding disorders or low blood pressure (Boehringer Ingelheim, 2015). Moreover, dipyridamole is known as a 'dirty drug', due to acting on different targets, including PDE5 (Gresele et al., 2011). With regard to the described properties of dipyridamole, development of selective ENT1-inhibitors is needed to limit systemic side effects and to ensure a positive benefit-risk-ratio for potential future overweight or obese patients.

In conclusion, increasing endogenous extracellular inosine concentrations of adipocytes by deletion of ENT1 enhanced thermogenic AT metabolism, which was characterized by increased EE and reduced weight gain during DIO. These findings suggest that ENT1 is a promising target for future obesity therapies, while selective compounds need to be developed. Moreover, effects of ENT1-inhibition on human subjects need to be investigated in the context of AT metabolism.

5.4. Effects of adipocyte-specific deletion of ENT1 on adipose tissue and whole body metabolism

In further experiments it was investigated, to what extent ENT1-deletion in adipocytes affects whole body EE and AT metabolism. To address this question, an adipocyte-specific ENT1-A-KO mouse model (ENT1floxed-AdiponectinCre) was generated and analyzed. A KD efficiency of 48%, 57% and 23% for *Slc29a1* was measured in ENT1-A-KO BAT, WATi and WATg, respectively. BAT and WATi explants of ENT1-A-KO mice showed an improved metabolic function, which was indicated by significantly increased lipolysis and oxygen consumption in comparison to ENT1-floxed control tissues. These findings were in line with the results of the global ENT1-KO model. Mature, primary adipocytes isolated from ENT1-A-KO BAT and WATi

showed significantly increased mRNA expression of adipogenic and thermogenic genes as compared to control adipocytes, suggesting improved differentiation and thermogenic function of ENT1-A-KO cells. In contrast, no statistically significant differences in lipolysis of WATg samples were observed between the two genotypes. Whereas this result differs from the effect on lipolysis observed in WATg of global ENT1-KO mice, the diminished effect can to some extend be explained by the recombination rate of only 23% in ENT1-A-KO WATg.

Analysis of 8-week-old ENT1-A-KO mice showed significantly increased whole body oxygen consumption at 23°C in comparison to control littermates, suggesting improved EE of the adipocyte-specific ENT1-A-KO mice. In accordance with the previously described findings, significantly elevated mRNA expression of the thermogenic gene *Ucp1* was measured in ENT1-A-KO BAT. During 12 weeks of HFD, ENT1-A-KO animals gained 13% less weight compared to control littermates, but this difference was not statistically significant. Moreover, the effect was weaker than the 38% reduction in weight gain observed in the global ENT1-KO mouse model. In NMR measurements and analysis of AT weights after HFD, no significant differences in fat mass were found between ENT1-A-KO animals and control littermates. These diminished effects, in comparison to the global ENT1-KO model, can to some extend be explained by the limited KD efficiency of ~50% in BAT and WATi for *Slc29a1* of the ENT1-A-KO mice.

Interestingly, ENT1-A-KO mice showed improved glucose tolerance in comparison to control mice, after HFD challenge. In addition, after 12 weeks of HFD, oxygen consumption of ENT1-A-KO animals at 23°C was significantly increased, indicating elevated EE. However, while the mean of oxygen consumption of ENT1-A-KO mice was enhanced significantly during the first 12 to 18 minutes of acute cold exposure, the AUC of oxygen consumption over 78 minutes of cold exposure at 4°C did not differ significantly between the genotypes. Matching with the metabolic phenotype after HFD, expression of UCP1 in ENT1-A-KO BAT, as well as mRNA expression of the thermogenic genes *Ucp1* and *Ppargc1a* in ENT1-A-KO WATi, were significantly elevated.

Considering a KD efficiency for *Slc29a1* of ~50% in BAT and WATi as a limiting factor, the observed *in vivo* effects of ENT1-A-KO on EE and glucose tolerance emphasize the role of ENT1 in regulation of extracellular inosine concentrations and AT metabolism. Future investigation of further adipocyte-specific ENT1-KO models, which aim for higher recombination rates in ATs compared to the ENT1floxed-AdiponectinCre model, could potentially exhibit more pronounced AT-mediated metabolic effects. An ENT1floxed-UCP1Cre mouse model enabling deletion of ENT1 in *Ucp1*-expressing cells, could be a promising approach, because the strongest effects of inosine-stimulation and the highest expression of *Slc29a1* were measured in *Ucp1*-expressing brown and beige adipocytes.

Taken together, adipocyte-specific deletion of ENT1 in mice increased whole body EE and promoted thermogenic function of BAT and WATi. These findings suggest that deletion of ENT1 in adipocytes, which in turn increases extracellular inosine concentrations and improves EE of BAT and WATi, mediates increased whole body EE observed in the global ENT1-KO model (section 5.3). In contrast, reduced weight gain and fat mass accumulation during DIO, which were detected as further metabolic effects in the global ENT1-KO model, were not reproducible using the ENT1floxed-AdiponectinCre model. Most likely, the limiting factor was the recombination rate of ~50% in BAT and WATi of ENT1-A-KO mice. Therefore, future experiments studying different Cre-models with higher recombination-rates in ATs, especially in brown and beige adipocytes, are needed to enable a complete reproduction of the effects observed in the global ENT1-KO mice.

5.5. AdoRA2B-dependent inosine signaling in adipose tissue

After inosine has been found to be an activator of adipose tissue EE, potential targets and signaling pathways were investigated. Previous experiments in this thesis showed increased intracellular cAMP concentrations upon inosine-stimulation. Consequently, further experiments focused on G_s-coupled receptors. In particular, the AdoRA2B was examined, because preliminary experiments showed a high relevance of this AdoR for inosine effects on BA. In order to validate the AdoRA2B-mediated effects of inosine in AT, pharmacological and genetic approaches were utilized *in vitro* and *in vivo*.

So far, no specific receptor, especially in AT, has been described for inosine. Several studies showed that inosine might exert anti-inflammatory, neuroprotective, immunomodulatory and anti-depressant effects *via* AdoRA1, AdoRA2A or AdoRA3 in the liver, brain or spleen (Gomez and Sitkovsky, 2003; Haskó et al., 2004; Kaster et al., 2013; Welihinda et al., 2018). Welihinda et al. (2016) showed that inosine acts as a functional agonist on the AdoRA2A, increasing intracellular cAMP concentrations, but not as potent as adenosine. The authors hypothesized that the effect of inosine *via* AdoRA2A, might be reduced due to structural differences of the two molecules and that inosine, as the more stable metabolite of adenosine, could prolong AdoRA2A activation.

Preliminary data of our working group showed that a pre-treatment of BA with an AdoRA2A and/or AdoRA2B antagonist diminished inosine-induced lipolysis. These findings were surprising since the AdoRA2 receptors, especially AdoRA2B, have been described to be rather insensitive to the ligand inosine compared to adenosine (Welihinda et al., 2016; Welihinda et al., 2018). A possible explanation might be that AdoRA2B receptors can form heteromers (Gnad et al., 2020). Potentially, these heteromeric receptors interact more strongly with inosine than single receptors. Moreover, inosine might be an allosteric modulator of AdoRs.

Discussion

In order to study AdoRA2B-mediated effects of inosine, intracellular cAMP concentrations were measured after inosine-stimulation of BA, including pre-incubation in absence or presence of the AdoRA2B-selective antagonist PSB603. In BA, which were not pre-incubated with PSB603, inosine treatment resulted in significantly increased cAMP levels. This stimulatory effect of inosine was abrogated in BA, which were pre-incubated with the A2B antagonist, indicating that inosine effects on BA are AdoRA2B-mediated by G_s-coupled downstream signaling.

This pharmacological approach was supported by further experiments studying WT and A2B-KO BA as a genetic model. A significant inosine-induced increase in intracellular cAMP was measured in WT BA, but not in A2B-KO cells. Moreover, inosine-induced lipolysis, a downstream mechanism of cAMP, was observed in WT BA and WA, while this effect was abolished in A2B-KO adipocytes. In addition, 16 hours of inosine application resulted in significantly increased mRNA expression of *Ucp1* in WT BA and WA, but no statistically significant effects were measured in A2B-deficient cells.

Lastly, as an *in vivo* experiment, inosine was injected in WT and A2B-KO mice. Inosine application to WT mice resulted in significantly increased oxygen consumption at 23°C indicating increased EE. In contrast, no statistically significant difference in oxygen consumption of vehicle- and inosine-injected A2B-KO animals was measured. These results were in line with the previous *in vitro* findings and indicate that inosine mediates its effects in AT *via* G_s-coupled AdoRA2B-dependent signaling, thereby enhancing EE.

Since the inosine-induced effects were completely abrogated in AdoRA2B-KO mice and adipocytes, AdoRA2A, another G_s-coupled potential receptor for inosine, was not further studied in this thesis. However, it was recently shown that the A2B receptor can form heteromers and might be necessary for the conformation of the adenosine binding site as well as the downstream cAMP-signalosome of the A2A receptor in primary adipocytes (Gnad et al., 2020). Moreover, inosine and adenosine have been postulated to share a binding site in AdoRA2A (Welihinda et al., 2016). Thus, the described dependency might also affect inosine signaling. With regard to this potential influence, inosine application should also be studied and compared in A2A-KO and A2A-A2B-double-KO models, in order to specify the direct effects of inosine mediated *via* AdoRA2B and AdoRA2A as well as the indirect effects of AdoRA2B-deletion on AdoRA2A signaling.

In conclusion, G_s-coupled AdoRA2B-dependent signaling was identified as a so far unknown signaling cascade of inosine in adipocytes. Due to the scarcity of obesity therapies targeting thermogenic AT metabolism, this result is of high relevance for the potential development of future drugs targeting thermogenic AT.

6. References

Abbracchio, M.P., and Burnstock, G. (1994). Purinoceptors: Are there families of P2X and P2Y purinoceptors? Pharmacology & therapeutics *64*, 445-475. https://doi.org/10.1016/0163-7258(94)00048-4.

Adamson, S.E., Meher, A.K., Chiu, Y.-H., Sandilos, J.K., Oberholtzer, N.P., Walker, N.N., Hargett, S.R., Seaman, S.A., Peirce-Cottler, S.M., and Isakson, B.E., et al. (2015). Pannexin 1 is required for full activation of insulin-stimulated glucose uptake in adipocytes. Molecular metabolism *4*, 610-618. https://doi.org/10.1016/j.molmet.2015.06.009.

Agilent Technologies, Inc. (2019). Agilent Seahorse XFp Cell Mito Stress Test Kit. User Guide (Wilmington, DE, USA).

Alarcón, S., Toro, María de Los Ángeles, Villarreal, C., Melo, R., Fernández, R., Ayuso Sacido, A., Uribe, D., San Martín, R., and Quezada, C. (2020). Decreased Equilibrative Nucleoside Transporter 1 (ENT1) Activity Contributes to the High Extracellular Adenosine Levels in Mesenchymal Glioblastoma Stem-Like Cells. Cells *9*, 1914. https://doi.org/10.3390/cells9081914.

Ayala, J.E., Bracy, D.P., Julien, B.M., Rottman, J.N., Fueger, P.T., and Wasserman, D.H. (2007). Chronic treatment with sildenafil improves energy balance and insulin action in high fat-fed conscious mice. Diabetes *56*, 1025-1033. https://doi.org/10.2337/db06-0883.

Aymerich, I., Foufelle, F., Ferré, P., Casado, F.J., and Pastor-Anglada, M. (2006). Extracellular adenosine activates AMP-dependent protein kinase (AMPK). Journal of Cell Science *119*, 1612. https://doi.org/10.1242/jcs.02865.

Baldwin, S.A., Beal, P.R., Yao, S.Y.M., King, A.E., Cass, C.E., and Young, J.D. (2004). The equilibrative nucleoside transporter family, SLC29. Pflugers Archiv : European journal of physiology *447*, 735-743. https://doi.org/10.1007/s00424-003-1103-2.

Baldwin, S.A., Yao, S.Y.M., Hyde, R.J., Ng, A.M.L., Foppolo, S., Barnes, K., Ritzel, M.W.L., Cass, C.E., and Young, J.D. (2005). Functional characterization of novel human and mouse equilibrative nucleoside transporters (hENT3 and mENT3) located in intracellular membranes. The Journal of biological chemistry *280*, 15880-15887. https://doi.org/10.1074/jbc.M414337200.

Barbatelli, G., Murano, I., Madsen, L., Hao, Q., Jimenez, M., Kristiansen, K., Giacobino, J.P., Matteis, R. de, and Cinti, S. (2010). The emergence of cold-induced brown adipocytes in mouse white fat depots is determined predominantly by white to brown adipocyte transdifferentiation. American journal of physiology. Endocrinology and metabolism *298*, E1244-53. https://doi.org/10.1152/ajpendo.00600.2009.

References

Barnes, K., Dobrzynski, H., Foppolo, S., Beal, P.R., Ismat, F., Scullion, E.R., Sun, L., Tellez, J., Ritzel, M.W.L., and Claycomb, W.C., et al. (2006). Distribution and functional characterization of equilibrative nucleoside transporter-4, a novel cardiac adenosine transporter activated at acidic pH. Circulation Research *99*, 510-519. https://doi.org/10.1161/01.RES.0000238359.18495.42.

Bartelt, A., Bruns, O.T., Reimer, R., Hohenberg, H., Ittrich, H., Peldschus, K., Kaul, M.G., Tromsdorf, U.I., Weller, H., and Waurisch, C., et al. (2011). Brown adipose tissue activity controls triglyceride clearance. Nature medicine *17*, 200-205. https://doi.org/10.1038/nm.2297.

Birsoy, K., Berry, R., Wang, T., Ceyhan, O., Tavazoie, S., Friedman, J.M., and Rodeheffer, M.S. (2011). Analysis of gene networks in white adipose tissue development reveals a role for ETS2 in adipogenesis. Development *138*, 4709-4719. https://doi.org/10.1242/dev.067710.

Blüher, M. (2019). Obesity: global epidemiology and pathogenesis. Nature reviews. Endocrinology *15*, 288-298. https://doi.org/10.1038/s41574-019-0176-8.

Boehringer Ingelheim (2015). Fachinformation Aggrenox® 200mg/25mg Retardkapseln.

Boison, D. (2013). Adenosine kinase: exploitation for therapeutic gain. Pharmacol Rev *65*, 906-943. https://doi.org/10.1124/pr.112.006361.

Braun, K., Oeckl, J., Westermeier, J., Li, Y., and Klingenspor, M. (2018). Non-adrenergic control of lipolysis and thermogenesis in adipose tissues. The Journal of experimental biology *221*. https://doi.org/10.1242/jeb.165381.

Burnstock, G. (1978). A basis for distinguishing two types of purinergic receptor. In Cell membrane receptors for drugs and hormones: a multidisciplinary approach, R.W. Straub and L. Bolis, eds. (New York: Raven Press), pp. 107–118.

Burnstock, G. (2007). Purine and pyrimidine receptors. Cellular and molecular life sciences : CMLS *64*, 1471-1483. https://doi.org/10.1007/s00018-007-6497-0.

Burnstock, G., and Gentile, D. (2018). The involvement of purinergic signalling in obesity. Purinergic signalling *14*, 97-108. https://doi.org/10.1007/s11302-018-9605-8.

Cannon, B., and Nedergaard, J. (2004). Brown adipose tissue: function and physiological significance. Physiological reviews *84*, 277-359. https://doi.org/10.1152/physrev.00015.2003.

Cao, W., Daniel, K.W., Robidoux, J., Puigserver, P., Medvedev, A.V., Bai, X., Floering, L.M., Spiegelman, B.M., and Collins, S. (2004). p38 mitogen-activated protein kinase is the central regulator of cyclic AMP-dependent transcription of the brown fat uncoupling protein 1 gene. Molecular and cellular biology *24*, 3057-3067. https://doi.org/10.1128/mcb.24.7.3057-3067.2004.

References

Choe, S.S., Huh, J.Y., Hwang, I.J., Kim, J. in, and Kim, J.B. (2016). Adipose Tissue Remodeling: Its Role in Energy Metabolism and Metabolic Disorders. Frontiers in endocrinology *7*, 30. https://doi.org/10.3389/fendo.2016.00030.

Choi, D.-S., Cascini, M.-G., Mailliard, W., Young, H., Paredes, P., McMahon, T., Diamond, I., Bonci, A., and Messing, R.O. (2004). The type 1 equilibrative nucleoside transporter regulates ethanol intoxication and preference. Nature neuroscience *7*, 855-861. https://doi.org/10.1038/nn1288.

Cinti, S. (2002). Adipocyte differentiation and transdifferentiation: plasticity of the adipose organ. Journal of endocrinological investigation *25*, 823-835. https://doi.org/10.1007/BF03344046.

Cinti, S. (2009). Transdifferentiation properties of adipocytes in the adipose organ. American journal of physiology. Endocrinology and metabolism *297*, E977-86. https://doi.org/10.1152/ajpendo.00183.2009.

Cohen, P., Levy, J.D., Zhang, Y., Frontini, A., Kolodin, D.P., Svensson, K.J., Lo, J.C., Zeng, X., Ye, L., and Khandekar, M.J., et al. (2014). Ablation of PRDM16 and beige adipose causes metabolic dysfunction and a subcutaneous to visceral fat switch. Cell *156*, 304-316. https://doi.org/10.1016/j.cell.2013.12.021.

Cohen, P., and Spiegelman, B.M. (2016). Cell biology of fat storage. Molecular biology of the cell *27*, 2523-2527. https://doi.org/10.1091/mbc.E15-10-0749.

Collins, S., Daniel, K.W., Petro, A.E., and Surwit, R.S. (1997). Strain-specific response to beta 3-adrenergic receptor agonist treatment of diet-induced obesity in mice. Endocrinology *138*, 405-413. https://doi.org/10.1210/endo.138.1.4829.

Csóka, B., Németh, Z.H., Virág, L., Gergely, P., Leibovich, S.J., Pacher, P., Sun, C.-X., Blackburn, M.R., Vizi, E.S., and Deitch, E.A., et al. (2007). A2A adenosine receptors and C/EBPbeta are crucially required for IL-10 production by macrophages exposed to Escherichia coli. Blood *110*, 2685-2695. https://doi.org/10.1182/blood-2007-01-065870.

Cypess, A.M., and Kahn, C.R. (2010). Brown fat as a therapy for obesity and diabetes. Current opinion in endocrinology, diabetes, and obesity *17*, 143-149. https://doi.org/10.1097/MED.0b013e328337a81f.

Cypess, A.M., Lehman, S., Williams, G., Tal, I., Rodman, D., Goldfine, A.B., Kuo, F.C., Palmer, E.L., Tseng, Y.-H., and Doria, A., et al. (2009). Identification and importance of brown adipose tissue in adult humans. The New England journal of medicine *360*, 1509-1517. https://doi.org/10.1056/NEJMoa0810780.

References

Cypess, A.M., Weiner, L.S., Roberts-Toler, C., Franquet Elía, E., Kessler, S.H., Kahn, P.A., English, J., Chatman, K., Trauger, S.A., and Doria, A., et al. (2015). Activation of human brown adipose tissue by a β3-adrenergic receptor agonist. Cell metabolism *21*, 33-38. https://doi.org/10.1016/j.cmet.2014.12.009.

Da Rocha Lapa, F., Macedo-Júnior, S.J., Luiz Cerutti, M., and Santos, A.R.S. (2014). Pharmacology of Adenosine Receptors and Their Signaling Role in Immunity and Inflammation. In Pharmacology and Therapeutics, S.J.T. Gowder, ed. (Rijeka: InTech).

Després, J.-P. (2006). Is visceral obesity the cause of the metabolic syndrome? Annals of medicine *38*, 52-63. https://doi.org/10.1080/07853890500383895.

Després, J.-P., Nadeau, A., Tremblay, A., Ferland, M., Moorjani, S., Lupien, P.J., Thériault, G., Pinault, S., and Bouchard, C. (1989). Role of Deep Abdominal Fat in the Association Between Regional Adipose Tissue Distribution and Glucose Tolerance in Obese Women. Diabetes *38*, 304. https://doi.org/10.2337/diab.38.3.304.

Di Cesare, M., Bentham, J., Stevens, G.A., Zhou, B., Danaei, G., Lu, Y., Bixby, H., Cowan, M.J., Riley, L.M., and Hajifathalian, K., et al. (2016). Trends in adult body-mass index in 200 countries from 1975 to 2014: a pooled analysis of 1698 population-based measurement studies with 19·2 million participants. The Lancet *387*, 1377-1396. https://doi.org/10.1016/S0140-6736(16)30054-X.

Dosch, M., Gerber, J., Jebbawi, F., and Beldi, G. (2018). Mechanisms of ATP Release by Inflammatory Cells. International journal of molecular sciences *19*. https://doi.org/10.3390/ijms19041222.

Dubyak, G.R. (1991). Signal transduction by P2-purinergic receptors for extracellular ATP. American journal of respiratory cell and molecular biology *4*, 295-300. https://doi.org/10.1165/ajrcmb/4.4.295.

Eltzschig, H.K., Eckle, T., Mager, A., Küper, N., Karcher, C., Weissmüller, T., Boengler, K., Schulz, R., Robson, S.C., and Colgan, S.P. (2006). ATP Release From Activated Neutrophils Occurs via Connexin 43 and Modulates Adenosine-Dependent Endothelial Cell Function. Circulation Research *99*, 1100-1108. https://doi.org/10.1161/01.RES.0000250174.31269.70.

Fredholm, B.B., IJzerman, A.P., Jacobson, K.A., Linden, J., and Müller, C.E. (2011). International Union of Basic and Clinical Pharmacology. LXXXI. Nomenclature and classification of adenosine receptors--an update. Pharmacol Rev *63*, 1-34. https://doi.org/10.1124/pr.110.003285.

Fredholm, B.B., Irenius, E., Kull, B., and Schulte, G. (2001). Comparison of the potency of adenosine as an agonist at human adenosine receptors expressed in Chinese hamster ovary cells11Abbreviations: cAMP, cyclic adenosine 3′,5′-monophosphate; CHO, Chinese hamster

ovary; NBMPR, nitrobenzylthioinosine; and NECA, 5′-N-ethyl carboxamido adenosine. Biochemical Pharmacology *61*, 443-448. https://doi.org/10.1016/S0006-2952(00)00570-0.

Frenguelli, B.G. (2019). The Purine Salvage Pathway and the Restoration of Cerebral ATP: Implications for Brain Slice Physiology and Brain Injury. Neurochem Res *44*, 661-675. https://doi.org/10.1007/s11064-017-2386-6.

Garg, A. (2011). Clinical review#: Lipodystrophies: genetic and acquired body fat disorders. The Journal of clinical endocrinology and metabolism *96*, 3313-3325. https://doi.org/10.1210/jc.2011-1159.

Gilardi, F., Winkler, C., Quignodon, L., Diserens, J.-G., Toffoli, B., Schiffrin, M., Sardella, C., Preitner, F., and Desvergne, B. (2019). Systemic PPARγ deletion in mice provokes lipoatrophy, organomegaly, severe type 2 diabetes and metabolic inflexibility. Metabolism *95*, 8-20. https://doi.org/10.1016/j.metabol.2019.03.003.

Giuliani, P., Zuccarini, M., Buccella, S., Peña-Altamira, L.E., Polazzi, E., Virgili, M., Monti, B., Poli, A., Rathbone, M.P., and Di Iorio, P., et al. (2017). Evidence for purine nucleoside phosphorylase (PNP) release from rat C6 glioma cells. Journal of neurochemistry *141*, 208-221. https://doi.org/10.1111/jnc.14004.

Gloy, V.L., Briel, M., Bhatt, D.L., Kashyap, S.R., Schauer, P.R., Mingrone, G., Bucher, H.C., and Nordmann, A.J. (2013). Bariatric surgery versus non-surgical treatment for obesity: a systematic review and meta-analysis of randomised controlled trials. BMJ : British Medical Journal *347*, f5934. https://doi.org/10.1136/bmj.f5934.

Gnad, T., Navarro, G., Lahesmaa, M., Reverte-Salisa, L., Copperi, F., Cordomi, A., Naumann, J., Hochhäuser, A., Haufs-Brusberg, S., and Wenzel, D., et al. (2020). Adenosine/A2B Receptor Signaling Ameliorates the Effects of Aging and Counteracts Obesity. Cell metabolism *32*, 56-70.e7. https://doi.org/10.1016/j.cmet.2020.06.006.

Gnad, T., Scheibler, S., Kügelgen, I. von, Scheele, C., Kilić, A., Glöde, A., Hoffmann, L.S., Reverte-Salisa, L., Horn, P., and Mutlu, S., et al. (2014). Adenosine activates brown adipose tissue and recruits beige adipocytes via A2A receptors. Nature *516*, 395-399. https://doi.org/10.1038/nature13816.

Gomez, G., and Sitkovsky, M.V. (2003). Differential requirement for A2a and A3 adenosine receptors for the protective effect of inosine in vivo. Blood *102*, 4472-4478. https://doi.org/10.1182/blood-2002-11-3624.

Gordon, J.L. (1986). Extracellular ATP: effects, sources and fate. The Biochemical journal *233*, 309-319. https://doi.org/10.1042/bj2330309.

GraphPad Software Inc. (2014). GraphPad Statistics Guide (San Diego, CA, USA).

References

Gray, J.H., Owen, R.P., and Giacomini, K.M. (2004). The concentrative nucleoside transporter family, SLC28. Pflugers Archiv : European journal of physiology *447*, 728-734. https://doi.org/10.1007/s00424-003-1107-y.

Gresele, P., Momi, S., and Falcinelli, E. (2011). Anti-platelet therapy: phosphodiesterase inhibitors. British Journal of Clinical Pharmacology *72*, 634-646. https://doi.org/10.1111/j.1365-2125.2011.04034.x.

Guallar, J.P., Cano-Soldado, P., Aymerich, I., Domingo, J.C., Alegre, M., Domingo, P., Villarroya, F., Javier Casado, F., Giralt, M., and Pastor-Anglada, M. (2007). Altered expression of nucleoside transporter genes (SLC28 and SLC29) in adipose tissue from HIV-1-infected patients. Antiviral therapy *12*, 853-863.

Guerra, C., Koza, R.A., Yamashita, H., Walsh, K., and Kozak, L.P. (1998). Emergence of brown adipocytes in white fat in mice is under genetic control. Effects on body weight and adiposity. J Clin Invest *102*, 412-420. https://doi.org/10.1172/JCI3155.

Guescini, M., Sisti, D., Rocchi, M.B.L., Stocchi, L., and Stocchi, V. (2008). A new real-time PCR method to overcome significant quantitative inaccuracy due to slight amplification inhibition. BMC bioinformatics *9*, 326. https://doi.org/10.1186/1471-2105-9-326.

Han, J., Lee, J.-E., Jin, J., Lim, J.S., Oh, N., Kim, K., Chang, S.-I., Shibuya, M., Kim, H., and Koh, G.Y. (2011). The spatiotemporal development of adipose tissue. Development (Cambridge, England) *138*, 5027-5037. https://doi.org/10.1242/dev.067686.

Hanlon, C.D., and Andrew, D.J. (2015). Outside-in signaling--a brief review of GPCR signaling with a focus on the Drosophila GPCR family. Journal of Cell Science *128*, 3533-3542. https://doi.org/10.1242/jcs.175158.

Hanna, J.N., McN Hill, P., and Sinclair, J.D. (1975). Human cardiorespiratory responses to acute cold exposure. Clinical and experimental pharmacology & physiology *2*, 229-238. https://doi.org/10.1111/j.1440-1681.1975.tb03028.x.

Haskó, G., Sitkovsky, M.V., and Szabó, C. (2004). Immunomodulatory and neuroprotective effects of inosine. Trends in Pharmacological Sciences *25*, 152-157. https://doi.org/10.1016/j.tips.2004.01.006.

Hatch, M.D. (1966). Adenylosuccinate synthetase and adenylosuccinate lyase from plant tissues. The Biochemical journal *98*, 198-203. https://doi.org/10.1042/bj0980198.

Hauser, A.S., Attwood, M.M., Rask-Andersen, M., Schiöth, H.B., and Gloriam, D.E. (2017). Trends in GPCR drug discovery: new agents, targets and indications. Nature reviews. Drug discovery *16*, 829-842. https://doi.org/10.1038/nrd.2017.178.

References

Hilger, D., Masureel, M., and Kobilka, B.K. (2018). Structure and dynamics of GPCR signaling complexes. Nature structural & molecular biology *25*, 4-12. https://doi.org/10.1038/s41594-017-0011-7.

Hills, N.K., and Johnston, S.C. (2008). Trends in usage of alternative antiplatelet therapy after stroke and transient ischemic attack. Stroke *39*, 1228-1232. https://doi.org/10.1161/STROKEAHA.107.496729.

Himms-Hagen, J., Melnyk, A., Zingaretti, M.C., Ceresi, E., Barbatelli, G., and Cinti, S. (2000). Multilocular fat cells in WAT of CL-316243-treated rats derive directly from white adipocytes. American journal of physiology. Cell physiology *279*, C670-81. https://doi.org/10.1152/ajpcell.2000.279.3.C670.

Hoffmann, L.S., Etzrodt, J., Willkomm, L., Sanyal, A., Scheja, L., Fischer, A.W.C., Stasch, J.-P., Bloch, W., Friebe, A., and Heeren, J., et al. (2015). Stimulation of soluble guanylyl cyclase protects against obesity by recruiting brown adipose tissue. Nature communications *6*, 7235. https://doi.org/10.1038/ncomms8235.

Hotamisligil, G.S., and Bernlohr, D.A. (2015). Metabolic functions of FABPs--mechanisms and therapeutic implications. Nature reviews. Endocrinology *11*, 592-605. https://doi.org/10.1038/nrendo.2015.122.

Iwaki, H., Ando, R., Miyaue, N., Tada, S., Tsujii, T., Yabe, H., Nishikawa, N., Nagai, M., and Nomoto, M. (2017). One year safety and efficacy of inosine to increase the serum urate level for patients with Parkinson's disease in Japan. Journal of the neurological sciences *383*, 75-78. https://doi.org/10.1016/j.jns.2017.10.030.

Jespersen, N.Z., Larsen, T.J., Peijs, L., Daugaard, S., Homøe, P., Loft, A., Jong, J. de, Mathur, N., Cannon, B., and Nedergaard, J., et al. (2013). A classical brown adipose tissue mRNA signature partly overlaps with brite in the supraclavicular region of adult humans. Cell metabolism *17*, 798-805. https://doi.org/10.1016/j.cmet.2013.04.011.

Jo, M., and Jung, S.T. (2016). Engineering therapeutic antibodies targeting G-protein-coupled receptors. Experimental & molecular medicine *48*, e207. https://doi.org/10.1038/emm.2015.105.

Kajimura, S., Seale, P., Kubota, K., Lunsford, E., Frangioni, J.V., Gygi, S.P., and Spiegelman, B.M. (2009). Initiation of myoblast to brown fat switch by a PRDM16-C/EBP-beta transcriptional complex. Nature *460*, 1154-1158. https://doi.org/10.1038/nature08262.

Kameoka, J., Tanaka, T., Nojima, Y., Schlossman, S.F., and Morimoto, C. (1993). Direct association of adenosine deaminase with a T cell activation antigen, CD26. Science (New York, N.Y.) *261*, 466-469. https://doi.org/10.1126/science.8101391.

References

Kao, Y.-H., Lin, M.-S., Chen, C.-M., Wu, Y.-R., Chen, H.-M., Lai, H.-L., Chern, Y., and Lin, C.-J. (2017). Targeting ENT1 and adenosine tone for the treatment of Huntington's disease. Hum Mol Genet *26*, 467-478. https://doi.org/10.1093/hmg/ddw402.

Kaster, M.P., Budni, J., Gazal, M., Cunha, M.P., Santos, A.R.S., and Rodrigues, A.L.S. (2013). The antidepressant-like effect of inosine in the FST is associated with both adenosine A1 and A 2A receptors. Purinergic signalling *9*, 481-486. https://doi.org/10.1007/s11302-013-9361-8.

Kather, H. (1988). Purine accumulation in human fat cell suspensions. Evidence that human adipocytes release inosine and hypoxanthine rather than adenosine. Journal of Biological Chemistry *263*, 8803-8809. https://doi.org/10.1016/S0021-9258(18)68377-2.

Kaur, J. (2014). A comprehensive review on metabolic syndrome. Cardiol Res Pract *2014*, 943162. https://doi.org/10.1155/2014/943162.

Khakh, B.S., and Burnstock, G. (2009). The double life of ATP. Scientific American *301*, 84-90, 92. https://doi.org/10.1038/scientificamerican1209-84.

Klepinin, A., Zhang, S., Klepinina, L., Rebane-Klemm, E., Terzic, A., Kaambre, T., and Dzeja, P. (2020). Adenylate Kinase and Metabolic Signaling in Cancer Cells. Frontiers in oncology *10*, 660. https://doi.org/10.3389/fonc.2020.00660.

Knittle, J.L., Timmers, K., Ginsberg-Fellner, F., Brown, R.E., and Katz, D.P. (1979). The growth of adipose tissue in children and adolescents. Cross-sectional and longitudinal studies of adipose cell number and size. The Journal of clinical investigation *63*, 239-246. https://doi.org/10.1172/JCI109295.

Kora Healthcare Ltd. (2012). Fachinformation Delimmun (Dublin).

Kotzbeck, P., Giordano, A., Mondini, E., Murano, I., Severi, I., Venema, W., Cecchini, M.P., Kershaw, E.E., Barbatelli, G., and Haemmerle, G., et al. (2018). Brown adipose tissue whitening leads to brown adipocyte death and adipose tissue inflammation. Journal of lipid research *59*, 784-794. https://doi.org/10.1194/jlr.M079665.

Kusminski, C.M., and Scherer, P.E. (2012). Mitochondrial dysfunction in white adipose tissue. Trends in endocrinology and metabolism: TEM *23*, 435-443. https://doi.org/10.1016/j.tem.2012.06.004.

Leblanc, E.S., O'Connor, E., Whitlock, E.P., Patnode, C.D., and Kapka, T. (2011). Effectiveness of primary care-relevant treatments for obesity in adults: a systematic evidence review for the U.S. Preventive Services Task Force. Annals of internal medicine *155*, 434-447. https://doi.org/10.7326/0003-4819-155-7-201110040-00006.

References

Ledderose, C., Bao, Y., Kondo, Y., Fakhari, M., Slubowski, C., Zhang, J., and Junger, W.G. (2016). Purinergic Signaling and the Immune Response in Sepsis: A Review. Clinical therapeutics *38*, 1054-1065. https://doi.org/10.1016/j.clinthera.2016.04.002.

Löffler, M., Morote-Garcia, J.C., Eltzschig, S.A., Coe, I.R., and Eltzschig, H.K. (2007). Physiological roles of vascular nucleoside transporters. Arteriosclerosis, thrombosis, and vascular biology *27*, 1004-1013. https://doi.org/10.1161/ATVBAHA.106.126714.

Mabley, J.G., Rabinovitch, A., Suarez-Pinzon, W., Haskó, G., Pacher, P., Power, R., Southan, G., Salzman, A., and Szabó, C. (2003). Inosine protects against the development of diabetes in multiple-low-dose streptozotocin and nonobese diabetic mouse models of type 1 diabetes. Molecular medicine (Cambridge, Mass.) *9*, 96-104. https://doi.org/10.2119/2003-00016.mabley.

Manolopoulos, K.N., Karpe, F., and Frayn, K.N. (2010). Gluteofemoral body fat as a determinant of metabolic health. International journal of obesity (2005) *34*, 949-959. https://doi.org/10.1038/ijo.2009.286.

Monaghan, T.K., Mackenzie, C.J., Plevin, R., and Lutz, E.M. (2008). PACAP-38 induces neuronal differentiation of human SH-SY5Y neuroblastoma cells via cAMP-mediated activation of ERK and p38 MAP kinases. Journal of neurochemistry *104*, 74-88. https://doi.org/10.1111/j.1471-4159.2007.05018.x.

Nedergaard, J., Bengtsson, T., and Cannon, B. (2007). Unexpected evidence for active brown adipose tissue in adult humans. American journal of physiology. Endocrinology and metabolism *293*, E444-52. https://doi.org/10.1152/ajpendo.00691.2006.

Nedergaard, J., and Cannon, B. (2014). The browning of white adipose tissue: some burning issues. Cell metabolism *20*, 396-407. https://doi.org/10.1016/j.cmet.2014.07.005.

Nguyen, M.D., Ross, A.E., Ryals, M., Lee, S.T., and Venton, B.J. (2015). Clearance of rapid adenosine release is regulated by nucleoside transporters and metabolism. Pharmacology research & perspectives *3*, e00189. https://doi.org/10.1002/prp2.189.

Nitti, V.W., Khullar, V., van Kerrebroeck, P., Herschorn, S., Cambronero, J., Angulo, J.C., Blauwet, M.B., Dorrepaal, C., Siddiqui, E., and Martin, N.E. (2013). Mirabegron for the treatment of overactive bladder: a prespecified pooled efficacy analysis and pooled safety analysis of three randomised, double-blind, placebo-controlled, phase III studies. International journal of clinical practice *67*, 619-632. https://doi.org/10.1111/ijcp.12194.

Organisation for Economic Co-operation and Development (2019). The Heavy Burden of Obesity: The Economics of Prevention. OECD Health Policy Studies. https://doi.org/10.1787/67450d67-en.

References

Panayiotou, C., Solaroli, N., and Karlsson, A. (2014). The many isoforms of human adenylate kinases. The International Journal of Biochemistry & Cell Biology *49*, 75-83. https://doi.org/10.1016/j.biocel.2014.01.014.

Pastor-Anglada, M., and Pérez-Torras, S. (2018). Who Is Who in Adenosine Transport. Frontiers in pharmacology *9*, 627. https://doi.org/10.3389/fphar.2018.00627.

Penuela, S., Gehi, R., and Laird, D.W. (2013). The biochemistry and function of pannexin channels. Biochimica et Biophysica Acta (BBA) - Biomembranes *1828*, 15-22. https://doi.org/10.1016/j.bbamem.2012.01.017.

Perdikari, A., Leparc, G.G., Balaz, M., Pires, N.D., Lidell, M.E., Sun, W., Fernandez-Albert, F., Müller, S., Akchiche, N., and Dong, H., et al. (2018). BATLAS: Deconvoluting Brown Adipose Tissue. Cell reports *25*, 784-797.e4. https://doi.org/10.1016/j.celrep.2018.09.044.

Pettengill, M., Robson, S., Tresenriter, M., Millán, J.L., Usheva, A., Bingham, T., Belderbos, M., Bergelson, I., Burl, S., and Kampmann, B., et al. (2013). Soluble ecto-5'-nucleotidase (5'-NT), alkaline phosphatase, and adenosine deaminase (ADA1) activities in neonatal blood favor elevated extracellular adenosine. The Journal of biological chemistry *288*, 27315-27326. https://doi.org/10.1074/jbc.M113.484212.

Poissonnet, C.M., Burdi, A.R., and Garn, S.M. (1984). The chronology of adipose tissue appearance and distribution in the human fetus. Early Human Development *10*, 1-11. https://doi.org/10.1016/0378-3782(84)90106-3.

Poon, I.K.H., Chiu, Y.-H., Armstrong, A.J., Kinchen, J.M., Juncadella, I.J., Bayliss, D.A., and Ravichandran, K.S. (2014). Unexpected link between an antibiotic, pannexin channels and apoptosis. Nature *507*, 329-334. https://doi.org/10.1038/nature13147.

Pouliot, M.-C., Després, J.-P., Nadeau, A., Moorjani, S., Prud&#039, Homme, D., Lupien, P.J., Tremblay, A., and Bouchard, C. (1992). Visceral Obesity in Men: Associations With Glucose Tolerance, Plasma Insulin, and Lipoprotein Levels. Diabetes *41*, 826. https://doi.org/10.2337/diab.41.7.826.

Puigserver, P., and Spiegelman, B.M. (2003). Peroxisome proliferator-activated receptor-gamma coactivator 1 alpha (PGC-1 alpha): transcriptional coactivator and metabolic regulator. Endocrine reviews *24*, 78-90. https://doi.org/10.1210/er.2002-0012.

Rhee, S.G., and Bae, Y.S. (1997). Regulation of phosphoinositide-specific phospholipase C isozymes. The Journal of biological chemistry *272*, 15045-15048. https://doi.org/10.1074/jbc.272.24.15045.

Rose, J.B., Naydenova, Z., Bang, A., Ramadan, A., Klawitter, J., Schram, K., Sweeney, G., Grenz, A., Eltzschig, H., and Hammond, J., et al. (2011). Absence of equilibrative nucleoside

transporter 1 in ENT1 knockout mice leads to altered nucleoside levels following hypoxic challenge. Life sciences *89*, 621-630. https://doi.org/10.1016/j.lfs.2011.08.007.

Rosen, E.D., and MacDougald, O.A. (2006). Adipocyte differentiation from the inside out. Nature reviews. Molecular cell biology *7*, 885-896. https://doi.org/10.1038/nrm2066.

Rosen, E.D., and Spiegelman, B.M. (2014). What we talk about when we talk about fat. Cell *156*, 20-44. https://doi.org/10.1016/j.cell.2013.12.012.

Rosenbaum, D.M., Rasmussen, S.G.F., and Kobilka, B.K. (2009). The structure and function of G-protein-coupled receptors. Nature *459*, 356-363. https://doi.org/10.1038/nature08144.

Rote Liste® Service GmbH (2021). Rote Liste. https://www.rote-liste.de/suche/stoff/061000/Inosin. 03.07.2021.

Sanyal, A., Naumann, J., Hoffmann, L.S., Chabowska-Kita, A., Ehrlund, A., Schlitzer, A., Arner, P., Blüher, M., and Pfeifer, A. (2017). Interplay between Obesity-Induced Inflammation and cGMP Signaling in White Adipose Tissue. Cell reports *18*, 225-236. https://doi.org/10.1016/j.celrep.2016.12.028.

Scheibler, S. (2017). Analysis of Adenosine Metabolism in Brown Adipose Tissue. Dissertation (Bonn: Naturwissenschaftliche Fakultät der Rheinischen - Friedrich - Wilhelms - Universität Bonn).

Schimmel, R.J., and McCarthy, L. (1984). Role of adenosine as an endogenous regulator of respiration in hamster brown adipocytes. The American journal of physiology, C301-307. https://doi.org/10.1152/ajpcell.1984.246.3.C301.

Schulz, T.J., and Tseng, Y.-H. (2013). Brown adipose tissue: development, metabolism and beyond. The Biochemical journal *453*, 167-178. https://doi.org/10.1042/BJ20130457.

Schwarzschild, M.A., Ascherio, A., Beal, M.F., Cudkowicz, M.E., Curhan, G.C., Hare, J.M., Hooper, D.C., Kieburtz, K.D., Macklin, E.A., and Oakes, D., et al. (2014). Inosine to increase serum and cerebrospinal fluid urate in Parkinson disease: a randomized clinical trial. JAMA neurology *71*, 141-150. https://doi.org/10.1001/jamaneurol.2013.5528.

Seale, P., Bjork, B., Yang, W., Kajimura, S., Chin, S., Kuang, S., Scimè, A., Devarakonda, S., Conroe, H.M., and Erdjument-Bromage, H., et al. (2008). PRDM16 controls a brown fat/skeletal muscle switch. Nature *454*, 961-967. https://doi.org/10.1038/nature07182.

Seale, P., Conroe, H.M., Estall, J., Kajimura, S., Frontini, A., Ishibashi, J., Cohen, P., Cinti, S., and Spiegelman, B.M. (2011). Prdm16 determines the thermogenic program of subcutaneous white adipose tissue in mice. The Journal of clinical investigation *121*, 96-105. https://doi.org/10.1172/JCI44271.

References

Seale, P., Kajimura, S., Yang, W., Chin, S., Rohas, L.M., Uldry, M., Tavernier, G., Langin, D., and Spiegelman, B.M. (2007). Transcriptional control of brown fat determination by PRDM16. Cell metabolism *6*, 38-54. https://doi.org/10.1016/j.cmet.2007.06.001.

Sharma, A.M., and Padwal, R. (2010). Obesity is a sign – over-eating is a symptom: an aetiological framework for the assessment and management of obesity. Obesity Reviews *11*, 362-370. https://doi.org/10.1111/j.1467-789X.2009.00689.x.

Sigma-Aldrich Corp. (2014). ADP/ATP Ratio Assay Kit (MAK135) - Technical Bulletin (St. Louis, MO, USA).

Spalding, K.L., Arner, E., Westermark, P.O., Bernard, S., Buchholz, B.A., Bergmann, O., Blomqvist, L., Hoffstedt, J., Näslund, E., and Britton, T., et al. (2008). Dynamics of fat cell turnover in humans. Nature *453*, 783-787. https://doi.org/10.1038/nature06902.

Srivastava, G., and Apovian, C.M. (2018). Current pharmacotherapy for obesity. Nature reviews. Endocrinology *14*, 12-24. https://doi.org/10.1038/nrendo.2017.122.

Stolic, M., Russell, A., Hutley, L., Fielding, G., Hay, J., MacDonald, G., Whitehead, J., and Prins, J. (2002). Glucose uptake and insulin action in human adipose tissue--influence of BMI, anatomical depot and body fat distribution. International journal of obesity and related metabolic disorders : journal of the International Association for the Study of Obesity *26*, 17-23. https://doi.org/10.1038/sj.ijo.0801850.

Sugii, S., Olson, P., Sears, D.D., Saberi, M., Atkins, A.R., Barish, G.D., Hong, S.-H., Castro, G.L., Yin, Y.-Q., and Nelson, M.C., et al. (2009). PPARgamma activation in adipocytes is sufficient for systemic insulin sensitization. Proceedings of the National Academy of Sciences of the United States of America *106*, 22504-22509. https://doi.org/10.1073/pnas.0912487106.

Symonds, M.E. (2013). Brown adipose tissue growth and development. Scientifica *2013*, 305763. https://doi.org/10.1155/2013/305763.

Syrovatkina, V., Alegre, K.O., Dey, R., and Huang, X.-Y. (2016). Regulation, Signaling, and Physiological Functions of G-Proteins. Journal of molecular biology *428*, 3850-3868. https://doi.org/10.1016/j.jmb.2016.08.002.

Tozzi, M., Hansen, J.B., and Novak, I. (2020). Pannexin-1 mediated ATP release in adipocytes is sensitive to glucose and insulin and modulates lipolysis and macrophage migration. Acta physiologica (Oxford, England) *228*, e13360. https://doi.org/10.1111/apha.13360.

References

van den Berg, Susan M, van Dam, A.D., Rensen, P.C.N., de Winther, Menno P J, and Lutgens, E. (2017). Immune Modulation of Brown(ing) Adipose Tissue in Obesity. Endocrine reviews *38*, 46-68. https://doi.org/10.1210/er.2016-1066.

van Luu-The, Paquet, N., Calvo, E., and Cumps, J. (2005). Improved real-time RT-PCR method for high-throughput measurements using second derivative calculation and double correction. BioTechniques *38*, 287-293. https://doi.org/10.2144/05382RR05.

van Marken Lichtenbelt, W.D., Vanhommerig, J.W., Smulders, N.M., Drossaerts, J.M.A.F.L., Kemerink, G.J., Bouvy, N.D., Schrauwen, P., and Teule, G.J.J. (2009). Cold-activated brown adipose tissue in healthy men. The New England journal of medicine *360*, 1500-1508. https://doi.org/10.1056/NEJMoa0808718.

Virtanen, K.A., Lidell, M.E., Orava, J., Heglind, M., Westergren, R., Niemi, T., Taittonen, M., Laine, J., Savisto, N.-J., and Enerbäck, S., et al. (2009). Functional brown adipose tissue in healthy adults. The New England journal of medicine *360*, 1518-1525. https://doi.org/10.1056/NEJMoa0808949.

Wang, W., Chen, N.-Y., Ren, D., Davies, J., Philip, K., Eltzschig, H.K., Blackburn, M.R., Akkanti, B., Karmouty-Quintana, H., and Weng, T. (2021). Enhancing Extracellular Adenosine Levels Restores Barrier Function in Acute Lung Injury Through Expression of Focal Adhesion Proteins. Frontiers in molecular biosciences *8*, 636678. https://doi.org/10.3389/fmolb.2021.636678.

Wang, W., and Seale, P. (2016). Control of brown and beige fat development. Nature reviews. Molecular cell biology *17*, 691-702. https://doi.org/10.1038/nrm.2016.96.

Welihinda, A.A., Kaur, M., Greene, K., Zhai, Y., and Amento, E.P. (2016). The adenosine metabolite inosine is a functional agonist of the adenosine A2A receptor with a unique signaling bias. Cellular signalling *28*, 552-560. https://doi.org/10.1016/j.cellsig.2016.02.010.

Welihinda, A.A., Kaur, M., Raveendran, K.S., and Amento, E.P. (2018). Enhancement of inosine-mediated A2AR signaling through positive allosteric modulation. Cellular signalling *42*, 227-235. https://doi.org/10.1016/j.cellsig.2017.11.002.

Wettschureck, N., and Offermanns, S. (2005). Mammalian G proteins and their cell type specific functions. Physiological reviews *85*, 1159-1204. https://doi.org/10.1152/physrev.00003.2005.

Weyer, C., Tataranni, P.A., Snitker, S., Danforth, E., and Ravussin, E. (1998). Increase in insulin action and fat oxidation after treatment with CL 316,243, a highly selective beta3-adrenoceptor agonist in humans. Diabetes *47*, 1555-1561. https://doi.org/10.2337/diabetes.47.10.1555.

References

Williams, D.M., Nawaz, A., and Evans, M. (2020). Drug Therapy in Obesity: A Review of Current and Emerging Treatments. Diabetes therapy : research, treatment and education of diabetes and related disorders *11*, 1199-1216. https://doi.org/10.1007/s13300-020-00816-y.

Wilson-Fritch, L., Nicoloro, S., Chouinard, M., Lazar, M.A., Chui, P.C., Leszyk, J., Straubhaar, J., Czech, M.P., and Corvera, S. (2004). Mitochondrial remodeling in adipose tissue associated with obesity and treatment with rosiglitazone. J Clin Invest *114*, 1281-1289. https://doi.org/10.1172/JCI21752.

World Health Organization (2000). Obesity: preventing and managing the global epidemic. Report of a WHO consultation (Geneva).

World Health Organization (2018). Noncommunicable diseases country profiles 2018 (Geneva).

World Health Organization (2021). Body mass index - BMI. https://www.euro.who.int/en/health-topics/disease-prevention/nutrition/a-healthy-lifestyle/body-mass-index-bmi. 24.05.2021.

Wu, J., Boström, P., Sparks, L.M., Ye, L., Choi, J.H., Giang, A.-H., Khandekar, M., Virtanen, K.A., Nuutila, P., and Schaart, G., et al. (2012). Beige adipocytes are a distinct type of thermogenic fat cell in mouse and human. Cell *150,* 366-376. https://doi.org/10.1016/j.cell.2012.05.016.

Xue, B., Rim, J.-S., Hogan, J.C., Coulter, A.A., Koza, R.A., and Kozak, L.P. (2007). Genetic variability affects the development of brown adipocytes in white fat but not in interscapular brown fat. Journal of lipid research *48*, 41-51. https://doi.org/10.1194/jlr.M600287-JLR200.

Zhang, J., Visser, F., King, K.M., Baldwin, S.A., Young, J.D., and Cass, C.E. (2007). The role of nucleoside transporters in cancer chemotherapy with nucleoside drugs. Cancer metastasis reviews *26*, 85-110. https://doi.org/10.1007/s10555-007-9044-4.

Zhang, Y., Proenca, R., Maffei, M., Barone, M., Leopold, L., and Friedman, J.M. (1994). Positional cloning of the mouse obese gene and its human homologue. Nature *372*, 425-432. https://doi.org/10.1038/372425a0.

Ziemke, F., and Mantzoros, C.S. (2010). Adiponectin in insulin resistance: lessons from translational research. Am J Clin Nutr *91*, 258S-261S. https://doi.org/10.3945/ajcn.2009.28449C.

Zoref-Shani, E. (1992). Metabolic fate of hypoxanthine and inosine in cultured cardiomyocytes. Journal of Molecular and Cellular Cardiology *24*, 183-189. https://doi.org/10.1016/0022-2828(92)93154-C.

List of figures

List of schemes

List of tables

List of tables

Summary

During the last decades, obesity has become a pandemic disease, associated with severe comorbidities, and a major problem for health care systems. Obesity results from energy imbalance, when energy intake exceeds energy expenditure. In this context, the identification of metabolically active brown adipose tissue (BAT) in adult humans revealed a new and promising target for future obesity therapies. In particular, brown adipocytes express uncoupling protein 1 (UCP1), this mitochondrial protein mediates dissipation of energy in form of heat (non-shivering thermogenesis), thereby increasing whole body energy expenditure. Moreover, white adipose tissue (WAT), especially the subcutaneous depots (WATi), can undergo browning/beiging. The resulting beige adipocytes express UCP1 and contribute to enhanced energy expenditure by performing non-shivering thermogenesis. Both types of thermogenic adipocytes (brown and beige adipocytes) are activated by cold exposure and β3-adrenergic receptor agonists. However, due to cardiac side effects or insufficient oral bioavailability, targeting β3-adrenergic receptors is not feasible as obesity therapy. Therefore, novel molecules and targets activating thermogenesis of adipose tissues need to be identified and investigated.

This thesis presents a novel approach to increase energy expenditure by stimulation of thermogenic adipose tissues with the purine inosine.

Performed experiments of this thesis revealed that inosine is present in dialysates of thermogenic brown and beige adipose tissue. In addition, extracellular inosine concentrations of BAT and WATi were significantly increased after physiological activation. Interestingly, an activating effect of inosine on lipolysis and intracellular cAMP levels of brown adipocytes was observed. Moreover, administration of inosine to mice by micro-osmotic pumps resulted in significantly increased whole body oxygen consumption and significantly reduced weight gain during high fat diet. In addition, *Ucp1* expression was significantly increased in BAT and WATi of inosine-treated mice compared to control littermates.

In further experiments it was shown that inhibition of the equilibrative nucleoside transporter 1 (ENT1) resulted in enhanced extracellular inosine levels of adipocytes. The effects of ENT1-deficiency on adipose tissue metabolism were investigated using a global ENT1-KO mouse model. Brown and white adipocytes isolated from ENT1-KO mice showed improved differentiation and thermogenic function as compared to WT cells. Furthermore, ENT1-KO mice gained significantly less weight during high fat diet and had improved glucose tolerance in comparison to WT littermates. In addition, significantly increased oxygen consumption of ENT1-KO mice was detected, indicating promoted energy expenditure by loss of ENT1, which in turn led to enhanced extracellular inosine concentrations. These findings were in line with

significantly increased expression of thermogenic genes, including *Ucp1*, in ENT1-KO BAT after high fat diet challenge.

In order to investigate to what extent ENT1-deletion in adipocytes affects whole body energy expenditure, an adipocyte-specific ENT1-A-KO mouse model (ENT1floxed-AdiponectinCre) was analyzed. Isolated ENT1-A-KO (ENT1$^{fl/fl}$ AdiponectinCre+) brown and white adipocytes showed improved differentiation with significantly enhanced expression of adipogenic and thermogenic marker genes in comparison to control cells (ENT1$^{fl/fl}$ AdiponectinCre-). Moreover, significantly increased lipolysis and oxygen consumption of BAT and WATi explants, as well as significantly enhanced whole body oxygen consumption of ENT1-A-KO mice was measured as compared to control animals. Further analyses revealed increased thermogenic gene expression in BAT and WATi as well as significantly increased whole body oxygen consumption of ENT1-A-KO animals after high fat diet. In addition, the ENT1-A-KO mice performed better, when challenged with a glucose tolerance test after high fat diet.

A further series of experiments showed that inosine signaling in adipocytes is dependent on the adenosine A2b receptor. In particular, statistically significant inosine-induced effects on *in vitro* lipolysis, intracellular cAMP concentrations and *Ucp1* expression as well as *in vivo* oxygen consumption were abolished in adenosine A2b receptor-deficient adipocytes and mice.

In conclusion, the presented results in this thesis indicate that inosine acts as a stimulatory autocrine/paracrine mediator in brown and beige adipose tissue. Moreover, it was shown that ENT1 is a relevant regulator of extracellular inosine concentrations and metabolism of thermogenic adipocytes. Consequently, increasing extracellular inosine concentrations - by administration of exogenous inosine or inhibition of ENT1 leading to increased endogenous extracellular inosine levels - represents a novel approach to enhance energy expenditure of thermogenic adipose tissue. Thus, inosine and its transporter ENT1 could be used as a new pharmacological agent and as a target for future obesity therapy. Further studies are needed to elucidate the extent to which the promising results observed in the mouse models are transferrable to humans.